Magnetization dynamics

Coherent precession, optical manipulation, and nanoscale switching

Benny Koene

Printed by Ipskamp Drukkers
Enschede, The Netherlands, 2014

ISBN 978-94-6259-413-5

Magnetization dynamics

Coherent precession, optical manipulation, and nanoscale switching

Proefschrift

ter verkrijging van de graad van doctor
aan de Radboud Universiteit Nijmegen
op gezag van de rector magnificus prof. dr. Th. L. M. Engelen,
volgens besluit van het college van decanen
in het openbaar te verdedigen op woensdag 10 december 2014
om 10:30 uur precies

door

Benny Koene

geboren op 16 oktober 1985
te Woerden, Nederland

Promotoren:	Prof. dr. A. I. Kirilyuk
	Prof. dr. Th. H. M. Rasing

Manuscriptcommissie:

Prof. dr. N. E. Hussey	(voorzitter)
Prof. dr. B. Koopmans	Technische Universiteit Eindhoven
Prof. dr. F. Nolting	Universität Basel, Zwitserland/Paul Scherrer Institute

This work was supported by de Nederlandse Organisatie voor Wetenschappelijk Onderzoek (NWO) and de Stichting voor Fundamenteel Onderzoek der Materie (FOM) as part of project SPIN 109 (08SPIN09), as well as by the European Union's Seventh Framework Programe (FP7/2007-2013) Grant No. 281043 (FemtoSpin) and by the NWO-DFG project DN 66-150.

"Our greatest weakness lies in giving up. The most certain way to succeed is always to try just one more time."

Thomas A. Edison

Preface

The thesis you are now reading is the result of four years of exploring. Where exploring can be interpreted in different ways: of course scientifically but as well as on a personal level and in the sense of travelling. A lot of people have helped me during my discovery journey or made the journey more fun. I would therefore like to use this preface to thank them for their contribution.

First of all I would like to thank my promoters, Andrei and Theo for giving me the opportunity to work in their group and guiding me while I was learning about magnetization dynamics. When I arrived in Nijmegen I actually did not know that much about magnetization dynamics but there was a project available related to plasmonic antennas, and with plasmonics I had gained some experience during my studies. Now, four years later only a fourth of this thesis is related to that project, the rest is entirely related to magnetization dynamics. Thank you as well for giving me the opportunity to work on several very different projects, I really enjoyed that. Andrei I would also like to thank you for being my daily supervisor and being always available for discussions.

As the work in this thesis consists for a large part of experimental work I was very happy with the three technicians in the group. Tonnie, Andre, Albert vE, thank you for your technical assistance. I really appreciated your input for technical solutions and despite your always busy schedule the solutions where always supplied in a short time span. Thank you as well for your effort in keeping the lasers up and running.

Thank you Marilou, for all your information about and assistance with the necessary administrative tasks. You where always available and willing to help when I had an administrative question.

I would also like to thank the manuscript commission, prof. Nigel Hussey, prof. Bert Koopmans and prof. Frithjof Nolting for reading my thesis and their feedback.

The work presented here could also not have been possible without people from outside Nijmegen. For the work on the nanoscale switching I would like to thank Alex, Han, Catherine, TianMin, prof. Hermann Dürr, and the others that assisted in the X-ray holography measurements with the Stanford synchrotron or that contributed to the discussion of the data. I really enjoyed experiencing to work with such a facility as well as the going out for dinner together or it is probably better to say going out for eating a burger together.

As here in Nijmegen we depend strongly on samples that are fabricated elsewhere I do not want to forget to thank the people that were involved in the making of the samples. Xiaofei, Jer-Shing and prof. Bert Hecht for the fabrication of the plasmonic antennas and their contributions to the discussion about the experimental data, and prof. Arata Tsukamoto for the supply of the magnetic materials.

For the work on the bismuth iron garnet I would like to thank Marwan, Elena and prof. Niels Keller. We had some very useful discussions about the sample and the data. Marwan I really enjoyed your enthusiasms when we where measuring together.

For the measurements on the magnon Bose-Einstein condensate I would like to thank the people from Münster: Patrick, Oleksandr, Vladislav and prof. Sergej Demokritov. Patrick, Oleksandr, I am happy that after a lot of trying we finally found the signal we were looking for. Without each other we would probably have given up earlier.

This brings me back to my direct colleagues from whom I have learned a lot in and outside the lab as well as that we had a lot of fun together. Here I would like to especially thank Matteo, you really helped me a lot in starting up my research in the group but also later on you were always available for a discussion and I learned a lot from you. Thank you as well for finding the overlap in the cases when I could not find it.

Of course I would also like to thank here all my other colleagues that made my PhD time enjoyable. Thank you Addis, Alex, Alexey, Albert D, Boldizsar, Bowen, Changhoon, Chris, Christian, Davide, Dennis, Diana, Dima A, Dima M, Fred, Huub, Ilie, Ilya, Jan, Jeroen, Johan dJ, Johan M, Jonas, Jos, Kadir, Koen, Lars, Laura, Lucca, Magnus, Mathieu, Remko, Raja G, Rajasekhar, Rostislav, Ruslan, Sam, Sasha, Sergey, Siebe, Tahoora, Thomas, Valeriy, Wei-Ta, Yuri and Yusuke. I enjoyed to talk, drink, eat, party, climb or play volleyball with you as well as to loose or win the sportsday together, to explore the conference cities, to loose from you with carting and to (try to) shoot on you during paintball.

In het Nederlands wil ik ook nog mijn vrienden bedanken voor het geven van de zo nu en dan nodige afleiding. Zowel mijn studie vrienden uit Delft: Alexander, Arjan, Freek, Johan vdB, Sjoerd, Thijs vL, Tom, en Wendy. Als ook mijn vrienden uit de regio Gouda: Dirk en Thijs dB. Bedankt.

Als laatste wil ik ook mijn ouders en mijn broertje bedanken voor hun interesse en voor het altijd klaar staan als ik ergens ondersteuning of advies bij nodig heb. Pa, Ma, uiteindelijk hebben jullie er ook voor gezorgd dat dit proefschrift hier nu ligt.

BKoene

Benny Koene　　　　Nijmegen, September 2014

Contents

Chapter 1

Introduction

In the current society we cannot imagine anymore to work without information technology. Governments and companies rely a lot on digital systems, but also you and me have to deal with information technology in our daily life. Think of working on a computer, internet, performing a pin transaction at the supermarket and using the increasing possibilities on your smart phone. For all those applications the storage and retrieval of digital information is of primary importance. This can be locally on the hard drive of your computer or delocalized on servers in a data center.

Currently the worldwide most used data storage device is the magnetic hard disk drive (HDD). This device stores digital information in oppositely oriented magnetic domains. The development of this device is highly focused on increasing the data density further and further. Preferably the access speed should be increased as well. Furthermore in the last decade the energy efficiency has become more and more important.

In the first section of this chapter we will give a brief overview of the advances in magnetic data recording technologies. The second section will give an introduction about magnetization dynamics which is the most important process involved in these technologies. Third we will discuss how the magnetization can be controlled by light pulses and that it is even possible to use this optical control in a data recording scheme. In the last section the scope and outline of this thesis can be found.

1.1 Magnetic Data Recording

Several technologies are developed and are being developed to increase the density of the data to be stored. One important parameter to consider in decreasing the size of the smallest bit (magnetic domain) is the anisotropy of the magnetic material. If the anisotropy is too small, thermal energy will win from the magnetic anisotropy energy of small bits and the bits will become randomly oriented and thus information gets lost. Hence the larger the coercive field, which is directly defined by the anisotropy, the smaller the domains will be that can be written in the material.

However a larger coercivity also means that the required field to switch the magnetization increases. The field that can be obtained with the small recording head that moves over the recording disks, only about 10 nm above the surface[1], is limited by the material properties to about 2 to 2.4 T [2, 3]. Around 2006, [4] the hard drive manufacturers switched from parallel (Fig. 1.1(a)) to perpendicular orientation of the magnetization with respect to the writing disk (Fig. 1.1(b)). The advantage of perpendicular orientation of the magnetization is that a magnetic soft under layer can be used to increase the effective field in the recording layer [5].

At the moment another technique is explored that enables the use of materials with an even higher coercive field. This technique uses a laser to locally heat the recording material such that temporarily the coercive field locally decreases and a lower applied field is necessary to switch the magnetic domain. For this technique to be useful the laser light has to be focused to a nanoscale spot, in order to achieve a data density superior to the one of the usual magnetic recording. To achieve the nanoscale focusing the field-confining properties of plasmonic structures are employed[8, 9]. The above described technique is known as Heat or Thermally Assisted Magnetic Recording (HAMR or TAMR [10–12]). In Fig. 1.1(c) a schematic of a possible realization of a HAMR/TAMR read/write head is given.

For HAMR/TAMR a laser has thus to be incorporated into the HDD, while a magnetic field is still necessary. Hence it will be challenging to decrease the energy consumption. Notice moreover, that a significant amount of energy in HDD's has to be used for the mechanical rotation of the magnetic disks. This rotational mechanism is as well a limiting factor in the access time [13].

Another interesting magnetic information technology with a faster access time is Magnetic Random Access Memory (MRAM) [14]. MRAM can be based on magnetic tunnel junctions [15–17] or spin transfer torque[18–20]. In the former a magnetic field pulse caused by two current pulses is used for the writing of the bit while in the latter a spin polarized current controls the magnetization and thus the bit value. Compared to other random access memories, MRAM is non-volatile. Together with its fast access time MRAM is therefore thought to be able to become a universal memory [13]. The device architecture of an MRAM device is schematically shown in Fig. 1.2.

The most important process in the magnetic data storage technology as discussed up to now is the change in direction of the magnetization by 180 deg. Hence to find new ways to increase the data density, energy efficiency and switching speed, it is necessary to obtain fundamental understanding of the dynamic processes that are involved in the magnetic switching process.

In summary, the importance of magnetic storage causes a lot of interest to the processes of magnetization dynamics and reversal at small length and time scales.

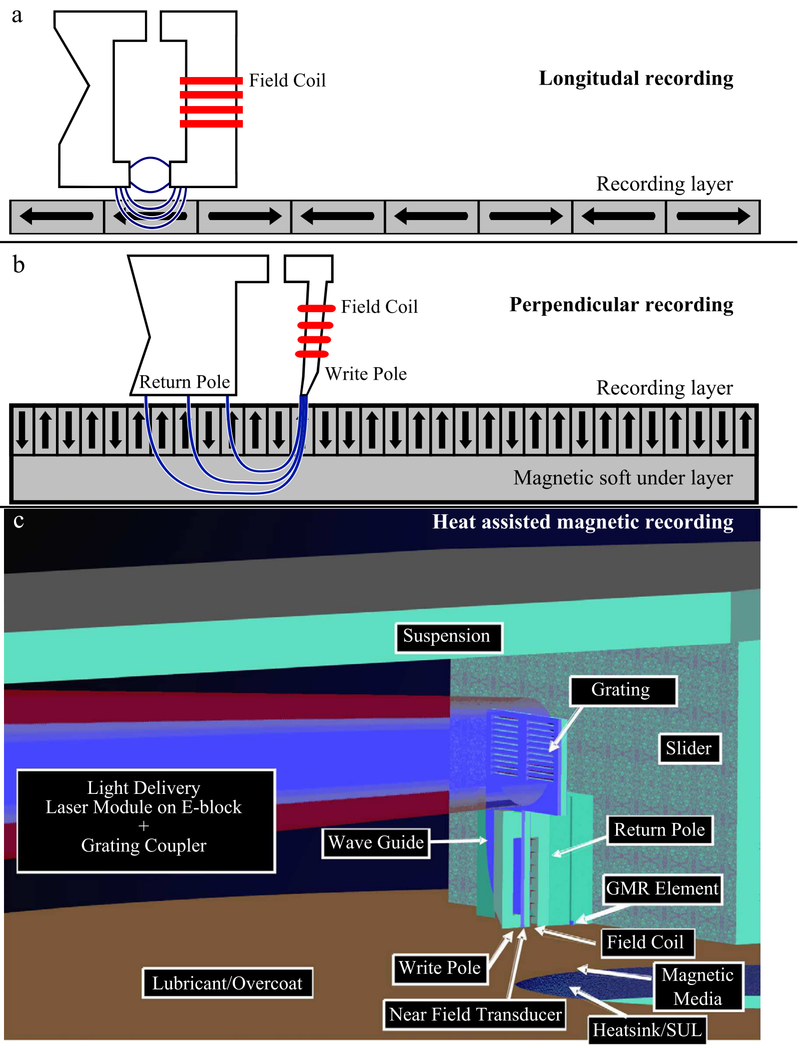

Figure 1.1: An overview of the development in magnetic data storage. In (a) longitudinal magnetic recording is shown. The arrows indicate the direction of the magnetization. Opposite directions represent a bit with a value of ‘0’or ‘1’. The perpendicular recording scheme is shown in (b). In (c) a possible HAMR/TAMR write head is shown. Figures (a) and (b) are adapted from Ref. [6] while (c) is adapted from Ref. [7].

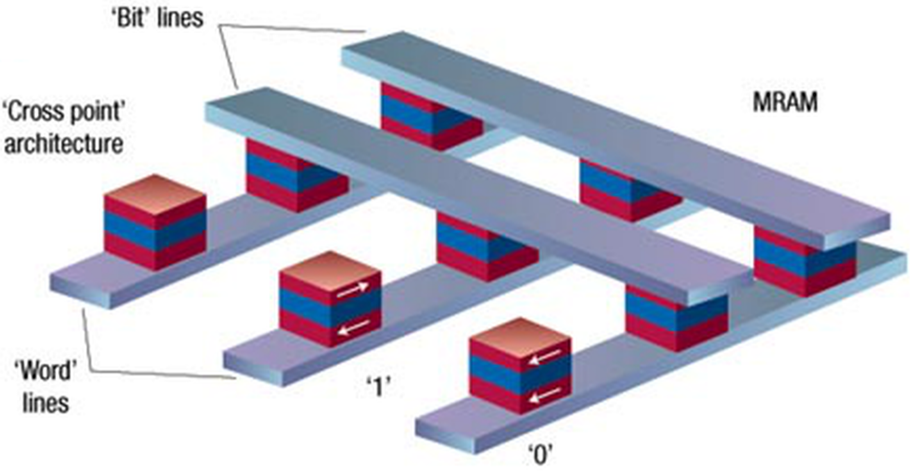

Figure 1.2: A schematic of the MRAM device architecture. This figure is adapted from Ref. [13].

1.2 Magnetization dynamics

After having discussed the importance of magnetization dynamics in the previous section, this section will discuss the basic physical equations and phenomena that form the basis for magnetization dynamics. First we will introduce the Landau Lifshitz Gilbert equation, then relaxation processes are discussed, followed by the description of a Bose-Einstein condensate of magnons in which the relaxation processes determine the coherence of this condensate.

1.2.1 Landau Lifshitz Gilbert equation

The magnetization dynamics induced by external magnetic fields are well described by the Landau-Lifshitz-Gilbert (LLG) equation [21, 22]:

$$\frac{\mathrm{d}\mathbf{m}}{\mathrm{d}t} = \gamma \mathbf{m} \times \mathbf{H}_{\mathrm{eff}} + \frac{\alpha}{|\mathbf{m}|} \mathbf{m} \times \frac{\mathrm{d}\mathbf{m}}{\mathrm{d}t}. \tag{1.1}$$

Here $\mathbf{m}$ is the magnetization vector, γ the gyromagnetic ratio, $\mathbf{H}_{\mathrm{eff}}$ the effective field and α the Gilbert damping. A sketch of the described precessional motion is shown in Fig. 1.3(a).

The effective field is constructed from a variety of contributions from which the most important ones are the external field, H_{ext}, the exchange field, H_{exch} in case of an inhomogeneous magnetization, the anisotropy field, H_{ani}, the demagnetizing field, H_{dem} and in case of the presence of a light pulse this might also be an impulsive field, H_{imp} as will be explained later on. Thus in general

$$\mathbf{H}_{\mathrm{eff}} = \mathbf{H}_{\mathrm{ext}} + \mathbf{H}_{\mathrm{exch}} + \mathbf{H}_{\mathrm{ani}} + \mathbf{H}_{\mathrm{dem}} + \mathbf{H}_{\mathrm{imp}}. \tag{1.2}$$

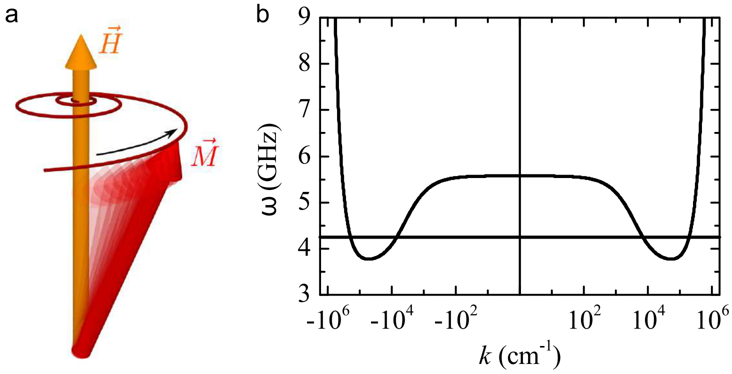

Figure 1.3: The uniform damped magnetization precession as described by Eq. 1.1 is schematically shown in (a) (adapted from Ref. [26]). In the absence of a homogeneous excitation it becomes possible to excite traveling spin waves/magnons. The dispersion curve for these magnons is shown in (b) for a magnetic thin film with the magnetization in the film plane and the wave vector of spin waves along the magnetization (backward volume mode). This curve is obtained with the equations as given in Ref. [25] and will be discussed in more detail in Chapter 6.

Magnetization dynamics can be induced by changing either one of the fields that determine H_{eff}.

When the external magnetic field is the most important contribution, it follows from Eq. (1.1) that the fastest switching path is achieved by applying a short field pulse perpendicularly to the magnetization direction. The field pulse can become shorter when the field amplitude is increased. However it has been demonstrated that this precessional switching becomes non-deterministic below 2 ps [23, 24].

With the techniques discussed in this thesis a magnetic material is only locally excited. This allows for a spatial variation in the resulting magnetization dynamics and the possibility of the magnetic precession to travel through the material in a wave-like manner. These traveling precessional waves are called spin waves or magnons [25]. The frequency of the magnetic precession for spin waves depend on their k-vector. An example of a magnon dispersion curve for a magnetic thin film is shown in Fig. 1.3(b).

1.2.2 Relaxation processes

The Gilbert damping α is worth a more detailed discussion. Due to spin lattice interactions, without an external continuous driving force the magnetization will precess towards an equilibrium position where the precession is stopped. This process is taken into account by the second term on the right hand side in Eq. (1.1). The Gilbert damping constant α is a material related quantity.

In general the damping α can be divided in the intrinsic damping α_{int}, caused by the above mentioned spin lattice interactions, and a non-intrinsic part, $\alpha_{\text{non-int}}$. This latter part can be caused by a poor fabrication quality of the material or this can be related to an inhomogeneous excitation mechanism [27–31]. Defects in the sample cause a spread in the sample anisotropy and thus in the excited precession frequencies as the anisotropy influences the effective field in Eq. (1.1). The subsequent excitation of spin waves will thus result in the presence of oscillations with different precession frequencies. Due to this decoherence of precession frequencies the observed damping can increase.

Another pathway for relaxation is resulting from interactions of magnons (or spin waves) with other magnons. By this so called magnon-magnon interaction it is possible that magnons of a different frequency are created. This interaction thus leads to a redistribution of magnons over the frequencies and is responsible for the thermalization of the magnon system. Note that the homogeneous precession mode can only be affected by such mechanism when there are magnon states with lower energies, for example in the backward volume mode shown in Fig. 1.3(b).

Actually for the switching of magnetization with an external field aligned almost anti parallel to the magnetization the damping plays an important role [32]. Without the second term in Eq. (1.1) the magnetization would not align along the applied magnetic field.

1.2.3 Bose-Einstein condensation

A phenomenon were relaxation processes play an important role is the formation of a magnon Bose-Einstein condensate. Bose-Einstein condensation [33, 34] is the condensation of bosons in the lowest energy state when in thermal equilibrium all other states are occupied. Such a condensation can occur as well in a quasi-equilibrium of magnons in garnet thin films [35]. From the magnon dispersion relation in Fig. 1.3(b) it follows that the magnons all collect in the two minima that are visible in this figure. To reach this minimum relaxation via magnon-magnon interactions is necessary. For this the number of magnons should be approximately conserved, while the magnon system should be in thermal equilibrium. Therefore, magnon-magnon relaxation processes should be much faster than the magnon-phonon (or spin-lattice) ones. Notice that the minima are located at opposite k-vectors which means that the magnons in the condensate consists of waves traveling in opposite direction and thus will form standing waves.

Bose-Einstein condensation suggests that all magnons are collected in a single energy state upon occurrence of the condensation. Hence they will precess at a single coherent frequency. However we have seen in the previous subsection that magnons have a finite life time due to relaxation processes. This finite lifetime will influence the coherence of the precession. The spectral width of the precession related to the condensate is theoretically expected to be inversely proportional to the magnon life time. However in experiments up to now only spectrally much broader condensates are observed [35, 36].

1.3 Laser induced magnetization dynamics

Magnetization dynamics can be excited in different ways. For example, by applying a magnetic field in a stepwise way along a direction different from the magnetization direction, the magnetization will start to precess according to Eq. (1.1) until the damping causes the magnetization to be aligned with the static field. Another possible excitation is by coupling a microwave field with a frequency equal to the Larmor precession condition ($\omega = \gamma H_{\text{ext}}$) [37]. In this way resonant excitation of magnetic precession is achieved. However it is also possible to excite magnetization dynamics with ultra short (femtosecond) intense light pulses, making it possible to influence the magnetization ultra fast on the same time scale as the pulse duration.

For this possibility of ultra fast control of magnetization and the wish to use this fast control in storage devices, the magnetization dynamics discussed in this thesis are mainly excited by light. An exception of this is the experiment discussed in Chapter 6 where microwave pumping is used.

The mechanisms that allow magnetization dynamics to be excited by light are diverse. Therefore, in this section, we will give an overview of the known mechanisms to excite magnetization dynamics optically. These effects are divided over four subsections which respectively discuss demagnetization in metals, heat induced switching, photo-magnetic effects and opto-magnetic effects.

1.3.1 Demagnetization in metals

The paper of Beaurepaire et al. [38] in 1996 in which the observation of laser induced ultrafast demagnetization was reported, was basically the start for all other studies with optical pump-probe setups on the manipulation of magnetic properties on the femtosecond time scale. The authors showed that the excitation of nickel with an intense 60 fs short laser pulse resulted in the observation of a decrease in the magnetization, $|\mathbf{m}|$ in the first picosecond. The measured data from the paper can be found in Fig. 1.4.

The observation of demagnetization was followed by an extensive discussion about its origin. Basically the effect is ascribed to a complex combination of relaxation processes between the electrons, the lattice and the spins of the material. A review of the numerous studies that contributed to a better understanding of the effect can be found in Ref. [39].

At the moment of writing this thesis, two main mechanisms are proposed that could explain the reduction in the magnetization. In the first mechanism the spins of the electrons flip and thus the net magnetization reduces [40]. In the second model the diffusion of electrons with a net specific spin orientation to other areas in the sample cause a decrease in the local magnetization [41].

1.3.2 All optical switching

The observation of optical induced ultrafast demagnetization raised the question if it was maybe possible to use a femtosecond light pulse to switch the magnetization

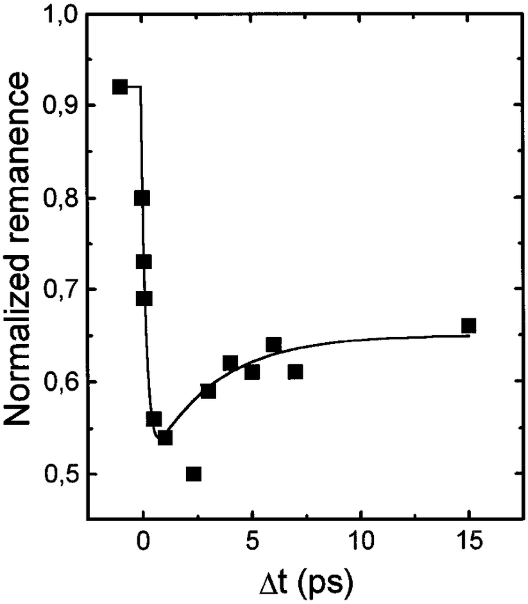

Figure 1.4: Ultra fast demagnetization in Nickel as measured for the first time by Beaurepaire et al. This figure is adapted from Ref. [38].

by 180 deg ultrafast, making an all optical magnetic data recording scheme possible. This turned out to be indeed the case. Stanciu et al. [42] showed in 2007 the all optical switching of magnetization in a ferrimagnetic metal.

The observation of all optical switching (AOS) gained a lot of interest [43–49] as the phenomenon is of interest from both a scientific and application point of view. It was discovered that the switching process occurred due to a combination of ultrafast demagnetization, as discussed in the previous subsection, with breaking and restoring of the exchange coupling on the femtosecond timescale. During the switching process the ferrimagnetic metal becomes for a short time ferromagnetic [44].

From a technologically point, AOS is interesting as it has characteristics that are interesting for data storage: the switching process is fast and energy efficient. Furthermore compared to HAMR/TAMR the switching scheme is more simple: as where for HAMR/TAMR a magnetic field is still necessary, for AOS this is not needed.

For data storage, a disadvantage is that AOS is based on optics and thus is limited by the diffraction limit. As visible to infrared light is used in the AOS experiments it is necessary to go well below the diffraction limit to show that AOS can compete with the data densities as obtained with the storage techniques as described earlier. Although significant progress [47, 50] has been made in reducing the optically switched domain, with a record of 150 nm as is shown in Fig. 1.5, further downscaling is required.

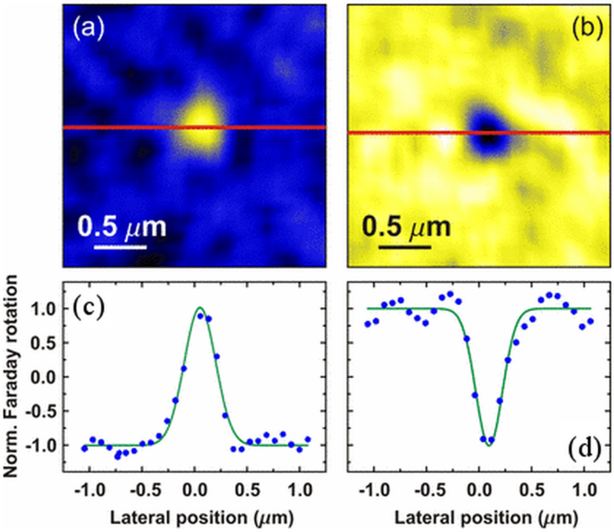

Figure 1.5: All optical switching in TbFeCo. The switched areas are as small as 150 nm in diameter. (a) and (b) show optical switched areas in oppositely oriented background magnetization. (c) shows the line traces along the two red lines in (a) and (b). This figure is adapted from Ref. [50].

1.3.3 Photo-magnetic effects

The observation of optically induced demagnetization and all optical switching is basically a result of ultra fast heating of the sample. This, however, involves depositing a large amount of energy into the sample, which needs to be dissipated afterwards, thus limiting the repetition rate of the impact. It would be more interesting to have a direct interaction between the femtosecond light pulse and the magnetization that acts on the same timescale as the laser pulse. It was discovered that this kind of light-magnetism interactions indeed exists. The most clear signature of these interactions is a polarization dependence of the observed magnetization dynamics. These light induced interactions can be divided in photo-magnetic (absorption related) and opto-magnetic (non-absorption related) effects.

In Ref. [51] and [52] magnetic precession was observed after illumination of a garnet film with a femtosecond pump pulse. It was observed that when the polarization angle of the linearly polarized pump pulse was changed, the amplitude of the precession changed as well. For some polarization angles there were even no oscillations excited. Together with a decrease in the amplitude of the oscillation with an increase in the external field, it was concluded that these oscillations originated from a long living change in H_{ani}.

The polarization dependence of this change in anisotropy can be explained by the polarization dependence of an optical induced electron transfer between ions in different sites [52]. The changed electronic state can simultaneously change the magnetic properties of the sample as well. As the electron transfer is initiated by the absorption of a photon this effect is called a photo-magnetic effect. Similar effects are observed in other materials as well, for example in nickel oxide [53, 54] or GaMnAs [55, 56].

1.3.4 Opto-magnetic effects

Next to the photo-induced effects another group of non-thermal effects exists. This is the group of effects that does not depend on an absorption process and is therefore called opto-magnetic effects. The origin of these effects are ascribed to the inverse processes of the well known magneto-optical effects like the Faraday and Cotton-Mouton effect [57]. Thus these opto-magnetic effects are called the inverse Faraday [51, 52, 58] or inverse Cotton-Mouton effect [59, 60]. Their existence was theoretically first described by Pitaevski [61] and later as well by Pershan et al. who also did the first experimental observations [62]. While the inverse Faraday effect as discussed above describes the effect of circularly polarized light, the inverse Cotton-Mouton effect describes a similar effect for linearly polarized light.

While thermal and photo-magnetic effects affect H_{ani} in a sample, the opto-magnetic effects can be described with the effective field H_{imp}. These effects act only on the magnetization in the presence of the light and are therefore called impulsive. Notice that photo-magnetic effects can be present for a while after the pump pulse already left the sample.

An example of magnetization dynamics excited by the inverse Faraday effect can be found in Refs. [58] and [51]. In those references it was demonstrated that with circularly polarized light of opposite helicity, magnetic precession was excited with a difference in their initial phase of 180 deg. This phase change was explained by the presence of an effective inverse Faraday field directed along or opposite to the light propagation direction during the presence of the pulse in the sample. Such an effective field causes the magnetization, initially in plane magnetized along an external field, to precess clockwise or anti-clockwise in the sample plane. After the pulse and thus the effective field has left the sample, a precession will start around the external field. The direction of this precession will be independent of the used light helicity, however, due to the clockwise or counter-clockwise rotation of the magnetization in the presence of the light pulse, after the pulse is gone the out of plane magnetization will increase first in the direction of the light propagation or first in the opposite direction, causing a difference of 180 deg in the initial phase of the oscillations excited with opposite circular polarizations. The clockwise and counter clockwise rotation are shown in Fig. 1.6.

For the opto-magnetic effects known up to now the direction of the effective field, and thus the direction of the change in magnetization has been shown to be controllable with the polarization of the light [51, 52, 58–60].

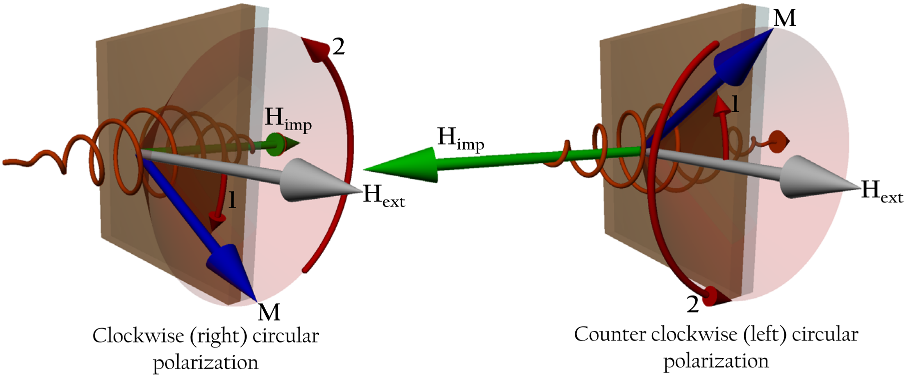

Figure 1.6: The effect of the effective inverse Faraday Field on the magnetization for the two helicities of light. First the magnetization precesses along the trajectory indicated with the number 1. Then if the light pulse is gone a second precession starts along the trajectory indicated with the number 2. Notice the difference in the starting direction for the two different helicities of light. The figures are based on similar figures in Ref. [52].

1.4 Scope of this thesis

This thesis aims to contribute to the understanding of magnetization dynamics and the applicability of all optical switching. To this end this thesis is devoted to various aspects of it, such as (i) using AOS at the nanoscale; (ii) studying the details of photo- and opto-magnetic effects, and (iii) investigation of the formation and properties of a magnon Bose-Einstein condensate. It is therefore divided in three different parts. After treating first some basic theory and the experimental tools in Chapter 2, the three parts will be divided over Chapters 3 to 6 as in the list below.

- The main question addressed in Chapter 3 will be if plasmonic antennas can be used to bring down the size of a domain written by all optical switching. With simulations we will show which domain size can be expected and what the most important design rules are for the geometry of the antenna. These simulations are followed by a demonstration of antenna induced all optical switching.

- In Chapters 4 and 5 a detailed study of the magnetization dynamics in a bismuth iron garnet thin film will be shown. In Chapter 4 a non-thermal polarization independent opto-magnetic effect is found that was not yet reported before. Furthermore the field dependence of the Gilbert damping is explained with a simple model based on a spread in the anisotropy of the sample.

- Chapter 5 focuses on a spectral study of the magnetization dynamics and shows a pump induced change in the magneto-optical constants. This change in the magneto-optical constants is used to explain other phenomena in the measured magnetization dynamics.

- In Chapter 6 the coherence of the magnetization dynamics is studied in a Bose-Einstein condensate of magnons. The main question we try to answer in this chapter is what is the maximum degree of coherence of the condensate.

References

[1] Y. Goto, N. Nakamura, A. Mituzani, H. Chiba, and K. Watanabe, "Head disk interface technologies for high recording density and reliability," Fujitsu Sci. Tech. J. **42**, 113 (2006).

[2] I. Tagawa, S. Ikeda, and Y. Uehara, "High-performance write head design and materials," Fujitsu Sci. Tech. J. **37**, 164 (2001).

[3] T. Schrefl, M. E. Schabes, D. Suess, and M. Stehno, "Dynamic micromagnetic write head fields during magnetic recording in granular media," Magnetics, IEEE Transactions on **40**, 2341 (2004).

[4] R. Wood, Y. Hsu, and M. Schultz, "Perpendicular magnetic recording technology (white paper)," Hitachi (2007).

[5] S. N. Piramanayagam, "Perpendicular recording media for hard disk drives," Journal of Applied Physics **102**, 011301 (2007).

[6] "Perpendicular recording diagram," (June 2014), http://en.wikipedia.org/wiki/File:Perpendicular_Recording_Diagram.svg.

[7] M. Kryder, E. Gage, T. McDaniel, W. Challener, R. Rottmayer, G. Ju, Y.-T. Hsia, and M. Erden, "Heat assisted magnetic recording," Proceedings of the IEEE **96**, 1810 (2008).

[8] W. L. Barnes, A. Dereux, and T. W. Ebbesen, "Surface plasmon subwavelength optics," Nature **424**, 824 (2003).

[9] L. Novotny and N. van Hulst, "Antennas for light," Nat Photon **5**, 83 (2011).

[10] K. Matsumoto, A. Inomata, and S.-Y. Hasagawa, "Thermally assisted magnetic recording," Fujitsu Sci. Tech. J. **42**, 158 (2006).

[11] W. A. Challener, C. Peng, A. V. Itagi, D. Karns, W. Peng, Y. Peng, X. Yang, X. Zhu, N. J. Gokemeijer, Y.-T. Hsia, G. Ju, R. E. Rottmayer, M. A. Seigler, and E. C. Gage, "Heat-assisted magnetic recording by a near-field transducer with efficient optical energy transfer," Nat Photon **3**, 220 (2009).

[12] B. C. Stipe, T. C. Strand, C. C. Poon, H. Balamane, T. D. Boone, J. A. Katine, J.-L. Li, V. Rawat, H. Nemoto, A. Hirotsune, O. Hellwig, R. Ruiz, E. Dobisz, D. S. Kercher, N. Robertson, T. R. Albrecht, and B. D. Terris, "Magnetic recording at 1.5 Pb m^{-2} using an integrated plasmonic antenna," Nat. Photonics **4**, 484 (2010).

[13] C. Chappert, A. Fert, and F. N. Van Dau, “The emergence of spin electronics in data storage,” Nat. Mater. **6**, 813 (2007).

[14] J. M. Daughton, “Magnetic tunneling applied to memory (invited),” Journal of Applied Physics **81**, 3758 (1997).

[15] M. Julliere, “Tunneling between ferromagnetic films,” Physics Letters A **54**, 225 (1975).

[16] J. S. Moodera, L. R. Kinder, T. M. Wong, and R. Meservey, “Large magnetoresistance at room temperature in ferromagnetic thin film tunnel junctions,” Phys. Rev. Lett. **74**, 3273 (1995).

[17] T. Miyazaki and N. Tezuka, “Giant magnetic tunneling effect in Fe/Al_2O_3/Fe junction,” Journal of Magnetism and Magnetic Materials **139**, L231 (1995).

[18] J. Slonczewski, “Current-driven excitation of magnetic multilayers,” Journal of Magnetism and Magnetic Materials **159**, L1 (1996).

[19] L. Berger, “Emission of spin waves by a magnetic multilayer traversed by a current,” Phys. Rev. B **54**, 9353 (1996).

[20] F. J. Albert, J. A. Katine, R. A. Buhrman, and D. C. Ralph, “Spin-polarized current switching of a Co thin film nanomagnet,” Applied Physics Letters **77**, 3809 (2000).

[21] L. D. Landau and E. M. Lifshitz, “On the theory of the dispersion of magnetic permeability in ferromagnetic bodies,” Phys. Z. Sowjet. **8**, 153 (1935).

[22] T. Gilbert, “A phenomenological theory of damping in ferromagnetic materials,” Magnetics, IEEE Transactions on **40**, 3443 (2004).

[23] I. Tudosa, C. Stamm, A. B. Kashuba, F. King, H. C. Siegmann, J. Stöhr, G. Ju, B. Lu, and D. Weller, “The ultimate speed of magnetic switching in granular recording media,” Nature **428**, 831 (2004).

[24] I. Tudosa, *Magnetization Dynamics Using Ultrashort Magnetic Field Pulses*, Ph.D. thesis, Stanford University (2005).

[25] B. Kalinikos, “Excitation of propagating spin waves in ferromagnetic films,” Microwaves, Optics and Antennas, IEE Proceedings H **127**, 4 (1980).

[26] J. Kisielewski, *Controlling the Magnetic Anisotropy in UltraThin Metallic Films*, Ph.D. thesis, Radboud University Nijmegen (2013).

[27] G. Counil, J.-V. Kim, T. Devolder, C. Chappert, K. Shigeto, and Y. Otani, “Spin wave contributions to the high-frequency magnetic response of thin films obtained with inductive methods,” Journal of Applied Physics **95**, 5646 (2004).

[28] M. Djordjevic, G. Eilers, A. Parge, M. Münzenberg, and J. S. Moodera, "Intrinsic and nonlocal Gilbert damping parameter in all optical pump-probe experiments," Journal of Applied Physics **99**, 08F308 (2006).

[29] S. Serrano-Guisan, K. Rott, G. Reiss, and H. W. Schumacher, "Inductive and magneto-resistive measurements of Gilbert damping in Ni 81 Fe 19 thin films and microstructures," Journal of Physics D: Applied Physics **41**, 164015 (2008).

[30] J. Walowski, M. D. Kaufmann, B. Lenk, C. Hamann, J. McCord, and M. Münzenberg, "Intrinsic and non-local Gilbert damping in polycrystalline nickel studied by Ti:sapphire laser fs spectroscopy," Journal of Physics D: Applied Physics **41**, 164016 (2008).

[31] H.-S. Song, K.-D. Lee, J.-W. Sohn, S.-H. Yang, S. S. P. Parkin, C.-Y. You, and S.-C. Shin, "Observation of the intrinsic Gilbert damping constant in Co/Ni multilayers independent of the stack number with perpendicular anisotropy," Applied Physics Letters **102**, 102401 (2013).

[32] H. C. Stöhr, J. Siegmann, *Magnetism, From Fundamentals to Nanoscale Dynamics* (Springer, 2006).

[33] S. N. Bose, "Plancks gesetz und lichtquantenhypothese," Z. Phys. **26**, 178 (1924).

[34] A. Einstein, "Quantentheorie des einatomigen idealen gases. part I," Sber. Preuss. Akad. Wiss. **22**, 261 (1924).

[35] S. O. Demokritov, V. E. Demidov, O. Dzyapko, G. A. Melkov, A. A. Serga, B. Hillebrands, and A. N. Slavin, "Bose-Einstein condensation of quasi-equilibrium magnons at room temperature under pumping," Nature **443**, 430 (2006).

[36] O. Dzyapko, V. E. Demidov, S. O. Demokritov, G. A. Melkov, and V. L. Safonov, "Monochromatic microwave radiation from the system of strongly excited magnons," Appl. Phys. Lett. **92**, 162510 (2008).

[37] A. G. Gurevich and G. A. Melkov, *Magnetization Oscillations and Waves* (CRC Press, 1996).

[38] E. Beaurepaire, J.-C. Merle, A. Daunois, and J.-Y. Bigot, "Ultrafast spin dynamics in ferromagnetic nickel," Phys. Rev. Lett. **76**, 4250 (1996).

[39] A. Kirilyuk, A. V. Kimel, and Th. Rasing, "Ultrafast optical manipulation of magnetic order," Rev. Mod. Phys. **82**, 2731 (2010).

[40] B. Koopmans, G. Malinowski, F. Dalla Longa, D. Steiauf, M. Fahnle, T. Roth, M. Cinchetti, and M. Aeschlimann, "Explaining the paradoxical diversity of ultrafast laser-induced demagnetization," Nat Mater **9**, 259 (2010).

[41] M. Battiato, K. Carva, and P. M. Oppeneer, "Superdiffusive spin transport as a mechanism of ultrafast demagnetization," Phys. Rev. Lett. **105**, 027203 (2010).

[42] C. D. Stanciu, F. Hansteen, A. V. Kimel, A. Kirilyuk, A. Tsukamoto, A. Itoh, and Th. Rasing, "All-optical magnetic recording with circularly polarized light," Phys. Rev. Lett. **99**, 047601 (2007).

[43] K. Vahaplar, A. M. Kalashnikova, A. V. Kimel, D. Hinzke, U. Nowak, R. Chantrell, A. Tsukamoto, A. Itoh, A. Kirilyuk, and Th. Rasing, "Ultrafast path for optical magnetization reversal via a strongly nonequilibrium state," Phys. Rev. Lett. **103**, 117201 (2009).

[44] I. Radu, K. Vahaplar, C. Stamm, T. Kachel, N. Pontius, H. A. Durr, T. A. Ostler, J. Barker, R. F. L. Evans, R. W. Chantrell, A. Tsukamoto, A. Itoh, A. Kirilyuk, Th. Rasing, and A. V. Kimel, "Transient ferromagnetic-like state mediating ultrafast reversal of antiferromagnetically coupled spins," Nature **472**, 205 (2011).

[45] J. H. Mentink, J. Hellsvik, D. V. Afanasiev, B. A. Ivanov, A. Kirilyuk, A. V. Kimel, O. Eriksson, M. I. Katsnelson, and T. Rasing, "Ultrafast spin dynamics in multisublattice magnets," Phys. Rev. Lett. **108**, 057202 (2012).

[46] A. R. Khorsand, M. Savoini, A. Kirilyuk, A. V. Kimel, A. Tsukamoto, A. Itoh, and Th. Rasing, "Role of magnetic circular dichroism in all-optical magnetic recording," Phys. Rev. Lett. **108**, 127205 (2012).

[47] M. Savoini, R. Medapalli, B. Koene, A. R. Khorsand, L. Le Guyader, L. Duò, M. Finazzi, A. Tsukamoto, A. Itoh, F. Nolting, A. Kirilyuk, A. V. Kimel, and Th. Rasing, "Highly efficient all-optical switching of magnetization in GdFeCo microstructures by interference-enhanced absorption of light," Phys. Rev. B **86**, 140404 (2012).

[48] T. Ostler, J. Barker, R. Evans, R. Chantrell, U. Atxitia, O. Chubykalo-Fesenko, S. El Moussaoui, L. Le Guyader, E. Mengotti, L. Heyderman, F. Nolting, A. Tsukamoto, A. Itoh, D. Afanasiev, B. Ivanov, A. Kalashnikova, K. Vahaplar, J. Mentink, A. Kirilyuk, Th. Rasing, and A. Kimel, "Ultrafast heating as a sufficient stimulus for magnetization reversal in a ferrimagnet," Nat Commun **3**, 666 (2012).

[49] C. E. Graves, A. H. Reid, T. Wang, B. Wu, S. de Jong, K. Vahaplar, I. Radu, D. P. Bernstein, M. Messerschmidt, L. Müller, R. Coffee, M. Bionta, S. W. Epp, R. Hartmann, N. Kimmel, G. Hauser, A. Hartmann, P. Holl, H. Gorke, J. H. Mentink, A. Tsukamoto, A. Fognini, J. J. Turner, W. F. Schlotter, D. Rolles, H. Soltau, L. Strüder, Y. Acremann, A. V. Kimel, A. Kirilyuk, Th. Rasing, J. Stöhr, A. O. Scherz, and H. A. Dürr, "Nanoscale spin reversal by non-local angular momentum transfer following ultrafast laser excitation in ferrimagnetic GdFeCo," Nat Mater **12**, 293 (2013).

[50] M. Finazzi, M. Savoini, A. R. Khorsand, A. Tsukamoto, A. Itoh, L. Duò, A. Kirilyuk, Th. Rasing, and M. Ezawa, "Laser-induced magnetic nanostructures with tunable topological properties," Phys. Rev. Lett. **110**, 177205 (2013).

[51] F. Hansteen, A. Kimel, A. Kirilyuk, and Th. Rasing, "Femtosecond photomagnetic switching of spins in ferrimagnetic garnet films," Phys. Rev. Lett. **95**, 047402 (2005).

[52] F. Hansteen, A. Kimel, A. Kirilyuk, and Th. Rasing, "Nonthermal ultrafast optical control of the magnetization in garnet films," Phys. Rev. B **73**, 014421 (2006).

[53] N. P. Duong, T. Satoh, and M. Fiebig, "Ultrafast manipulation of antiferromagnetism of NiO," Phys. Rev. Lett. **93**, 117402 (2004).

[54] T. Satoh, N. P. Duong, and M. Fiebig, "Coherent control of antiferromagnetism in NiO," Phys. Rev. B **74**, 012404 (2006).

[55] D. M. Wang, Y. H. Ren, X. Liu, J. K. Furdyna, M. Grimsditch, and R. Merlin, "Light-induced magnetic precession in (Ga,Mn)As slabs: Hybrid standing-wave Damon-Eshbach modes," Phys. Rev. B **75**, 233308 (2007).

[56] Y. Hashimoto, S. Kobayashi, and H. Munekata, "Photoinduced precession of magnetization in ferromagnetic (Ga,Mn)As," Phys. Rev. Lett. **100**, 067202 (2008).

[57] A. K. Zvezdin and V. A. Kotov, *Modern magnetoopticcs and magnetooptical materials* (Institute of Physics Publishing, Bristol and Philadelphia, 1997).

[58] A. V. Kimel, A. Kirilyuk, P. A. Usachev, R. V. Pisarev, A. M. Balbashov, and Th. Rasing, "Ultrafast non-thermal control of magnetization by instantaneous photomagnetic pulses," Nature **435**, 655 (2005).

[59] A. M. Kalashnikova, A. V. Kimel, R. V. Pisarev, V. N. Gridnev, A. Kirilyuk, and Th. Rasing, "Impulsive generation of coherent magnons by linearly polarized light in the easy-plane antiferromagnet $FeBO_3$," Phys. Rev. Lett. **99**, 167205 (2007).

[60] A. M. Kalashnikova, A. V. Kimel, R. V. Pisarev, V. N. Gridnev, P. A. Usachev, A. Kirilyuk, and Th. Rasing, "Impulsive excitation of coherent magnons and phonons by subpicosecond laser pulses in the weak ferromagnet $FeBO_3$," Phys. Rev. B **78**, 104301 (2008).

[61] L. P. Pitaevskii, "Electric forces in a transparent dispersive medium," Sov. Phys. JETP **12**, 1008 (1961).

[62] P. S. Pershan, J. P. van der Ziel, and L. D. Malmstrom, "Theoretical discussion of the inverse Faraday effect, Raman scattering, and related phenomena," Phys. Rev. **143**, 574 (1966).

Chapter 2

Theoretical and experimental tools

A variety of different experimental techniques is used in this thesis plus a specialized numerical computational approach. In this chapter all these techniques are briefly explained. First we will give a brief general introduction to pump-probe experiments. Second, we summarize the necessary theory for the interaction between electromagnetic waves and magnetic materials. More specifically we discuss the differences between the microwave, optical and X-ray regions of the electromagnetic spectrum. Next, a brief description of the laser systems that we employ is given. After that we continue with the three different pump-probe schemes that are used in this thesis. The fifth section explains the numerical technique that is used in Chapter 3. In the last section a short summary is given.

2.1 Introduction

To obtain advanced information about physical processes or material properties it is often not enough to only perform a probe experiment. For this reason a large number of experiments is based on a pump-probe scheme, where an action of a certain stimulus ("pump") brings a system out of equilibrium, followed by a probe action which probes the pump induced change in the system of interest. Notice that for future applications the ability to actively control the processes in and properties of a material with some kind of pump is very desirable as well.

The pump action could bring the system temporarily out of equilibrium or it could bring the system to a new equilibrium state. For those two possibilities the requirements for the pump-probe experiments differ significantly. In the former case the experiment needs to have a time resolution well below the typical timescale related to the process of interest, while in the latter case a time resolution is not a necessity. In this chapter examples of both type of pump-probe experiments will be given.

In this work different regions of the electromagnetic (EM) spectrum are used for the pump or probe action. The advantage of EM radiation is that the frequency of the radiation can be chosen such that it matches with the typical energy scales related to the phenomena of interest. For this reason, in this thesis we do not limit ourselves to a specific range of the EM spectrum. We will use the spectrum from X-rays to optical frequencies and all the way up to microwaves. Hereby we mainly use, but also study, the interaction between the radiation and magnetic properties of a material. Another advantage in the optical part of the spectrum is the availability of ultrashort laser pulses. The use of such short laser pulses makes it possible to measure with an extremely high time resolution. The recent development of X-ray free electron lasers has brought this high (femtosecond) resolution to the X-ray regime as well.

2.2 Interaction of electromagnetic radiation with magnetization

For the experiments performed in this thesis the interaction between EM radiation and magnetism is very important. The effect of magnetism on the EM radiation is used to obtain information about the effect of the radiation on magnetism. In the different regions in the EM spectrum the interaction has a different origin. In this section we will discuss the most important characteristics of the interactions that play a role in the different EM regions.

2.2.1 Microwave region

With magnetic fields of a few kOe the ferromagnetic precession frequency is typically in the GHz range. Thus with microwaves the magnetic precession can be driven resonantly. The magnetization will directly follow the oscillation of the electromagnetic field. Theoretically this oscillation is best described in terms of the high frequency magnetic susceptibility tensor $\hat{\chi}$, which relates the ac component of the magnetization, $\mathbf{m}_{\mathrm{ac}}$ to the ac magnetic field component of the microwaves $\mathbf{h}_{\mathrm{ac}}$ [1]

$$\mathbf{m}_{\mathrm{ac}} = \hat{\chi}\mathbf{h}_{\mathrm{ac}}. \tag{2.1}$$

Hence the total magnetization and magnetic field is given by

$$\mathbf{m} = \mathbf{m}_{\mathrm{dc}} + \mathbf{m}_{\mathrm{ac}}, \quad \mathbf{H} = \mathbf{h}_{\mathrm{dc}} + \mathbf{h}_{\mathrm{ac}}. \tag{2.2}$$

With the static field along the z direction and the oscillating part in the xy-plane it can be shown that by using the linearized Landau Lifshitz equation, thus assuming small oscillation amplitudes, the susceptibility is given by [1]

$$\hat{\chi} = \begin{bmatrix} \chi & \mathrm{i}\chi_{\mathrm{a}} & 0 \\ -\mathrm{i}\chi_{\mathrm{a}} & \chi & 0 \\ 0 & 0 & 0 \end{bmatrix}. \tag{2.3}$$

with

$$\chi = \tfrac{\gamma m_{\mathrm{dc}}\omega_{\mathrm{H}}}{\omega_{\mathrm{H}}^2-\omega^2} \quad \chi_{\mathrm{a}} = \tfrac{\gamma m_{\mathrm{dc}}\omega}{\omega_{\mathrm{H}}^2-\omega^2}. \tag{2.4}$$

Here ω is the frequency of $\mathbf{h}_{\mathrm{ac}}$ and the Larmor precession ω_{H} is given by

$$\omega_{\mathrm{H}} = \gamma h_{\mathrm{dc}}. \tag{2.5}$$

Eq. 2.4 gives a resonant condition for $\omega = \omega_{\mathrm{H}}$ and thus by matching the microwave driving frequency and the applied field it is possible to resonantly excite magnetic precession. Notice that in the derivation of Eq. 2.4 we neglected damping. With damping included the oscillation amplitude at resonance will not be infinite. Furthermore in reality the resonance frequency is not only given by the external applied field as suggested by Eq. 2.5, but by the total effective field acting on the magnetization, which includes the anisotropy and demagnetizing field.

In the above discussion only a single homogeneous ($k = 0$) mode is described that precesses uniformly in the entire sample. However in a magnetic sample also traveling modes or spin waves are allowed as already mentioned in Chapter 1. These spin waves are also always present in thermal equilibrium due to thermal fluctuations. Due to the presence of other modes and the nonlinear character of the Landau Lifshitz Gilbert equation, coupling between the uniform precessional mode and spin waves with k-vectors of opposite sign will occur if the excitation field is intense enough [1]. In Chapter 6 we will use this so called parametric excitation mechanism to excite spin waves at half the microwave pumping frequency and with finite k-vectors.

Although in this subsection we explained the occurrence of magnetic resonance with the magnetic susceptibility tensor $\hat{\chi}$, a similar description can be given in terms of the magnetic permeability tensor, $\hat{\mu}$. This permeability tensor is related to the susceptibility by $\hat{\mu} = \hat{I} + 4\pi\hat{\chi}$ where I is a unit tensor. In fact the largest difference in the interaction between electromagnetic radiation and magnetism in the microwave and optical plus X-ray regime is that in the microwave regime this interaction is described by oscillating magnetic fields of the electromagnetic wave (magnetic dipole approximation), while in the optical and X-ray regime this description is based on the electric field (electric dipole approximation). Therefore in the next subsection we will use the description of the electric permittivity, ϵ to explain the interaction between light and magnetism.

2.2.2 Optical and X-ray region

In the optical and X-ray region the interaction between the EM radiation and the magnetization is originating from electric dipole transitions and the different response of those transitions to the opposite angular momenta of the two possible light helicities [2]. However, due to the difference in the energy scales related to the two EM regions a large difference exists between the observed effects in the optical and in the X-ray regions.

In comparison to their transition energy, in the optical regime the dipole transitions are relatively broad [3]. While in the X-ray region, narrow, well defined inter band transitions are dominating the optical response of the material. With the proper sum rules quantitative information about the magnetic properties of the material, like the magnetic spin moment and the orbital magnetic moment, can be obtained [4]. While in the optical regime mainly the real part of the refractive index is of importance, in the X-ray regime it is the imaginary part, i.e. the extinction coefficient, that is of most importance.

Although there are differences in the observed effects in the two EM spectral regions the physics can be described with the same physical model. The dielectric tensor $\hat{\epsilon}$ of an isotropic material in the presence of a magnetic field is given by

$$\hat{\epsilon} = \begin{bmatrix} \epsilon_0 & \mathrm{i}\epsilon_{\mathrm{xy}}(m_{\mathrm{z}}) & 0 \\ \mathrm{i}\epsilon_{\mathrm{xy}}(m_{\mathrm{z}}) & \epsilon_0 & 0 \\ 0 & 0 & \epsilon_0 \end{bmatrix}. \tag{2.6}$$

Here m_{z} is the component of the magnetization along the propagation direction of the light. In the absence of magnetization, $\epsilon_{xy} = 0$. All matrix elements are complex quantities.

The eigenvectors of the matrix in Eq. (2.6) are the two helicities of circular polarization and it can be shown [2, 5] that the eigenvalues for the two helicities, $n_{\pm}^2$ are given by

$$n_{\pm}^2 = \epsilon_0 \pm \epsilon_{\mathrm{xy}}(m_{\mathrm{z}}). \tag{2.7}$$

Here n_+ and n_- are the complex refractive indices for the two opposite circular polarizations.

The difference between the real parts of n_+ and n_- cause circular polarization of opposite helicity to travel with different velocities through the material. Hence when linear polarization, which can be decomposed in the two circular polarizations, is traveling through a magnetic material, the phase between the opposite circular polarization components will change. This causes the linear polarization to rotate. This effect is called the Faraday effect [6]. Quantitatively the rotation angle θ, is given by [2]

$$\theta = \frac{\omega}{2c}\left[\mathrm{Re}(n_+) - \mathrm{Re}(n_-)\right] L. \tag{2.8}$$

Here ω is the angular frequency of the light, c the speed of light, and L is the path length of the light. For magnetization directions parallel and anti-parallel to the propagation direction of the light, the rotation θ will be in the opposite direction.

The attenuation factor A of light is given by [7]

$$A = 1 - \mathrm{e}^{-\alpha L}, \tag{2.9}$$

where α is the attenuation coefficient which is defined as

$$\alpha = \frac{2\omega \mathrm{Im}(n)}{c}. \tag{2.10}$$

The difference in attenuation for left and right circular polarizations is now given by

$$\Delta A = A_+ - A_- = \mathrm{e}^{-\alpha_- L} - \mathrm{e}^{-\alpha_+ L}. \tag{2.11}$$

The occurrence of this difference in attenuation for opposite helicities is called magnetic circular dichroism (MCD). Notice that if linear polarized light is sent through a material with MCD the polarization will become elliptical.

In the X-ray region at the absorption edges of the material, the differences in the imaginary part of the refractive indices for the two different helicities are relatively large. The attenuation differs by several tens of percentage for thin film samples [4]. The real part of n is approximately one in the X-ray region.

In the optical regime the differences in attenuation are much smaller. For example in GdFeCo the MCD was measured to be only about 1.4% [8]. However, the differences in the real part of the refractive index in the optical regime are large enough to measure a significant Faraday rotation. In materials with large magneto-optical constants (e.g. GdFeCo and TbFeCo [9] or bismuth iron garnet [10]) this rotation can be of the order of several tens of millidegree per nanometer.

Although X-rays have a larger MCD signal and give the possibility to obtain quantitative information about the magnetization, in this thesis we use the X-rays mainly for their shorter wavelength and thus their ability to image with a higher spatial resolution as compared to the visible part of the EM spectrum.

2.3 Femtosecond pulsed laser systems

For the optical measurements we make use of femtosecond laser systems. In Chapter 6 this is a mode locked oscillator [11, 12], while in Chapters 4 and 5 an amplified laser system [13] is employed in combination with an optical parametric amplifier (OPA) [14].

The mode locked oscillator is a Spectra Physics 100 fs Tsunami Ti:Sapphire laser with a repetition rate of about 80 MHz. It gives most output power when the wavelength is tuned to 800 nm, however it can be tuned over a range from 700 to 1050 nm. The oscillator is pumped with a continuous wave 532 nm Millenia diode pumped Nd:YVO_4 laser. This same oscillator is part of the amplified laser system as well.

For amplification a Spectra Physics Spitfire amplifier is used together with an Empower Nd:YLF seed laser. Together with the oscillator the output of this system are 40 fs, 800 nm amplified laser pulses at a repetition rate of 1 kHz. Part of this output light is then sent through a Spectra Physics OPA-880C, in which it is possible to tune the wavelength over a broad range. To use the full possible range of 0.3 to 3 μm the light path and nonlinear crystals have to be changed. In this thesis we only used the range from 450 to 530 nm.

2.4 Pump-probe techniques

For all experiments performed in this thesis some form of pump-probe technique is employed. However, there are significant differences in how these techniques are realized. The information about the physics of the magnetization dynamic processes that can be obtained with them is different as well. Here we will discuss the three different schemes. First we start with static imaging, followed by how we measure dynamics in the time domain and last we will show a pump-probe technique that measures in the frequency domain.

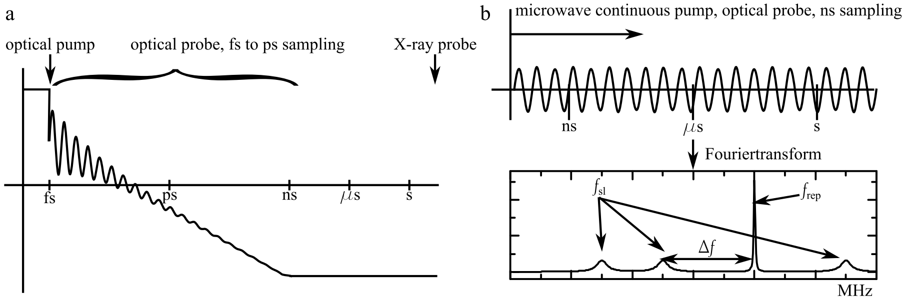

Figure 2.1: Schematic showing the differences between the three different pump-probe schemes that are used in this thesis. In (a) an optical pump excites magnetization dynamics. The timescale that is addressed with an all optical pump-probe scheme is indicated. With such a setup magnetization dynamics can be revealed. The X-ray probe is used on a timescale where all dynamics is already gone and where the system has reached a (new) equilibrium. In (b) the characteristics of the microwave pump - optical probe scheme is shown.

2.4.1 Static imaging of single pulse switching

In Chapter 3 we will use a static form of pump-probe. First an optical pump is used to induce a change in the magnetic state of the sample. It is assumed here that this change is stable in time. In a next step, that is independent of the pump event, we probe the new magnetic state. This gives the freedom to probe at any convenient time and with any suitable technique that is available. Here we use X-ray holographic imaging for the probe. This method of pump-probe results in a 2D image of the magnetic domain structure and does not give any information about the magnetization dynamics. The information that can be obtained about the magnetization of the sample with this setup is visualized and compared to the other techniques in Fig. 2.1(a).

Magnetic imaging with X-rays is based on X-ray magnetic circular dichroism. The absorption of circular polarized light by a magnetic material depends on the direction of the magnetic field and the helicity of the light [15]. If we would scan a focused circularly polarized X-ray beam over a thin film surface and record at every point the transmission it is possible to image the magnetic domain structure.

However, instead of scanning over the surface we illuminate the whole area of interest at once and use holography for imaging. In holographic imaging it is not the real space image that is recorded but the reciprocal scattering pattern. Due to interference of this scattering pattern with X-rays from a reference structure, it is possible to reconstruct the real space image with an inverse Fourier transform. We use the specific form of holography called “holography with extended reference by autocorrelation linear differential operation”(HERALDO), where the resolution is not determined by the size of the reference structure but by the sharpness of the edge of the reference structure [16].

Quantitatively we can describe the used Holography technique in the following way

[16]. The spatial variation in the light field in the sample plane is given by $o(x, y)$. As those variations are caused by the difference in transmission for opposite domains, $o(x, y)$ describes the domain structure that we are interested in. Furthermore, the field distribution at the reference structure is given by $r(x, y)$ and thus the total field distribution in the sample plane is given by

$$f(x, y) = o(x, y) + r(x, y). \tag{2.12}$$

The far field diffraction pattern is now given by the Fourier transform of the near-field field distribution given in Eq. (2.12) [7]

$$F(u, v) = \mathcal{F}[f(x, y)]. \tag{2.13}$$

However, in the far field we do not detect the field distribution $F(u, v)$, but the intensity distribution $|F(u, v)|^2$. The inverse Fourier transform of this intensity distribution gives

$$\mathcal{F}^{-1}[|F(u, v)|^2] = f \otimes f = o \otimes o + r \otimes r + o \otimes r + r \otimes o, \tag{2.14}$$

where $a \otimes b$ indicates the cross-correlation between a and b.

Now the idea of HERALDO is to find an n-th order linear differential operator $\mathcal{L}^{(n)}$, such that

$$\mathcal{L}^{(n)}[r(x, y)] = A\delta(x - x_0)\delta(y - y_0) + g(x, y). \tag{2.15}$$

Here A is an arbitrary complex constant, δ the Dirac delta function and $g(x, y)$ can be any arbitrary function. $\mathcal{L}^{(n)}$ is of the general form

$$\mathcal{L}^{(n)} = \sum_{k=0}^{n} a_k \frac{\partial^n}{\partial x^{n-k} \partial y^k}, \tag{2.16}$$

where a_k are constant coefficients.

If an operator that satisfies Eq. (2.15) is applied to Eq. (2.14) it can be shown that [16]

$$\begin{aligned} \mathcal{L}^{(n)}[f \otimes f] = \mathcal{L}^{(n)}[o \otimes o] + \mathcal{L}^{(n)}[r \otimes r] + (-1)^n o \otimes g + g \otimes o \\ + (-1)^n A^* o(x + x_0, y + y_0) + A o^*(x_0 - x, y_0 - y), \end{aligned} \tag{2.17}$$

where the $*$ indicates the complex conjugate.

The last two terms in the last equation are exactly the images of the domain structure that we want to know. To be able to obtain those images it is necessary that the images do not overlap with the other cross-correlation terms. The requirements to fulfill this condition are extensively discussed in Ref. [16] and can be summarized to the following three requirements. If the object can be contained in a circle with radius ρ, then:

- the reference feature responsible for the Dirac delta in Eq. (2.15) should be separated from the edge of the object by a distance of 2ρ to make sure the object is not overlapping with $\mathcal{L}^{(n)}[o \otimes o]$.

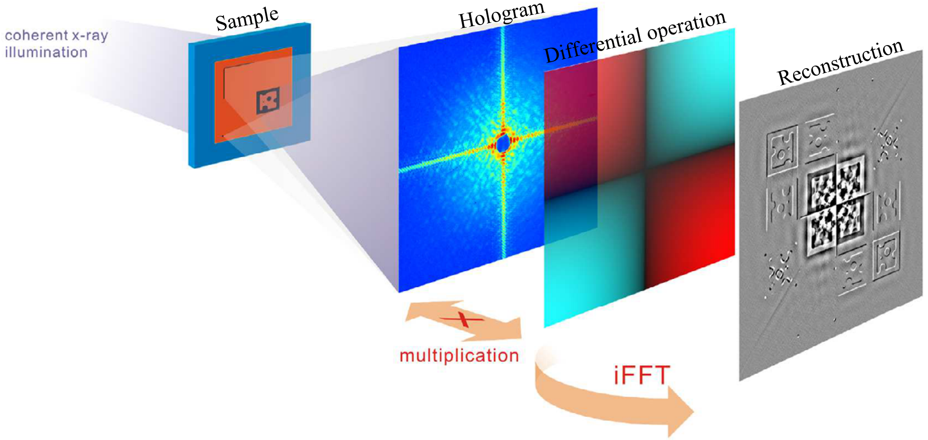

Figure 2.2: A schematic overview of the mathematical operations that are needed to be performed within the HERALDO scheme to obtain the spatial information about the sample structure. Adapted from Ref. [17].

- $g(x, y)$ and $g(-x, y)$ should be zero in a radius of 2ρ around the Dirac delta to prevent overlap between the object and $(-1)^n o \otimes g + g \otimes o$.

- $r \otimes r$ should be zero in a radius of ρ around the Dirac delta to prevent overlap between the object and the term $\mathcal{L}^{(n)}[r \otimes r]$.

Notice that for conventional Fourier holography with a single point reference hole, and thus $r(x, y) = A\delta(x - x_0)\delta(y - y_0)$ the right linear differential operator that satisfies Eq. (2.15) is the identity operator and $g(x, y) = 0$. Thus the main differences between the holography technique applied here and conventional single point reference holography is the use of a different shape of the reference hole and the application of a linear differential operator. The advantage to have more freedom of choice for the reference structure is that a structure can be chosen that can be fabricated with a high reproducibility and with sharp features. The imaging resolution is determined by how well the Dirac delta point can be approached. Thus the sharper the edge the closer the linear derivative operation will give a Dirac delta point.

In the measurements discussed in this thesis L-shaped reference holes are used. The resolution that can be obtained with this shape is demonstrated to be roughly 16 nm[17]. By applying a second order linear differential operator along the two arms of the L-shape, three Dirac delta points will be obtained at the corners of the L-shape. Each of them can be used to obtain the image of the domain structure. According to Eq. (2.15) the other two are then part of the function $g(x, y)$. In practice we do not apply the differential operator after the inverse Fourier transform but we perform the equivalent multiplication of the differential operation in Fourier space[16, 17], thus before the inverse Fourier transform is applied. In Fig. 2.2 the mathematical

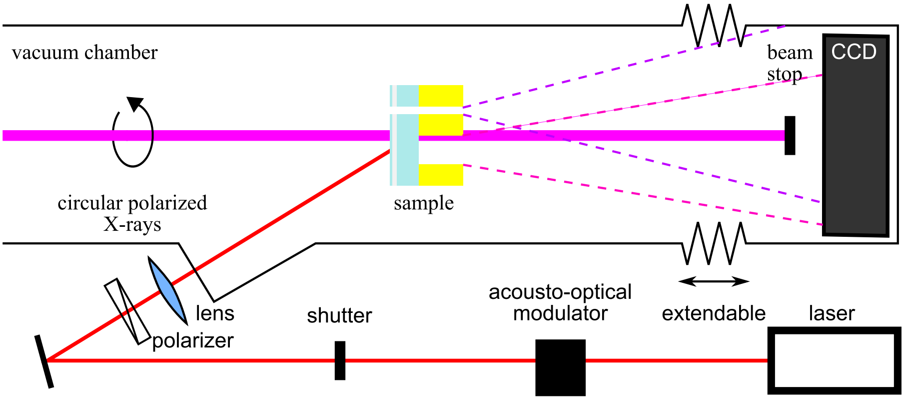

Figure 2.3: A schematic overview of the optical pump, X-ray probe setup for static imaging.

operations that are needed to be performed are graphically illustrated.

A schematic of the setup is shown in Fig. 2.3. The optical part of the setup consists of a pulsed Erbium doped fiber laser with a wavelength of 1030 nm. The pulses are about 120 fs long and fluences from 3 to 10 mJ/cm^2 are used. An acousto-optical modulator is employed to reduce the repetition rate of the laser from the MHz range to only a few Hz. In combination with a shutter this makes single pulse illumination possible.

In the X-ray part of the setup, Circularly polarized X-rays are transmitted through the sample that is placed in a vacuum chamber. Diffracted X-rays are detected by the CCD camera while the intense direct beam is blocked by a beam stop to protect the camera. Furthermore the vacuum chamber behind the sample is extendable such that we can control the k-vectors that can be detected.

In the presence of non-magnetic material on the sample the transmission through the sample will also contain features that are not related to the magnetic domain structure. To obtain the magnetic domain structure in such a situation the measurement has to be performed with both left and right circularly polarized light. By taking the difference between the two measured data sets, all non-magnetic features can be removed and the domain structure will be obtained. Instead if we are interested to obtain spatial information about the location of the non-magnetic materials we can take the sum of the measured data sets. An image obtained by taking the difference between the data sets is called a magnetic image while an image obtained by taking the sum of the data sets is called a charge image as it only shows spin independent absorption.

2.4.2 Dynamics: time domain

Another type of pump-probe is femtosecond optical pump-probe spectroscopy. For this method of pump-probe the amplified laser system is used together with the OPA.

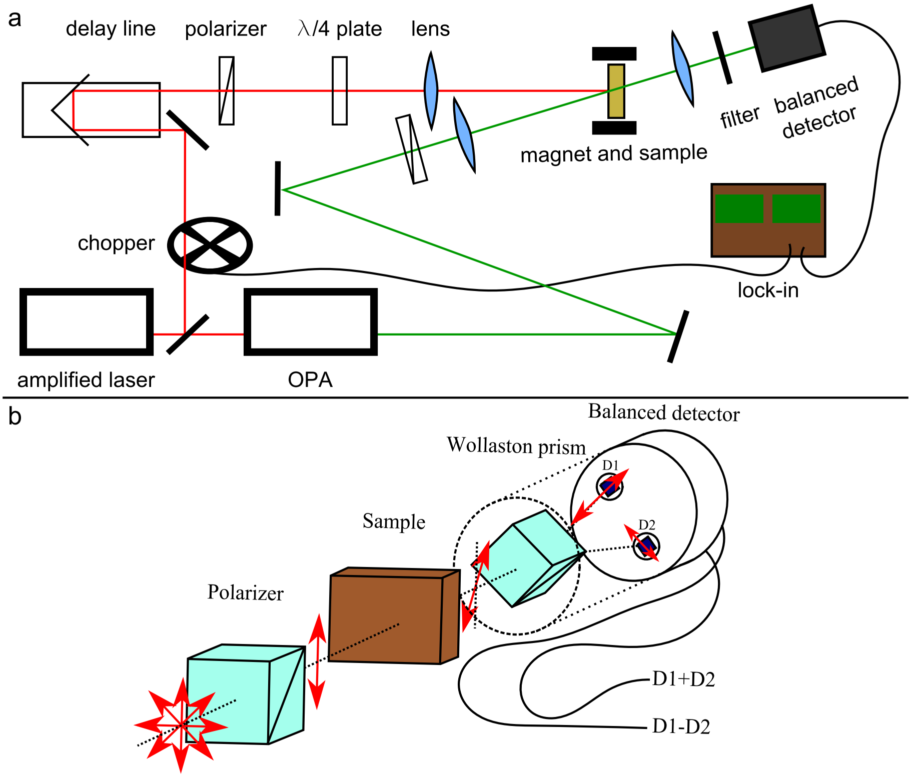

Figure 2.4: (a) A schematic overview of the all optical pump-probe setup that is used to measure magnetization dynamics. (b) A schematic overview of the basic elements in a magneto-optical measurement with a balanced detector scheme.

The pump is the direct output of the amplifier, 40 fs, 800 nm pulses at a repetition rate of 1 kHz. For the probe, part of the laser output is directed through the OPA such that it can be tuned over a range from 450 to 530 nm. The probe is always of a much lower intensity as compared to the pump and is used to measure the time dependent pump induced changes in the Faraday rotation. This type of pump-probe is used in Chapters 4 and 5. A sketch of the setup can be found in Fig. 2.4(a).

As pump and probe are created from the same laser output, they are synchronized in time. With a mirror on a horizontal translation stage placed in the pump beam path it is possible to accurately vary the optical path length of the pump with respect to that of the probe. By changing this path length the arrival time of the pump pulse with respect to that of the probe can be tuned. In other words the delay between the arrival of the probe pulse after that of the pump can be controlled, therefore this translation stage is also often named delay stage.

With a delay stage it is possible to measure the magnetization state with a time resolution of approximately the pulse duration of 40 fs. This is short enough to reveal magnetization dynamics in magnetic materials. The time scale addressed by this setup is shown in Fig. 2.1(a). Although this system is only used to measure at a single point, the spatial resolution is equal to the probe spot size, which in general is several tens of microns. For the measurement to deliver reliable results, the pump spot is always kept larger as compared to the probe spot such that the probed area can be assumed to be homogeneously excited.

Although to measure the Faraday rotation only two linear polarizers are necessary, here we replace the second polarizer with a Wollaston prism in combination with a balanced detector scheme as shown in Fig. 2.4(b). With a Wollaston prism two orthogonal polarizations are both sent in the forward direction with only a small angle between them. The balanced detector consists of two diode detectors such that both polarization components can be detected. The Wollaston prism is placed such that it decomposes the incoming polarization along the two axes that make an angle of +45 and -45 deg with respect to the polarization axis of the first polarizer. Electronic subtraction of the two obtained signals now gives a signal that is linearly proportional to the Faraday rotation if this rotation is small. By amplification of the difference signal, small rotation angles can be measured. By rotating the Wollaston prism by a defined angle and measuring the voltage difference, the detector can be calibrated to measure the rotation angle in degrees. Another advantage of the balanced detector is that besides the difference signal, the sum signal can be measured at the same time. This sum signal gives information about the transmission through the sample.

A further increase of the sensitivity is obtained by employing a lock-in amplifier (Stanford Research Systems, SR830). For the lock-in technique a chopper rotating at 500 Hz synchronized with the laser output of 1 kHz is placed in the pump beam path. Feeding the voltage from the balanced detector to the lock-in amplifier with the chopper frequency as the reference signal will give the pump induced signal at the output of the lock-in amplifier.

An in plane external field up to 5 kG is applied by an electromagnet. Furthermore some simple optical elements are used to control the polarization and intensity of the light.

2.4.3 Dynamics: frequency domain

In Chapter 6 again another type of pump-probe is utilized. Here a continuous microwave pump is used to excite magnetization precession in a sample while an optical 100 fs pulsed laser at a repetition rate of around 80 MHz is used as the probe. This probe is used as a carrier for the magnetization precession frequency. By feeding the probe signal after being detected by an avalanche photodiode (APD) to a frequency analyzer, the coherence of the magnetic precession can be determined. The frequency of the magnetization precession is imposed on the probe signal by the Faraday effect. In Fig. 2.1(b) the magnetization dynamics addressed with this technique can be compared with the other two pump-probe schemes discussed in this section. In Fig. 2.5 a sketch of the setup can be found.

A microwave generator (Anritsu MG3692C) supplies the microwaves and by a

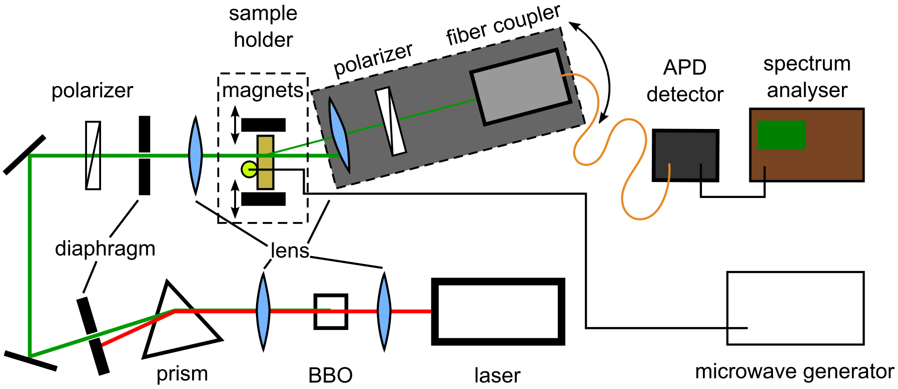

Figure 2.5: A schematic overview of the microwave continuous pump, optical pulsed probe setup to measure the coherence of the magnetic precession in the frequency domain.

coaxial cable they are send to the sample holder. This holder contains the sample and a microstripline. This stripline is connected to a cavity formed by a thin gold wire via a capacitor. This cavity is positioned directly on top of the sample such that a high microwave intensity is achieved at the desired position.

For the optical pulses the mode locked Ti:Sapphire oscillator is used. Active mode locking guarantees a high stability of the repetition rate, which is advantageous for the determination of the coherence of the magnetization precession. With a barium borate (BBO) crystal and the right tuning of the laser a wavelength of 495 nm is obtained. A prism is used to separate the fundamental and second harmonic light. The second harmonic is sent through a polarizer and a diafragm before being focused on the sample. After the sample the light is collimated again and send through a second polarizer. In a next step, the light is coupled into an optical fiber with a parabolic mirror. The collection optics are mounted on a rotation arm with the sample positioned at its rotation axis. This generates the freedom to collect the light that is scattered under any angle. This angular sensitivity is necessary as we are interested in light scattering from standing periodic patterns of spin waves. The fiber is connected to an APD-detector.

An in plane external magnetic field is applied with permanent magnets on a translation stage such that the amplitude of the field can be varied. Furthermore, as the gold wire is on top of the sample, we employ a high-resolution camera system to make sure that the light spot does not overlap with the gold wire.

The signal from the APD-detector is connected to an HP 8560A Portable Spectrum Analyzer. This analyzer performs a Fourier transform on the electrical signal and thus shows the frequency components that are present. The frequency components that will be visible, actually depend on the relative orientation of the two polarizers and the laser repetition frequency. It is therefore important to discuss the frequency components that are present quantitatively. Here we will make use of the Jones matrix formalism. After the first polarizer the polarization is horizontal

$$E = \begin{bmatrix} 1 \\ 0 \end{bmatrix}, \tag{2.18}$$

where we take the amplitude of the light to be normalized. Then it passes through the sample where it undergoes a Faraday rotation. In the matrix formalism this can be written as

$$F = \begin{bmatrix} \cos\phi & -\sin\phi \\ \sin\phi & \cos\phi \end{bmatrix}. \tag{2.19}$$

Here ϕ is the polarization rotation angle. This rotation angle is depending on the oscillating component of the magnetization out of plane, hence

$$\phi = A \sin \omega_{\mathrm{mag}} t. \tag{2.20}$$

Here A is the oscillation amplitude and ω_{mag} the magnetic precession frequency. The second polarizer can be written as

$$P = \begin{bmatrix} \cos^2\theta & \cos\theta\sin\theta \\ \sin\theta\cos\theta & \sin^2\theta \end{bmatrix}. \tag{2.21}$$

The angle θ is the angle of the second polarizer's polarization axis with respect to the first one.

We can assume that the oscillation amplitude A is small and thus the small angle approximation can be applied to Eq. (2.19). The light intensity after the second polarizer is now given by the matrix product

$$\begin{aligned} I = |PFE|^2 = {} & \frac{A^2}{2}\sin^2\theta(1-\cos 2\omega_{\mathrm{mag}}t) \\ & + A\sin\omega_{\mathrm{mag}}t\cos\theta\sin\theta + \cos^2\theta(1-\frac{A^2}{2}(1-\cos 2\omega_{\mathrm{mag}}t)). \end{aligned} \tag{2.22}$$

In cross-condition with $\theta = 90\,\mathrm{deg}$ this gives

$$I = \frac{A^2}{2}(1-\cos 2\omega_{\mathrm{mag}}t). \tag{2.23}$$

Hence a signal at twice the magnetic precession frequency. A more qualitative explanation for this frequency doubling is that a clockwise and counter clockwise Faraday rotation both give a signal with the same amplitude along the transmission axis of the polarizer. Thus no difference is observed between a component of the magnetization aligned parallel or anti-parallel with the light propagation direction. As a consequence the Faraday signal will be oscillating at double the precession frequency. Away from the cross-condition the projection of the original polarization on the second polarizer's axis makes distinction between the parallel and anti-parallel orientation of the magnetization possible. Actually at $\theta = 45\,\mathrm{deg}$ Eq. (2.22) reduces to

$$I = \frac{1}{2} + \frac{A}{2}\sin\omega_{\mathrm{mag}}t, \tag{2.24}$$

which is a signal at the same frequency as the precession.

The magnon precession ω_{mag}, is typically in the GHz range. Hence if we would like to detect the oscillation as described by Eq. (2.22) electronically, an extremely fast detector would be necessary. Therefore we measure here with a pulsed laser consisting of femtosecond pulses at a repetition rate of 80 MHz. This basically means that every pulse samples Eq. (2.22) and the detector only needs to be able to detect subsequent pulses at the repetition rate, f_{rep} of the laser. Mathematically this can be described by multiplying Eq. (2.22) by a delta pulse train. For simplicity we continue here with the assumption that $\theta = 45\,\text{deg}$ and thus make use of Eq. (2.24):

$$I = (\frac{1}{2} + \frac{A}{2}\sin\omega_{\text{mag}}t)\sum_{k=-\infty}^{\infty}\delta(t - kT_{\text{rep}}), \tag{2.25}$$

where $T_{\text{rep}} = 1/f_{\text{rep}}$ is the period between two pulses.

The Fourier transform of Eq. 2.25 will consist of peaks at the frequencies Nf_{rep} from the constant term and $Nf_{\text{rep}} \pm f_{\text{mag}}$ from the magnetic precession. With N being an integer. As $f_{\text{rep}} << f_{\text{mag}}$, the frequency components from the precession will appear as side lobes of the frequency components at integer multiples of f_{rep}. The frequency f_{sl}, of these side lobes is given by

$$f_{\text{sl}} = Nf_{\text{rep}} \pm \Delta f, \quad \Delta f = f_{\text{mag}} - Zf_{\text{rep}}. \tag{2.26}$$

Here Z is the largest integer for which Δf will be just positive.

The various frequency components as discussed here are shown in Fig. 2.1(b). The Fourier spectrum will repeat itself in a frequency span equal to f_{rep}. For this reason the range in the graphs in this report are all placed within the range $[0\ f_{\text{rep}}]$.

The width of the side lobes is a direct measure for the coherence of the magnetic precession. The narrower the width the more coherent the precession. As we have seen in Eq. (2.23) and (2.24), depending on the relative orientation of the polarizers the observed side lobes will result from an oscillation in the signal at once or twice the precession frequency. It is important to realize what the effect is of the different origin of these side lobes on their width. When the side lobe is related to double the precession frequency its width will be twice as broad as compared to a side lobe related to the real precession frequency.

The measurements shown in this thesis are performed with $45 < \theta < 90\,\text{deg}$. In this configuration the signal related to the real precession frequency is the largest and the correct frequency width is directly obtained. We do not take $\theta = 45\,\text{deg}$ as at this angle the signal to noise ratio is not optimal. The technique as described here is very well suited to determine the coherence of the precession, however due to the use of a pulsed laser with $f_{\text{rep}} << f_{\text{mag}}$ the determination of f_{mag} is not possible.

2.5 FDTD Simulations

In Chapter 2 we want to study the effect of a capping layer between a plasmonic antenna and a magnetic layer on the optical near-field. Furthermore we want to find the optimal antenna geometry which could reduce the switching area in all optical magnetic switching. Therefore we need to solve the Maxwell equations for this geometry. A useful and frequently used numerical tool that is able to do the required calculations is a finite difference time domain (FDTD) simulation [18]. Due to the scalability of the Maxwell equations the FDTD scheme is a universal scheme for problems involving EM radiation of any frequency.

FDTD simulations basically solve the Maxwell equations numerically by discretizing the space and time step. As no theoretical assumptions are made the calculations can give in principle the exact solution if the space and time step go to zero. However the solution will only describe the experiment correctly if the right geometry and dielectric constant of the material is used. In practice this gives the biggest uncertainty to the outcome of the simulations, as especially in nano-structures it will be difficult to let the simulation structure have the exact same shape as the fabricated structure. Furthermore the dielectric constants of the amorphous materials that we are interested in in this thesis are not well known.

Note that the simulations performed here only take the optical properties of the material into account (i.e. the diagonal elements of the permittivity tensor). Hence the magnetic properties are ignored and thus magnetic phenomena like all optical switching will not be visible in the simulations. Yet, combined with the knowledge obtained from experiments we can draw conclusions about the effect of the field distributions that we find, on the process of all optical switching.

The simulations shown in this thesis are performed with the commercial software package Lumerical FDTD Solutions [19]. This software offers the possibility to use non-uniform meshing. This means that the space discretization is not everywhere the same. In specific situations this can reduce the computational time as the required space step is not everywhere the same. For small metallic structures in general a small mesh size is required due to possible large field confinements and small physical dimensions. However for the correct calculation of EM field propagation through air or a substrate much larger mesh cells can already be sufficient. We use a $1 \times 1 \times 1$ nm mesh cell around the smallest metallic structures, while we allow larger mesh cells for the substrate and the air region in the simulations. The allowed time step Δt is determined by a stability criterion which relates Δt to the smallest spatial step Δx by [20]

$$C = \Delta t \sum_{i=1}^{n} \frac{u_{x_i}}{\Delta x_i}. \tag{2.27}$$

Here n is the dimensionality of the simulation (in this case 3) and u_{x_i} is the velocity of the EM wave. For the simulation to be stable $C \leq 1$. In the simulations performed here we take $C = 0.99$.

Furthermore, in most of the simulated structures we can make use of symmetry conditions to reduce the area that needs to be simulated to only one fourth of the total area of interest. This significantly reduces the duration of the simulation. This is even possible when we want to simulate the illumination of the structure of interest by circular polarized light. Orthogonal components of the EM radiation do not influence each other as long as only the diagonal components of the permittivity tensor are taken into account. We can thus perform two independent simulations with orthogonal linear polarization and perform a weighted sum including a phase factor of the EM fields afterwards to obtain the result of illumination with circularly polarized light [21]. Simulating twice one fourth of the area of interest is still faster as compared to performing a single simulation of the whole area of interest.

2.6 Summary

The variety of approaches presented in this chapter is imperative for a comprehensive understanding of magnetization dynamics and the use of light to control it. X-Ray holography supplies a high imaging resolution, while with optical pump-probe experiments it is relatively easy to address the femtosecond timescale. The degree of coherence of a magnetic precession is easier to determine with a technique that measures in the frequency domain. Finally to get inside in the near field beam profile, performing FDTD simulations is a good approach.

References

[1] A. G. Gurevich and G. A. Melkov, *Magnetization Oscillations and Waves* (CRC Press, 1996).

[2] A. K. Zvezdin and V. A. Kotov, *Modern magnetoopticcs and magnetooptical materials* (Institute of Physics Publishing, Bristol and Philadelphia, 1997).

[3] A. Kirilyuk, A. V. Kimel, and Th. Rasing, "Ultrafast optical manipulation of magnetic order," Rev. Mod. Phys. **82**, 2731 (2010).

[4] J. Stöhr, "X-ray magnetic circular dichroism spectroscopy of transition metal thin films," *Future Perspectives for Electron Spectroscopy with Synchrotron Radiation*, Journal of Electron Spectroscopy and Related Phenomena **75**, 253 (1995).

[5] A. R. Khorsand, *Spectroscopic Study of Ultrafast Laser-Induced Magnetization Reversal*, Ph.D. thesis, Radboud University Nijmegen (2013).

[6] M. Faraday, "Experimental researches in electricity," Phil. Trans. Roy. Soc. **136**, 1 (1846).

[7] E. Hecht, *Optics* (Addison Wesley, 2002).

[8] A. R. Khorsand, M. Savoini, A. Kirilyuk, A. V. Kimel, A. Tsukamoto, A. Itoh, and Th. Rasing, "Role of magnetic circular dichroism in all-optical magnetic recording," Phys. Rev. Lett. **108**, 127205 (2012).

[9] R. Medapalli, *Efficient Optical-Control of Ultrafast Magnetization Dynamics in Metallic Alloys*, Ph.D. thesis, Radboud University Nijmegen (2014).

[10] M. Deb, E. Popova, A. Fouchet, and N. Keller, “Magneto-optical Faraday spectroscopy of completely bismuth-substituted $Bi_3Fe_5O_{12}$ garnet thin films,” Journal of Physics D: Applied Physics **45**, 455001 (2012).

[11] P. F. Moulton, “Spectroscopic and laser characteristics of Ti:Al_2O_3,” J. Opt. Soc. Am. B **3**, 125 (1986).

[12] Spectra Physics, *Tsunami; Mode-Locked Ti:sapphire Laser*, Spectra Physics, The Solid State Laser Company, Mountain View, CA, U.S.A. (2005).

[13] Spectra Physics, *Spitfire Pro; Ti:sapphire Regenerative Amplifier Systems*, Spectra Physics, The Solid State Laser Company, Mountain View, CA, U.S.A. (2005).

[14] G. Cerullo and S. De Silvestri, “Ultrafast optical parametric amplifiers,” Review of Scientific Instruments **74**, 1 (2003).

[15] H. C. Stöhr, J. Siegmann, *Magnetism, From Fundamentals to Nanoscale Dynamics* (Springer, 2006).

[16] M. Guizar-Sicairos and J. R. Fienup, “Holography with extended reference by autocorrelation linear differentialoperation,” Opt. Express **15**, 17592 (2007).

[17] D. Zhu, M. Guizar-Sicairos, B. Wu, A. Scherz, Y. Acremann, T. Tyliszczak, P. Fischer, N. Friedenberger, K. Ollefs, M. Farle, J. R. Fienup, and J. Stöhr, “High-resolution X-ray lensless imaging by differential holographic encoding,” Phys. Rev. Lett. **105**, 043901 (2010).

[18] A. Taflove and S. C. Hagness, *Computational Electromagnetics: The Finite-Difference Time-Domain Method* (Artech House, 2005).

[19] *FDTD Solutions v7.0* (Lumerical Solutions Inc., Vancouver (Canada)).

[20] R. Courant, K. Friedrichs, and H. Lewy, “On the partial difference equations of mathematical physics,” IBM Journal of Research and Development **11**, 215 (1967).

[21] Lumerical Solutions Inc., “Circular polarization and phase convention,” (June 2014), http://docs.lumerical.com/en/index.html?ref_sim_obj_planewave_circular_polarization.html.

Chapter 3

Antenna induced nanoscale all optical switching: Simulations and Experiment[1]

Because of its energy efficiency and switching speed, all optical switching of the magnetization could be of interest for data recording. However, in all optical recording techniques in general the bit size is limited by the diffraction limit. By employing plasmonic antennas for subdiffraction focusing of light, we show in this chapter that the bit size in all optical magnetic switching can be brought down to the nanoscale. After an introduction we will discuss in the second section the results from finite difference time domain simulations which leads to the conclusion that an off-resonant antenna is more efficient than a resonant one. Afterwards, in section three we demonstrate experimentally antenna induced all optical switching.

3.1 Introduction

Due to their ability to confine light below the diffraction limit and the accompanying large intensity enhancement [1–5], optical antennas are ideal for increasing the efficiency of light-matter interactions. These properties make optical antennas not only useful for applications in the field of photovoltaics, nonlinear optics, and quantum optics [6], but also in data storage technologies.

In Heat Assisted Magnetic Recording (HAMR), plasmonic structures are used to heat nanoscale spots, such that their magnetization can then be reversed with a smaller magnetic field, increasing the potential data storage density [7, 8]. With HAMR an external magnetic field is still necessary. However, exploiting All Optical

---

[1] In part adapted from: B. Koene, M. Savoini, A. V. Kimel, A. Kirilyuk, and Th. Rasing *Appl. Phys. Lett.* **101**, 013115 (2012).

Switching (AOS) magnetic domains can be switched reversibly with femtosecond laser pulses in the absence of any external magnetic field, making all-optical data storage and retrieval possible [9–11].

Although the AOS process is very fast, the reported sizes of the switched domains are of several microns [10, 11], which is not appealing for industry, where the actual bit size is already well below 100 nm. Yet, the use of plasmonic structures to reduce this size in AOS is not straightforward as the actual recording media are usually protected by a dielectric or metallic capping layer of several tens of nanometers, which will severely affect the focusing abilities and subsequent potential data densities for AOS.

Furthermore, to maintain the polarization of the light in the near field, the plasmonic structure has to be designed very carefully. Although AOS is a heat induced effect, polarization can play a role due to magnetic circular dichroism. Opposite circular polarizations may be absorbed with different efficiencies and thus heat the sample by different amounts. Employing this difference, deterministic helicity dependent switching (HD-AOS) can be obtained [12].

On the experimental side it is not easy to observe AOS mediated by plasmonic antennas. As a switching area of only tens of nanometers is expected, an imaging system with preferably an even smaller resolution is necessary. Optical systems as employed elsewhere in this thesis which use the visible to infrared spectrum cannot reach this resolution as they can not go below the diffraction limit.

In this chapter both simulations and experiment are used to study the applicability of nano antennas in the field of AOS. In section two of this chapter, with finite difference time domain simulations, we will show that an off-resonant plasmonic cross antenna delivers optical energy more efficiently to the magnetic layer as compared to a resonant one. It is shown that the near-field interference between the excitation light and the re-emitted light [13] plays an important role here. We have chosen for a cross antenna as with these antennas the circular polarization state in the near field is maintained and large enhancement factors have been demonstrated in the antenna gap [14, 15].

Evaluating the spot size and field enhancement that can be obtained inside the magnetic film shows that we can obtain a gain in energy together with a sub-diffraction sized spot, even in the presence of a capping layer. Based on this knowledge we have fabricated real antenna structures on top of a magnetic sample. Linear dipole antennas are used to simplify fabrication for these proof of principles experiments. In section three we present antenna induced AOS observed with X-ray holographic imaging.

3.2 FDTD Simulations

In this section we discuss the Finite Difference Time Domain (FDTD) simulations that we performed. First, we describe the studied structure. Second, the simulation results are shown and the role of interference is explained. Last, the spot size that can be obtained in the magnetic layer is shown as well.

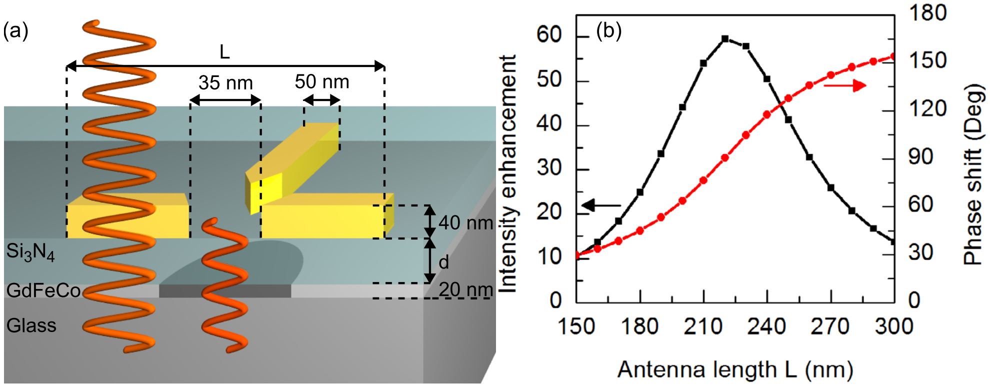

Figure 3.1: Crossed dipole antenna. (a) A sketch of the considered situation. An incoming wave(left) excites the antenna and interferes with the re-emitted wave(right). In the GdFeCo layer this results in a nanoscale reversed magnetic domain(dark cylinder) due to HD-AOS. (b) Intensity enhancement and phase shift as a function of the antenna length. Both are recorded in the center of the antenna gap and in the presence of a 60 nm Si_3N_4 layer.

3.2.1 Structure optimization

The structure we consider is as follows: a glass substrate (dielectric constant [16] $\epsilon = 2.11$) [17], a thin film of magnetic material, in our case 20 nm of GdFeCo ($\epsilon = -1.15 + 28.56i$) [18], protected by a capping layer of Si_3N_4 ($\epsilon = 4$) [17]. The sample is similar to the samples typically used in HD-AOS experiments [10, 11]. In those experiments a capping layer of 60 nm is used to optimize the magneto-optical signal. On top of the last layer we place the cross antenna structure. We use FDTD simulations [19] to calculate the electromagnetic (EM) fields at different positions in the structure presented in Fig. 3.1(a). A circularly polarized plane wave at a wavelength of 800 nm is used to excite the antenna. In the simulations we assume typical dimensions for real cross antennas: a thickness of 40 nm, an arm width of 50 nm, and a gap size of 35 nm[20]. The total length of two opposite arms including the gap is varied from 110 nm to 300 nm. The antenna is made of gold ($\epsilon = -24.11 + 1.49i$) [21]. In the FDTD simulations a non-uniform meshing is used with the smallest mesh cells $1\times1\times1$ nm at the position of the antenna, extending to the GdFeCo film directly underneath the antenna.

In general, when plasmonic antennas are considered, the attention is focused on the intensity enhancement. This intensity enhancement is calculated by normalizing the field intensities obtained in the presence of the antenna structure with the results of a simulation without the antenna. Fig. 3.1(b) shows this intensity enhancement in the antenna gap when the antenna length is varied and a 60 nm thick Si_3N_4 capping layer is used. However, the intensity enhancement as defined earlier does not take into account the difference in energy delivery to the magnetic thin film due to a change in the capping layer thickness, while this capping layer, which is effectively a cavity, will influence the energy delivery. As HD-AOS depends on the polarization of the EM

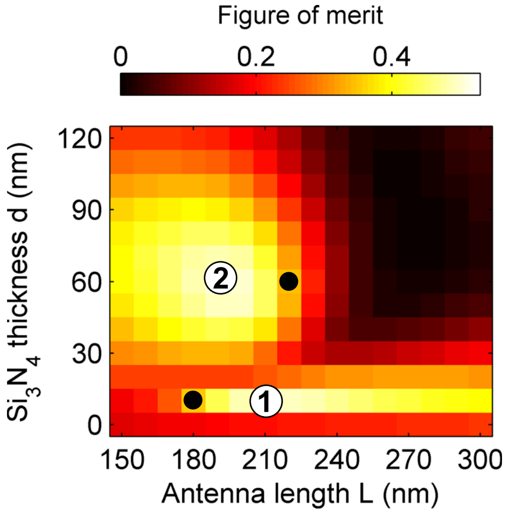

Figure 3.2: FOM as function of the antenna length L and the Si$_3$N$_4$ layer thickness d. The FOM is recorded at half-height of the GdFeCo layer directly below the center of the antenna. Two maxima are observed, indicated by the numbers one and two. The black dots indicate the lengths at which the antenna is resonant for the two optimal Si$_3$N$_4$ thicknesses.

fields we would like to have a measure for the degree of circular polarization as well. For these reasons we will from here on use the following figure of merit (FOM)[14, 15] defined by

$$\mathrm{FOM} = IC^2, \tag{3.1}$$

where I is the intensity and C is the degree of circular polarization given by

$$\mathrm{C} = \frac{2E_x E_y \sin(\delta_x - \delta_y)}{I}. \tag{3.2}$$

Here E_i and δ_i are respectively the amplitude and phase of the field component i. For I we will take the field intensity normalized to the source intensity. Note that the source intensity is equal for all simulations and thus it will take into account the difference in energy delivery due to the capping layer thickness. We would like to emphasize that we do not use the intensity enhancement here, which we can get if we normalize to the intensity profile obtained without antenna in the same plane.

In Fig. 3.2 the FOM inside the GdFeCo is shown as a function of the capping layer thickness and the antenna length. Two maxima can be observed, the first maximum can be found for a dielectric layer thickness of 10 nm and an antenna length of 210 nm. The second maximum is reached for a capping layer thickness of 60 nm and an antenna length of 190 nm. For both capping layer thicknesses this maximum does not coincide with the antenna resonant length as defined in the antenna gap and indicated by the black dots in Fig. 3.2. Note that when the capping layer thickness is changed the antenna resonant length and quality factor can be different as well.

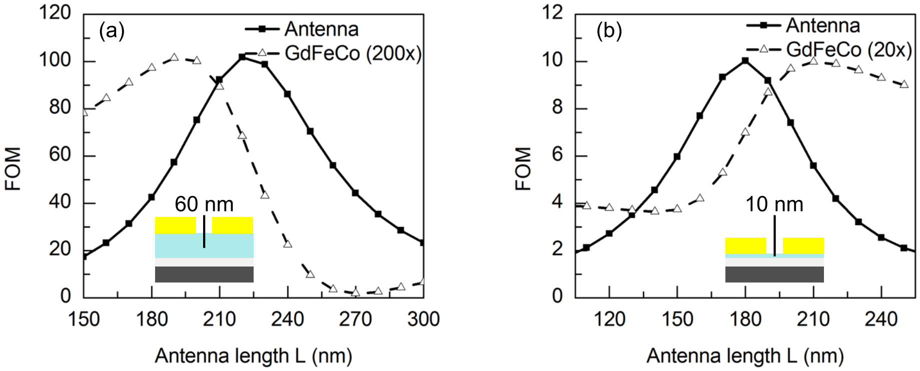

Figure 3.3: FOM in the GdFeCo (open symbols) as function of antenna length. The solid symbols show the FOM in the center of the antenna gap. In (a) a 60 nm Si_3N_4 layer is present while in (b) this layer is 10 nm thick.

Close to the metallic magnetic film the FOM inside the antenna gap will be reduced significantly due to the presence of an extra loss channel formed by the lossy plasmon modes bound to the GdFeCo surface. This directly explains the equal amplitude of the two maxima despite the difference in distance.

3.2.2 Near field Interference

To explain the origin of the discrepancy between the antenna lengths at which the FOM in the GdFeCo reaches a maximum and the antenna resonant length, we will concentrate on the capping layer thicknesses at which these maxima occur. In Fig. 3.3 the FOM inside the GdFeCo (open symbols) is shown together with the FOM in the center of the antenna gap (solid symbols) at a fixed Si_3N_4 thickness of 60 nm(a) and 10 nm(b). These figures show a clear difference between the behavior of the FOM with antenna length in the plane of the antenna and inside the GdFeCo. The maximum intensity in the GdFeCo layer occurs for 10 nm (60 nm) of Si_3N_4 for an antenna longer (shorter) than the resonant length.

The observed behavior can be explained by interference between the re-emitted light from the antenna and the excitation light. Like a harmonic oscillator, a resonance in intensity goes together with a phase shift for the re-emitted light. The phase shift in the center of the antenna gap as function of the antenna length is shown in Fig. 3.1(b) for the 60 nm thick capping layer. In the center of the antenna gap no interference can be observed due to the large difference in intensity of the two light sources. From Fig. 3.1(b) it can be seen that the light in the antenna gap is 60 times more intense than the exciting light. However, the exponential decay of the plasmon fields causes this large difference in intensity to disappear fast with distance. This results in comparable intensities for the two light beams in the GdFeCo layer, 60 nm below the antenna, leading to interference effects. The increase in intensity towards the plasmon resonance combined with the relative small phase difference for antennas shorter than the resonant length makes the maximum intensity in the active layer to occur for an antenna that is a few tens of nanometers shorter than a resonant antenna. For antennas longer than resonant ones, the large phase shift for the re-emitted light results in destructive interference, which explains the minimum in Fig. 3.3(a) for an antenna length of 270 nm.

If we now compare the above situation with the case of only a 10 nm capping layer, Fig. 3.3(b), than we can observe a few differences. First, in Fig. 3.3(b) there is no complete destructive interference visible. This could indicate that the two EM waves that interfere do not have the same amplitude. The other difference is that while in the 60 nm case we have a maximum for an antenna that is shorter than the resonant one, for the 10 nm case we have in the same situation a minimum. We ascribe this effective phase shift of roughly π for one of the two waves to the interplay between the plasmon modes of the antenna and the GdFeCo film.

3.2.3 Magnetic layer field patterns

All previous simulation results were collected in a single point only. However, for the purpose of magnetic switching it is of interest to know the field patterns resulting from the interference in the plane of the magnetic thin film. These interference patterns give an indication about the size of the magnetic domain that is switched by using the optical antennas as considered in this paper. The obtained interference patterns for the 60 nm thick capping layer are shown in Fig. 3.4(a) for antenna lengths of respectively 190 nm (maximum), 220 nm (resonant) and 270 nm (minimum). In the left column the FOM distribution in the vertical direction is shown while in the right column the in plane distribution is shown. The left column clearly shows the fast decrease of the FOM when we move further away from the antenna. As is clearly shown in Fig. 3.4(c), for the antenna with a length of 190 nm a spot size with a full width at half maximum (FWHM) of 190 nm is found. Note that we have a constant FOM over a width of 90 nm. If we calculate the maximum intensity enhancement in the GdFeCo for this antenna we find a value of 2.6.

Fig. 3.4(b) shows the same information as Fig. 3.4(a) but now for a 10 nm capping layer. With this thickness the FOM decays even faster while moving away from the antenna and an even smaller spot size with a FWHM of 41 nm is found. This sub diffraction area is substantially smaller than the spot size of a light beam focused with conventional objectives (typical dimensions with an immersion oil objective are of approximately 350 nm using 800 nm light). We would like to mention that considering only the field intensity I would give a spot size FWHM of 52 nm. Hence we have here an advantage due to the dependence of the AOS on the helicity of light. The maximum field enhancement in the 41 nm spot is 3.7. This would mean that the known switching threshold of 2.6 mJ/cm^2 for a GdFeCo sample without any structure on top [12], will reduce to 0.7 mJ/cm^2 in the case that nanoantennas are used.

Although low, the intensity enhancement we find is in the same order of magnitude of others reported for devices aimed for similar applications (as for example reported in Fig. 2(b) of Ref. [7]). In our case the low value is caused by the quickly vanishing nature of the near fields together with the presence of a capping layer while for

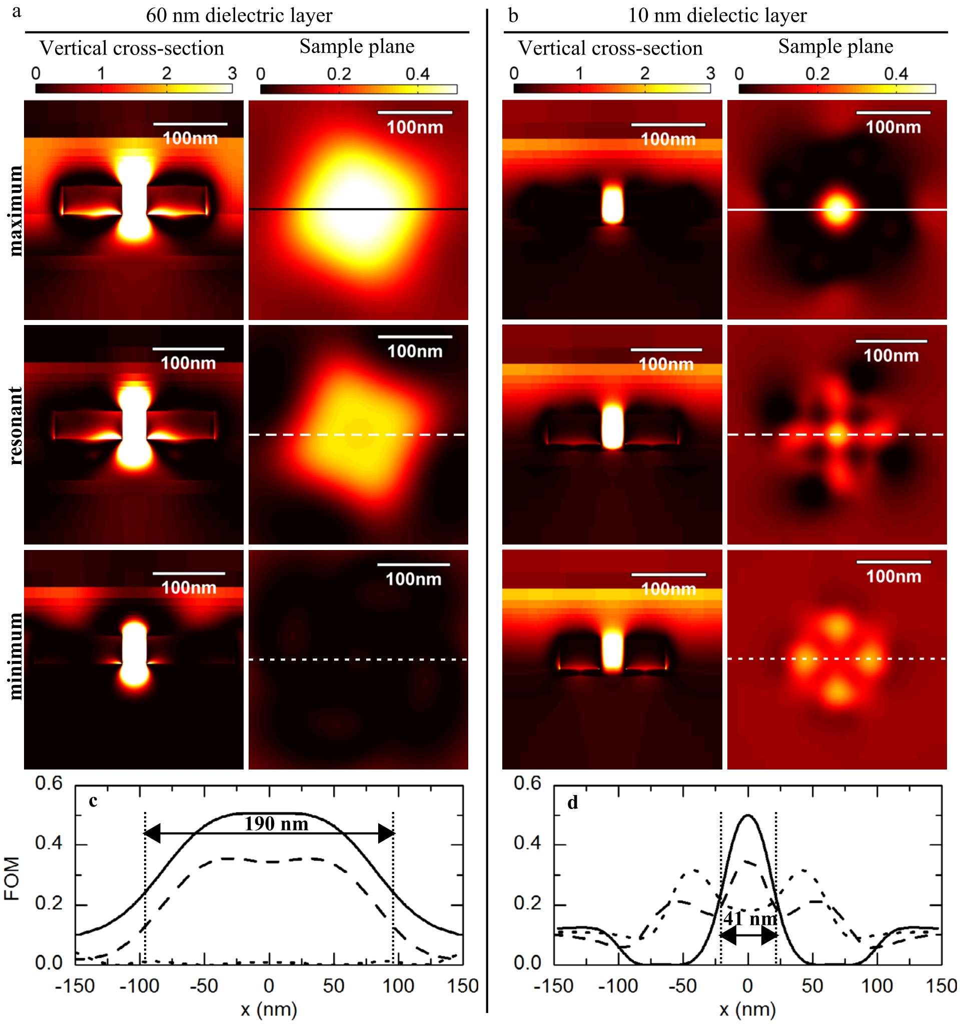

Figure 3.4: FOM distribution in the vertical (left column) and horizontal (GdFeCo plane, right column) cross-section. In (a)/(b) the dielectric layer is 60/10 nm thick. For both layer thicknesses three different antenna lengths are shown. The antennas shown are the ones with a length that gives a maximum and minimum for the FOM inside the GdFeCo as found in Fig. 3.3, as well as for the resonant antenna. Line plots of the FOM profiles along the dashed and solid lines in (a) and (b) are shown in (c) and (d) for the two layer thicknesses. The FWHM of the central spot is indicated for the profiles that demonstrate the highest FOM.

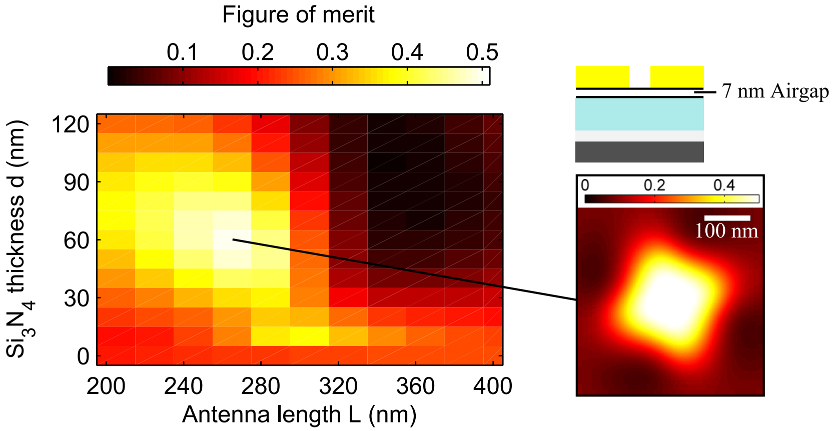

Figure 3.5: FOM as function of the antenna length L and the Si_3N_4 layer thickness d in the case that a 7 nm air gap is present between the antenna and the dielectric layer. The FOM is recorded at half-height of the GdFeCo layer directly below the center of the antenna. For the highest FOM the in-plane field profile is shown as well.

example in Ref. [7] there is a less efficient coupling due to the high refractive index surrounding the antenna. For the purpose of HD-AOS this small enhancement factor is not a problem as the main reason to use optical antennas here is to bring switching down to the nanoscale.

To summarize, here we considered a plasmonic structure that can be easily made with the current state of the art nanofabrication technologies [20]. With progress in the fabrication process smaller antenna gaps will also be attainable. This would make it possible to have smaller spot sizes and larger enhancement factors. Considering data storage technology, in which a writing head (antenna) moves over the medium, we performed some simulations with a 7 nm air slit between the antenna and the capping layer as well. Except in the antenna length no noticeable changes where observed. The obtained FOM versus antenna length and dielectric layer thickness can be found in Fig. 3.5. The in-plane field profile of the antenna with the highest FOM is shown in this figure as well.

3.3 Experimental realization[2]

In this section we use X-ray holographic imaging to show that plasmonic antennas can be employed to switch the magnetization on the nanoscale. The measurements are performed at the Stanford Synchrotron Radiation Light source (SSRL) of the SLAC

---

[2] The collaboration in which this work is realized consisted of B. Koene, M. Savoini, A. Kimel, A. Kirilyuk and Th. Rasing from the Radboud University Nijmegen, J. Stöhr and the H. Dürr group from the Stanford University, X. Wu and B. Hecht from the University of Wurzburg, A. Tsukamoto and A. Itoh from the Nihon University Chiba.

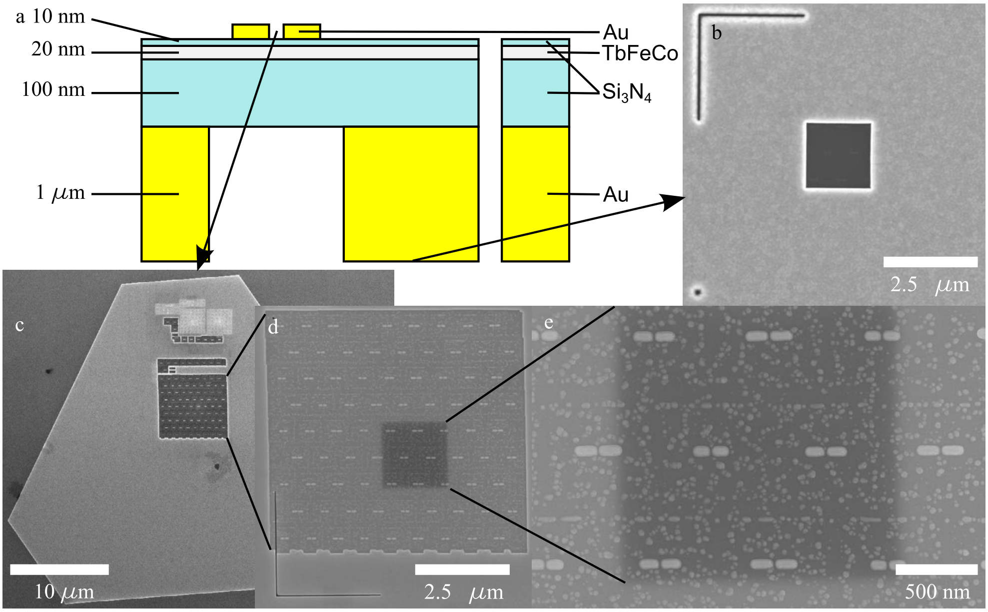

Figure 3.6: An overview of the fabricated sample. (a) A schematic of the sample that clearly shows the layer structure. (b) A scanning electron microscopy (SEM) image of the back side of the sample with the L and dot shaped reference holes and the imaging window. (c) to (e) are SEM images of the top side of the sample (c) A gold flake with antenna structures. (d) a zoom in on the area with antennas, the background contrast shows clearly where the 2 by 2 μm imaging window is located. The L shaped reference hole is visible as well. (e) A zoom in on the aperture area.

national accelerator laboratory. First the technique of X-Ray Holographic imaging is briefly explained and the fabrication steps are shown, followed by the results and a discussion.

3.3.1 Experimental setup and sample preparation

As explained in Sect. 2.4.1 the technique of X-Ray holographic imaging is used. This technique is based on magnetic circular dichroism. To obtain a high resolution the specific form of holography called "holography with extended reference by autocorrelation linear differential operation" (HERALDO) is used. In HERALDO the resolution is determined from the sharpness of the edge of the reference structure instead of its size. With this method a resolution down to 16 nm is obtained [22].

The measurement is performed in transmission geometry using a 100 nm thick Si_3N_4 membrane as the sample substrate. This membrane is thin enough to allow X-rays to be transmitted. On top of this membrane a 20 nm TbFeCo layer is sputtered followed by a second layer of Si_3N_4 with a thickness of 10 nm. Compared to GdFeCo which was used in the first part of this chapter, TbFeCo has a larger anisotropy, hence

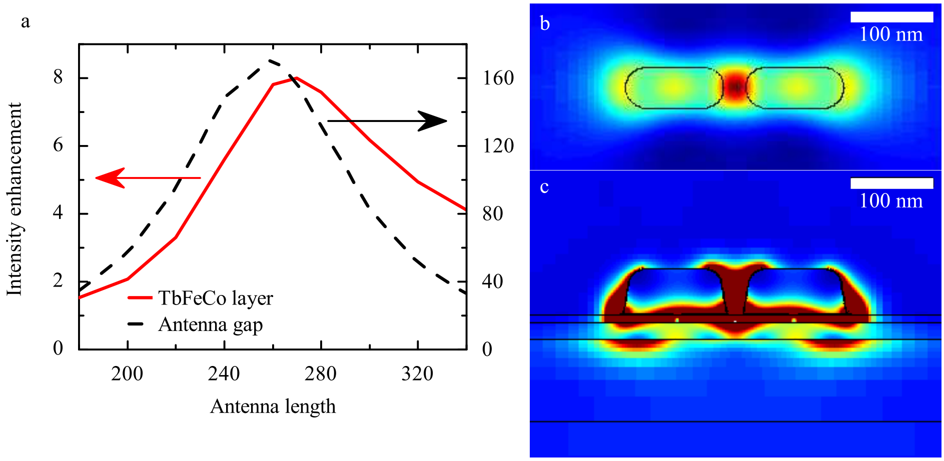

Figure 3.7: Intensity enhancement for a simple dipole antenna on top of a Si_3N_4 membrane. (a) shows the enhancement versus antenna length inside the antenna gap and at half height inside the TbFeCo layer. In (b) and (c) the field distribution is shown for a 270 nm antenna at half height inside the TbFeCo layer and in the vertical direction through all layers respectively.

it should be able to maintain smaller stable magnetic domains. For the holographic imaging a reference hole and imaging window is necessary. For this reason the back side of the membrane is covered by a one micron thick layer of gold which is non-transparent for the X-rays. With focused ion beam (FIB) the reference hole and an imaging window of 2 by 2 μm are created in the gold layer. A schematic of the sample structure is shown in Fig. 3.6(a).

As we use TbFeCo instead of GdFeCo and the substrate is only 100 nm thick, new simulations have to be performed to determine the optimal antenna length. Furthermore instead of using a cross-antenna we will use a dipole antenna as this simplifies the fabrication process and AOS can also be obtained with linearly polarized light. From the results of the simulations, shown in Fig. 3.7(a) we find an optimal antenna length of 270 nm. The obtained line shape is comparable to the one obtained in Fig 3.3(b) although the difference with the line shape in the antenna gap is smaller. The field distribution of the 270 nm antenna is shown in Fig. 3.7(b) and (c). To take into account differences between simulations and real structures, we fabricated antennas with total lengths of 230, 270 and 310 nm.

The antennas are fabricated with FIB on gold flakes grown on a glass substrate [23]. After the fabrication the gold flakes are transferred onto the membrane [24]. The imaging window is created in a processing step after the antennas have been placed onto the sample. For this reason, more antennas are fabricated then can fit in the window. This ensures that several antennas will be inside the window. Scanning electron beam microscopy images of the antennas and the reference hole and imaging window are shown in Fig. 3.6(b)-(e).

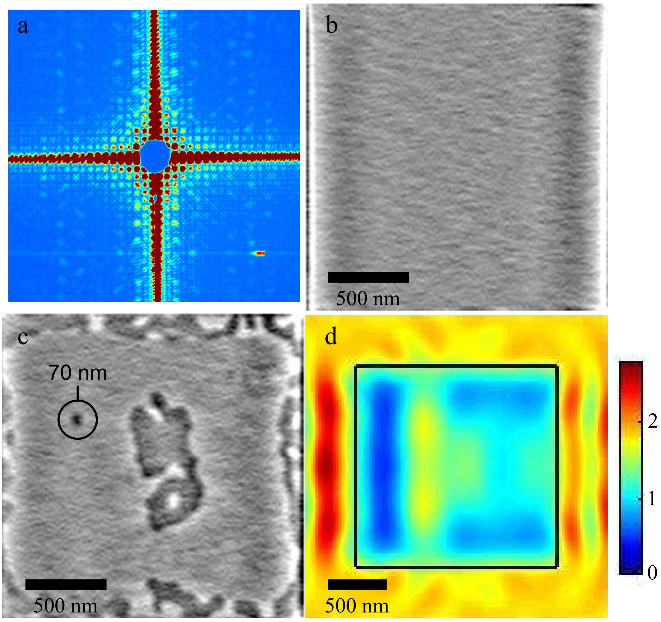

Figure 3.8: All optical switching inside the aperture without antennas. (a) A typical scattering pattern collected by a CCD camera behind the sample. (b) An X-ray holography image of the optically unexposed aperture area. The homogeneous magnetic signal is a result of the initial saturation of the sample by a magnetic field of 1.6 T (c) An X-ray holography image of the optically exposed aperture area. Already without antennas an optically switched area of 70 nm can be observed as indicated with the black circle. (d) FDTD simulations of the field distribution inside the TbFeCo layer. The black lines indicate the position of the aperture.

3.3.2 Results and discussion

Although we use X-rays to image (probe) the recorded magnetic pattern, for the creation of this pattern with AOS we use a 1030 nm laser (pump). We would like to emphasize here that to induce small switched areas with plasmonic antenna's the light does not have to be focused. Hence, in the experiments shown here the pump spot is kept bigger than the imaging window. The pump light is aligned at 30 deg from the sample normal. Due to this angle the focal spot is slightly elliptical. Furthermore the sample is oriented such that the antennas are illuminated with p polarization, that is the polarization is along the antenna length and parallel to the sample surface.

The first experiment we did was with an imaging window without antennas to determine the fluence at which AOS occurs. All samples shown here where initially brought into a homogeneous magnetic state by applying a 1.6 T magnetic field. In Fig. 3.8(a) a typical scattering pattern that is recorded is shown. An image of the empty imaging window before and after illumination of the sample with the pump, as obtained by a Fourier transform of a scattering pattern, is shown in Fig. 3.8(b) and (c) respectively. The pump fluence was approximately 9 mJ/cm^2. Clear indications of switching are visible. Especially at the border and in the center of the imaging window, switched area's can be identified.

The color scaling in Fig. 3.8(c) requires some more explanation. There can be made a distinction between four main tints, white, light grey, dark grey and black. While light grey and dark grey represent oppositely directed out of plane magnetizations, the black and white color occur only at domain boundaries. We assign the white and black colors to the same magnetization direction as respectively the light grey and dark grey colors. The reason for the different amplitude we ascribe to the HERALDO measurement method. This method is based on a cross-correlation between the object of interest and the reference structure. An ideal reference structure would be a point (delta function). In that case in the frequency space the spatial frequencies of the object would be weighted equally, however, deviations from this ideal reference structure will result in a finite frequency window where the high frequencies and thus sharp changes in real space are weighted stronger as compared to the low frequencies. This results in the higher amplitudes at the domain boundaries.

To explain the observed switching pattern we performed FDTD simulations of the experimental geometry. The obtained intensity profile at half height inside the TbFeCo layer is shown in Fig. 3.8(d). It is clear that the area where we observe switching roughly follows the light intensity pattern. A physical explanation for the higher intensity in the region outside the imaging window is simply that the light is reflected by the gold layer and thus passes twice through the TbFeCo layer. The region of higher intensity in the center of the window can be due to interference of light reflecting from the gold edges of the imaging window. It is worth noticing that the black dot (optically switched area) indicated by the black circle in Fig. 3.8(c) has a diameter of 70 nm.

In Fig. 3.9 the results for two antenna samples are shown. The charge image in Fig. 3.9(a) confirms that we have a resolution that is able to distinguish the antenna gap which is approximately 25 nm. In Fig. 3.9(b) the magnetic image is shown. However to clearly see where the magnetization switches with respect to the antenna we use the charge image to draw the antenna outline in the magnetic image, as is done in Fig. 3.9(c) and (d).

The two samples shown here is a small selection of several measurements performed at different fluencies and samples, nevertheless they show the general features that we observe more often. Again there is switching at the window boundaries. More interestingly, there is switching in the areas around the antennas as well. In contrast, away from the antennas no clear switching is observed. The antennas thus clearly modify the switching pattern. It should be noted however, that in general the switching does not occur in the center of the antennas as we expected. From the two samples shown only one area can be identified where clear switching occurs in the antenna gap. This is for the antenna in the bottom left corner of sample 2. It is worth noting that for this switching spot the width in the direction perpendicular to the antenna axis is not extending outside the antenna contour. Hence the width of the spot is smaller than the antenna width which is around 50 nm. More often

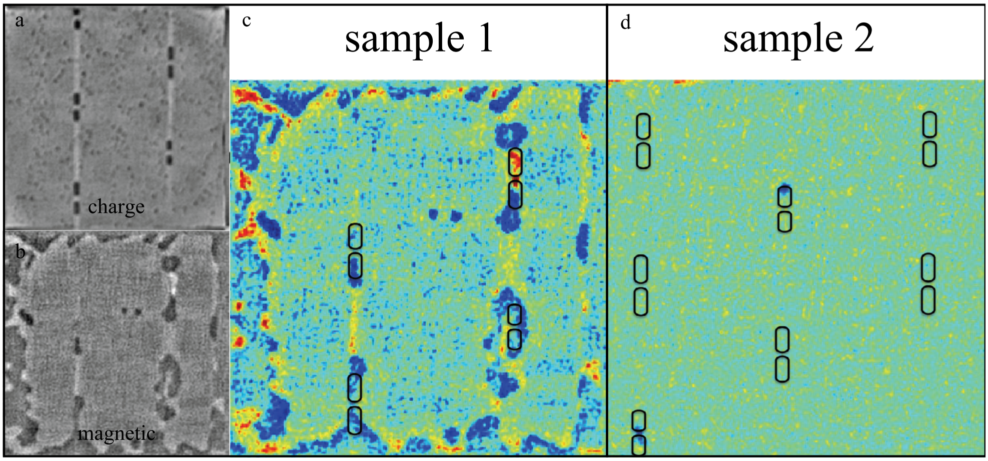

Figure 3.9: All optical switching using plasmonic antennas. (a) and (b) show the charge and magnetic signals that can be obtained from the X-ray holography for a sample with antennas. In the charge image the antennas are clearly visible. In (c) and (d) the charge image is used to draw the antenna outline on the magnetic image for two different samples. Switching can be observed close to the antennas. The pump fluencies used for sample 1 and 2 are respectively 9.4 mJ/cm^2 and 3.7 mJ/cm^2

however, we observed switching beneath one of the antenna arms, like is the case for the top left antenna in sample 1 and the top middle antenna of sample 2.

We can think of several reasons why the switching does not occur only in the center. Besides fabrication imperfections, surface roughness, or non-perfect transfer [24] of the antennas between the glass and membrane substrate we could for example also look at the field profile in Fig. 3.7(b). Note for example that although a clear spot can be identified in the antenna gap, the contrast with the field profile under the antenna arms is much smaller than the contrast in the direction perpendicular to the antenna axis. This means that to obtain a spot only in the gap region the fluence should be tuned very accurately. In Fig. 3.9(c) where a lower fluence is used already a more isolated switching area can be observed. Notice also the small gold particles in Fig. 3.6(e) around the antenna which are formed during the transferring of the antennas from the glass to the membrane. These particles might modify the antenna modes as well.

Yet, the above explanation does not explain the observation of switching underneath a single antenna arm only. One explanation for this might be given by recent measurements that demonstrate a large inhomogeneity of the spatial distribution of the Gd and Fe content in GdFeCo [25]. Such an inhomogeneity causes differences in the local switching properties. Although here we use TbFeCo, the fabrication method does not differ a lot and a similar inhomogeneity in this material is observed [26].

3.4 Conclusions

To conclude, we have shown that besides the direct field enhancement and field confinement related to plasmonic structures, near-field interference effects can be of similar importance when optimizing the energy delivery to the near field. As a relevant example we considered a metallic magnetic thin film protected by a dielectric capping layer with cross-antennas on top. The antenna length at which the maximum energy is delivered to the thin film differs from the resonant antenna length. This difference can be attributed to the interference between the excitation light and the re-emitted light by the antenna. With the antennas on top of a 10 nm thick capping layer and using 800 nm light, we were able to predict a sub diffraction spot with a maximum intensity enhancement of 3.7 and a FWHM of 41 nm inside the magnetic material, which is comparable to the bit size in present day storage technology.

Furthermore using X-ray holographic imaging we have shown that plasmonic antennas indeed can modify the switching area. We observe switched areas with a width of below 50 nm. It should be noted however that not in all cases switching in the center area is obtained as expected. Further development is necessary to achieve a robust and reproducible switching of a small domain at the antenna's center.

References

[1] A. A. Mikhailovsky, M. A. Petruska, M. I. Stockman, and V. I. Klimov, "Broadband near-field interference spectroscopy of metal nanoparticles using a femtosecond white-light continuum," Opt. Lett. **28**, 1686 (2003).

[2] A. A. Mikhailovsky, M. A. Petruska, K. Li, M. I. Stockman, and V. I. Klimov, "Phase-sensitive spectroscopy of surface plasmons in individual metal nanostructures," Phys. Rev. B **69**, 085401 (2004).

[3] M. Celebrano, M. Savoini, P. Biagioni, M. Zavelani-Rossi, P.-M. Adam, L. Duò, G. Cerullo, and M. Finazzi, "Retrieving the complex polarizability of single plasmonic nanoresonators," Phys. Rev. B **80**, 153407 (2009).

[4] L. Novotny and N. van Hulst, "Antennas for light," Nat Photon **5**, 83 (2011).

[5] P. Biagioni, J.-S. Huang, and B. Hecht, "Nanoantennas for visible and infrared radiation," Reports on Progress in Physics **75**, 024402 (2012).

[6] P. Bharadwaj, B. Deutsch, and L. Novotny, "Optical antennas," Adv. Opt. Photon. **1**, 438 (2009).

[7] W. A. Challener, C. Peng, A. V. Itagi, D. Karns, W. Peng, Y. Peng, X. Yang, X. Zhu, N. J. Gokemeijer, Y.-T. Hsia, G. Ju, R. E. Rottmayer, M. A. Seigler, and E. C. Gage, "Heat-assisted magnetic recording by a near-field transducer with efficient optical energy transfer," Nat Photon **3**, 220 (2009).

[8] B. C. Stipe, T. C. Strand, C. C. Poon, H. Balamane, T. D. Boone, J. A. Katine, J.-L. Li, V. Rawat, H. Nemoto, A. Hirotsune, O. Hellwig, R. Ruiz, E. Dobisz, D. S. Kercher, N. Robertson, T. R. Albrecht, and B. D. Terris, "Magnetic recording at 1.5 Pb m^{-2} using an integrated plasmonic antenna," Nat. Photonics **4**, 484 (2010).

[9] A. V. Kimel, A. Kirilyuk, P. A. Usachev, R. V. Pisarev, A. M. Balbashov, and Th. Rasing, "Ultrafast non-thermal control of magnetization by instantaneous photomagnetic pulses," Nature **435**, 655 (2005).

[10] C. D. Stanciu, F. Hansteen, A. V. Kimel, A. Kirilyuk, A. Tsukamoto, A. Itoh, and Th. Rasing, "All-optical magnetic recording with circularly polarized light," Phys. Rev. Lett. **99**, 047601 (2007).

[11] K. Vahaplar, A. M. Kalashnikova, A. V. Kimel, D. Hinzke, U. Nowak, R. Chantrell, A. Tsukamoto, A. Itoh, A. Kirilyuk, and Th. Rasing, "Ultrafast path for optical magnetization reversal via a strongly nonequilibrium state," Phys. Rev. Lett. **103**, 117201 (2009).

[12] A. R. Khorsand, M. Savoini, A. Kirilyuk, A. V. Kimel, A. Tsukamoto, A. Itoh, and Th. Rasing, "Role of magnetic circular dichroism in all-optical magnetic recording," Phys. Rev. Lett. **108**, 127205 (2012).

[13] E. S. Barnard, R. A. Pala, and M. L. Brongersma, "Photocurrent mapping of near-field optical antenna resonances," Nat. Nano. **6**, 588 (2011).

[14] P. Biagioni, J. S. Huang, L. Duò, M. Finazzi, and B. Hecht, "Cross resonant optical antenna," Phys. Rev. Lett. **102**, 256801 (2009).

[15] P. Biagioni, M. Savoini, J.-S. Huang, L. Duò, M. Finazzi, and B. Hecht, "Near-field polarization shaping by a near-resonant plasmonic cross antenna," Phys. Rev. B **80**, 153409 (2009).

[16] The mentioned dielectric constants are all fits to the experimentally measured data in the given references.

[17] E. D. Palik, *Handbook of Optical Constants of Solids I - III* (Academic Press, 1997).

[18] W. R. Hendren, R. Atkinson, R. J. Pollard, I. W. Salter, C. D. Wright, W. W. Clegg, and D. F. L. Jenkins, "Optical and magneto-optical characterization of TbFeCo and GdFeCo thin films for high-density recording," Journal of Physics: Condensed Matter **15**, 1461 (2003).

[19] *FDTD Solutions v7.0* (Lumerical Solutions Inc., Vancouver (Canada)).

[20] P. Biagioni, X. Wu, M. Savoini, J. Ziegler, J.-S. Huang, L. Duò, M. Finazzi, and B. Hecht, "Tailoring the interaction between matter and polarized light with plasmonic optical antennas," Proc. SPIE **7922**, 79220C (2011).

[21] P. B. Johnson and R. W. Christy, “Optical constants of the noble metals,” Phys. Rev. B **6**, 4370 (1972).

[22] D. Zhu, M. Guizar-Sicairos, B. Wu, A. Scherz, Y. Acremann, T. Tyliszczak, P. Fischer, N. Friedenberger, K. Ollefs, M. Farle, J. R. Fienup, and J. Stöhr, “High-resolution X-ray lensless imaging by differential holographic encoding,” Phys. Rev. Lett. **105**, 043901 (2010).

[23] J.-S. Huang, V. Callegari, P. Geisler, C. Brüning, J. Kern, J. C. Prangsma, X. Wu, T. Feichtner, J. Ziegler, P. Weinmann, M. Kamp, A. Forchel, P. Biagioni, U. Sennhauser, and B. Hecht, “Atomically flat single-crystalline gold nanostructures for plasmonic nanocircuitry,” Nat Commun **1**, 150 (2010).

[24] X. Wu and B. Hecht, To be submitted.

[25] C. E. Graves, A. H. Reid, T. Wang, B. Wu, S. de Jong, K. Vahaplar, I. Radu, D. P. Bernstein, M. Messerschmidt, L. Müller, R. Coffee, M. Bionta, S. W. Epp, R. Hartmann, N. Kimmel, G. Hauser, A. Hartmann, P. Holl, H. Gorke, J. H. Mentink, A. Tsukamoto, A. Fognini, J. J. Turner, W. F. Schlotter, D. Rolles, H. Soltau, L. Strüder, Y. Acremann, A. V. Kimel, A. Kirilyuk, Th. Rasing, J. Stöhr, A. O. Scherz, and H. A. Dürr, “Nanoscale spin reversal by non-local angular momentum transfer following ultrafast laser excitation in ferrimagnetic GdFeCo,” Nat Mater **12**, 293 (2013).

[26] M. Savoini and T. Wang, “EELS measurements and analysis,” Private communications.

Chapter 4

Magnetization dynamics in Bismuth Iron Garnet[1]

Bismuth-iron garnet is an interesting material for magneto-optical studies as it shows very large Faraday rotation. In this chapter we present a detailed study of the magnetization dynamics that can be excited in this material with a femtosecond laser pulse. We demonstrate that a new excitation mechanism can be found in this garnet. First an introduction is given followed by a brief description of the sample and the setup. Then it is shown how the dynamics depend on the pump polarization and fluence. In Sect. 4.4 the field dependence is shown and in Sect. 4.5 the characteristics of the new excitation mechanism are discussed. The last section gives a conclusion.

4.1 Introduction

Controlling the magnetization dynamics with femtosecond laser pulses is an actively developing area of research [1]. Among various mechanisms responsible for the excitation of such dynamics, the non-thermal ones are the most interesting [2–7]. Using non-thermal excitation one is able to introduce changes in the magnetic system at much shorter time scales, which are defined by the spin-orbit coupling and not by thermalization processes. The difference is particularly significant in dielectrics, where the interaction of spins with the environment is limited by the so-called phonon-magnon bottleneck [1].

Two main non-thermal mechanisms were shown to exist. The first of them is characterized by an impulsive action, that only exists during the laser pulse. Inverse Faraday [2] and Cotton-Mouton [5, 8] effects are representative of this type. The second ones are displacive effects such as the photoinduced change of magnetic

---

[1] This work is realized in collaboration with M. Deb, E. Popova and N. Keller from the Université de Versailles Saint-Quentin-en-Yvelines

anisotropy [4, 9], which persist in the sample for a time interval much longer than the length of the pulse. It has also been shown, that the combination of the two effects can in principle be used for ultrafast switching of the magnetization at the time scale of the laser pulse [3]. Therefore, detailed understanding of the exact behavior of non-thermal excitation mechanisms is very important for further development of the ultrafast optical manipulation of magnetic moments.

In this chapter, three different excitation mechanisms are distinguished. In addition to the impulsive inverse Faraday effect [2–4] and the displacive action of the photoinduced magnetic anisotropy [3, 4, 9], another previously unknown excitation mechanism is identified. The possible origin of this mechanism is suggested to be a short living photo-induced change in the anisotropy. This new mechanism is linearly dependent on the light intensity but does not depend on polarization.

Here, we will first discuss the results of a detailed study on the dependence of the induced magnetization dynamics on the pump pulse polarization and fluence, and on the external field. In particular we will address the anisotropy and Gilbert damping. The oscillation amplitude dependence on the external field will be the main indicator for the new excitation mechanism.

4.2 Sample and experimental setup

The investigations have been performed using bismuth iron garnet ($Bi_3Fe_5O_{12}$, BIG). The interest in this material is caused by its largest known magneto-optical constants in the iron garnet family, with the Faraday rotation reaching 60 deg/μm in the visible light range ($\lambda = 430$ nm). This property makes BIG a promising material for the fabrication, for example, of magneto-optical circulators [10]. The synthesis of this material requires non-equilibrium growth techniques and, so far, the fabrication of a bulk crystal of BIG was not successful. However, since the '90s [11], good quality thin films of BIG are grown on structure-matching substrates.

The studied sample is a 200 nm thick single crystalline and single phase BIG film grown epitaxially on a substituted $Gd_3Ga_5O_{12}(001)$ substrate by pulsed laser deposition. The sample has uniaxial and cubic anisotropy which are of the order of 300 and 200 Oe respectively. The measured saturation magnetization, $4\pi M_\mathrm{s}$ of BIG films is about 1500 Oe [12]. A more detailed description of the growth conditions and the investigation of the structural, magnetic and static magneto-optic properties of BIG films can be found in Refs. [12–15].

For the measurements an optical pump-probe setup in transmission geometry is used. The pump was the direct output of a Spectra Physics Spitfire amplified laser system giving 40 fs, 800 nm pulses at a repetition rate of 1 kHz. At this wavelength BIG is mostly transparent so heating effects are minimal. For the probe, part of the laser output was directed through an optical parametric amplifier (OPA) to change the wavelength to 450 nm.

The pump pulse was aligned perpendicularly to the sample while the probe was at a small angle from the sample normal ($\sim$10 deg). The pump induced Faraday rotation of the probe was measured using a balanced detector scheme in combination

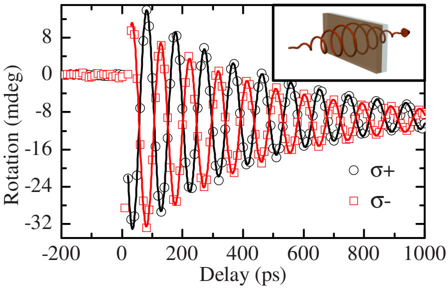

Figure 4.1: Observed magnetization dynamics for circular pump polarizations. A 180 deg phase difference is visible between oscillations excited with right ($\sigma+$, black circles) and left ($\sigma-$, red squares) circular polarization. The solid lines are fits using Eq. (4.1). The external field is 3 kG and the pump fluence is 27 mJ/cm^2.

with a lock-in amplifier and a chopper. An in plane external field was applied by an electromagnet.

The probe polarization is in all cases linear while the polarization of the pump is varied between linear and circular. The spot size of the pump was, depending on the measurement, 130 or 365 μm, while the probe spot was 26 μm. The fluence of the pump was varied between 10 and 50 mJ/cm^2. The pulse energy of the probe was at least 1000× smaller than that of the pump.

All experimental data of the pump induced oscillations in the Faraday rotation are fitted with an exponentially decaying sine function

$$y = y_0 + (B\mathrm{e}^{R_0 t}) + A\mathrm{e}^{-t/\tau}\sin(2\pi f t - \phi). \tag{4.1}$$

Here y_0 is a dc offset, A is the amplitude of the oscillations, f is the frequency, τ is the oscillation lifetime, ϕ is the initial phase and t is the time. The exponential second term is only used when it improved the fit. The origin of this exponential term is difficult to assign. It can appear due to state-filling effects that become visible in the magneto-optical response. The exponential behavior is most visible in the case of large pump fluences.

4.3 Polarization and fluence dependence of the magnetization dynamics

The oscillations that are observed when we excite the sample with circularly polarized pump pulses are shown in Fig. 4.1. From this figure it is clear that when the helicity of the pump light is reversed from right ($\sigma+$) to left ($\sigma-$), the initial phase changes by 180 deg. This behaviour is similar to what is observed earlier [3] and can be explained by the inverse Faraday effect.

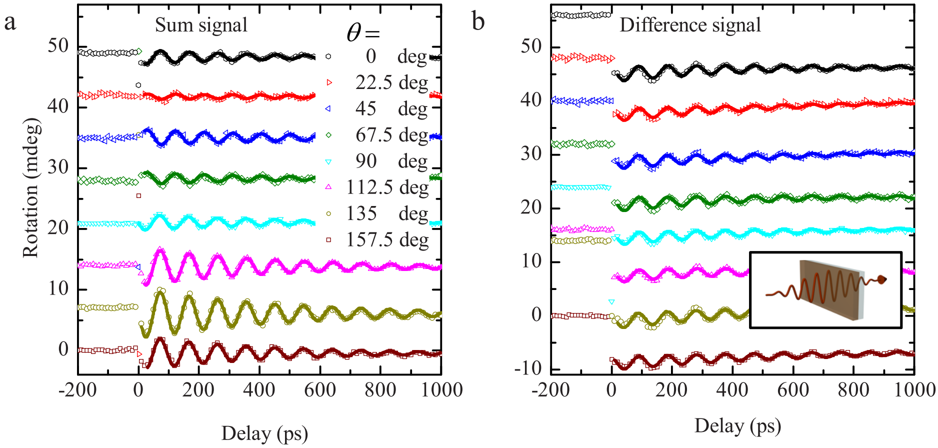

Figure 4.2: Observed magnetization dynamics for linear pump polarizations with different polarization angles θ as indicated in the legend. The sum(a)/difference(b) signal is obtained by taking the sum/difference of the positive and negative field data. The solid lines are fits using Eq. (4.1). The external field and fluence are the same as in Fig. 4.1.

The oscillations obtained with linearly polarized light with different polarization angles θ, are shown in Fig. 4.2. In this figure we have plotted separately the sum and difference of the data obtained at opposite directions of the applied magnetic field. The field was in all cases sufficient to saturate the magnetization. Representing the data in this manner shows that we can distinguish two differently behaving oscillations. The sum/difference signal in Fig. 4.2(a)/(b) shows an oscillation that is independent/dependent on the direction of the magnetic field.

Besides their different dependence on the direction of the field, the sum and difference signal differ in their initial phase and in their amplitude dependence on the angle of polarization θ, as well. In Fig. 4.3(a) the initial phase obtained from fits to the data shows a difference of almost $\pi/2$. To formulate differently, while the sum signal is sine like, the difference signal is cosine like. For comparison the initial phase for the left and right circular polarizations are shown in the same graph as well. From their initial phase it follows that the oscillations induced by the two circular polarization are both sine like.

Fig. 4.3(b) shows how the amplitude of the two signals depends on θ. While the sum signal shows a periodic, $\sin 2\theta$, modulation of the amplitude and even changes sign, the amplitude of the difference signal does not change.

The behaviour of the sum signal is similar to what is observed in Ref. [3] and can be ascribed to the photoinduced change in anisotropy. The independence of the response on the field (magnetization) direction means that switching the direction of the magnetization leads to a reversal of the photoinduced anisotropy contribution[3]. In contrast, the difference signal in Fig. 4.2(b), which shows polarization independent dynamics is thus a totally different kind of excitation.

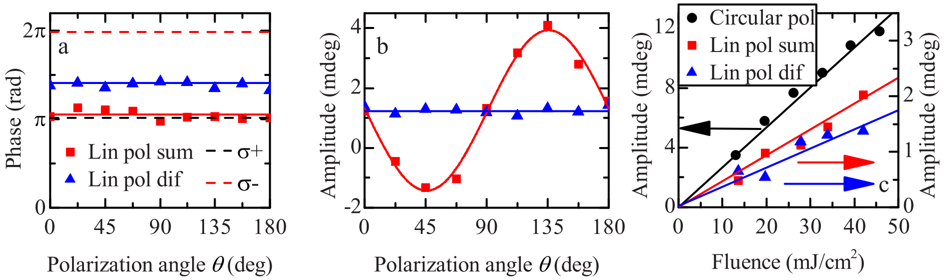

Figure 4.3: Several characteristics of the observed magnetization dynamics. Initial phase (a) and oscillation amplitude (b) of the sum and difference data as a function of the azimuthal linear polarization angle. In (a) for comparison, the initial phase of the oscillations shown in Fig. 4.1 are shown as well. For the three data sets in Figs. 4.1 and 4.2 the dependence of the amplitude on the pump fluence is shown in (c). The solid lines are guides to the eye. An external field of 3 kG was applied.

We would like to add the comment here that contrary to the results reported in Ref. [3] the $\sin 2\theta$ dependence of the oscillation amplitude is not centered around zero. This might indicate that in the sum signal there is an oscillation component that, like in the difference signal, does not depend on the polarization of the light. However as we cannot isolate this oscillation it is difficult to say something about its origin. Its polarization independent character might however suggest the same origin as the oscillations observed in the difference signal.

From Fig. 4.3(c) we see that the amplitude of all three datasets is approximately linear with the pump fluence up to 50 mJ/cm^2. For excitation with circular polarization we have obtained data with larger fluences as well. At these higher fluences non-linear behaviour starts to become visible. The reason for this non-linear behaviour will be discussed in the next chapter. The fluence dependence for the sum and difference of the signal obtained with linear polarization is measured at a polarization angle of $\theta = 0$ deg. For this polarization angle the amplitude of the two datasets is comparable.

4.4 Magnetic Field dependence of the magnetization dynamics

To better understand the differences and similarities between the three different types of excitations shown in Figs. 4.1 and 4.2 we measured their magnetic field dependencies. For the linear polarization the field dependence is measured at the azimuthal polarization angle of 135 deg which results in a maximum signal for the sum signal. The dependence of the frequency, damping factor and oscillation amplitude on the external field are discussed in this section.

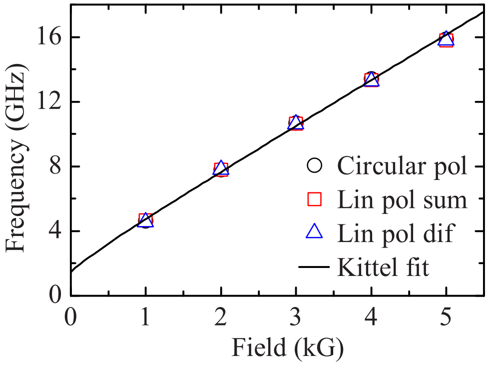

Figure 4.4: The precession frequency as function of the external field is shown for the three data sets in Figs. 4.1 and 4.2. The solid line is a fit using the Kittel formula (Eq. (4.4)).

4.4.1 Frequency and anisotropy

In Fig. 4.4 the frequency versus magnetic field is shown. From this figure we can directly conclude that for all three datasets we excite the same ferromagnetic mode. From this frequency dependence we can also subtract information about the anisotropies in the sample by using the Kittel formula.

The Kittel formula depends strongly on both, the experimental geometry and the magnetic parameters of the sample such as saturation magnetization and anisotropy. To derive the right formula, first the free energy, F for this sample is written as [16],

$$\begin{aligned} F = -H_{\mathrm{ext}} M_{\mathrm{s}} [\cos\theta_{\mathrm{H}} \cos\theta_{\mathrm{m}} + \sin\theta_{\mathrm{H}} \sin\theta_{\mathrm{m}} \cos(\phi_{\mathrm{H}} - \phi_{\mathrm{m}})] \\ + (K_{\mathrm{u}} - 2\pi M_{\mathrm{s}}^2)\sin^2\theta_{\mathrm{m}} + \frac{1}{4} K_{\mathrm{c}} [\sin^2 2\theta_{\mathrm{m}} + \sin^4\theta_{\mathrm{m}} \sin^2 2\phi_{\mathrm{m}}]. \end{aligned} \quad (4.2)$$

The first term is the Zeeman energy, H_{ext} is the externally applied field and M_{s} is the saturation magnetization. The second term is related to the uniaxial anisotropy and the demagnetizing field. K_{u} is the uniaxial anisotropy constant. The last term is the cubic anisotropy energy with K_{c} the cubic anisotropy constant. The angles θ and ϕ are the azimuthal and out of plane angle of the magnetization (subscript m) or external field (subscript H).

From the free energy the Kittel formula is now obtained by [16]

$$\left(\frac{\omega}{\gamma}\right)^2 = \frac{1}{M_{\mathrm{s}}^2 \sin^2\theta_{\mathrm{m}}} \left[\frac{\delta^2 F}{\delta\theta_{\mathrm{m}}^2} \frac{\delta^2 F}{\delta\phi_{\mathrm{m}}^2} - \left(\frac{\delta^2 F}{\delta\theta_{\mathrm{m}} \delta\phi_{\mathrm{m}}} \right)^2 \right]. \quad (4.3)$$

In this equation γ is the gyromagnetic ratio and ω the angular precession frequency. In our experiment H_{ext} is parallel to one of the cubic axes. In this configuration $\theta_{\mathrm{m}} = \theta_{\mathrm{H}} = \pi/2$ and $\phi_{\mathrm{m}} = \phi_{\mathrm{H}} = 0$ which simplifies Eq. (4.3) to

$$\omega = \gamma\sqrt{[H_{\mathrm{ext}} + (4\pi M_{\mathrm{s}} - H_{\mathrm{u}}) + H_{\mathrm{c}}][H_{\mathrm{ext}} + H_{\mathrm{c}}]}, \quad (4.4)$$

where we use the the effective field representation with $H_{\mathrm{u,c}} = 2K_{\mathrm{u,c}}/M_{\mathrm{s}}$. Fitting Eq. (4.4) to the data in Fig. 4.4 gives us a value of 1200 Oe for $(4\pi M_{\mathrm{s}} - H_{\mathrm{u}})$ and a value of 200 Oe for H_{c}. Unfortunately with Eq. (4.4) it is not possible to distinguish between $4\pi M_{\mathrm{s}}$ and H_{u}. With the estimation of 1500 Oe for $4\pi M_{\mathrm{s}}$ [12], H_{u} would be 300 Oe.

4.4.2 Gilbert damping

The Gilbert damping factor α can be obtained from the oscillation lifetime τ by following a similar derivation as in Ref. [17] taking into account the effective fields that are present in the current sample and experimental setup. The final result of this derivation will be:

$$\alpha = \frac{1}{\tau\gamma[H_{\mathrm{ext}} + \frac{1}{2}(4\pi M_{\mathrm{s}} - H_{\mathrm{u}}) + H_{\mathrm{c}}]}. \tag{4.5}$$

The field dependence of the damping factor is shown in Fig. 4.5(a). For all excitation mechanisms the damping is almost equal. This is also what was expected based on Fig. 4.4 which shows that all excitation mechanisms excite the same mode. The small differences we assign to a less accurate determination of the damping at smaller oscillation amplitudes. Furthermore, the damping is decreasing with increasing field in all three cases. This kind of behaviour is observed more often in different kind of materials and ascribed to decoherence of the precession [18–22]. This decoherence of the precession can be a result of the presence of a spread in the frequencies of the oscillations that are excited due to the inhomogeneity of the anisotropies at the sample. At larger fields the relative contribution of the anisotropy field to the precession frequency will be decreasing and thus more coherent oscillations will be present which decreases the observed damping. A spread in anisotropy could exist due to impurities in the sample, for example grains.

To get a better understanding of the origin of the increase in the damping factor towards low fields we will use a model comparable to the one used in Ref. [21]. In this model we use Eq. (4.1) to fit manually the obtained data and derive $\alpha(H_{\mathrm{ext}})$. We obtain the intrinsic damping factor α_{int} as the limit $\alpha(H_{\mathrm{ext}} \to \infty)$ by fitting the data in Fig. 4.5(a) by

$$\alpha = \alpha_{\mathrm{int}} + \alpha_{\mathrm{non-int}} \mathrm{e}^{-H_{\mathrm{ext}}/h} \tag{4.6}$$

Here $\alpha_{\mathrm{non-int}}$ is the non-intrinsic damping factor, hence the part that is caused by the apparent spread in anisotropy. How fast the contribution from $\alpha_{\mathrm{non-int}}$ decreases is characterized by the decay constant h. The resulting fit parameters for the different datasets are given in Table 4.1. From here we will only continue with the dataset obtained with circular polarized light.

With Eq. 4.5 and α_{int} we can calculate $\tau_{\mathrm{int}}(H_{\mathrm{ext}})$. By using $\tau_{\mathrm{int}}(H_{\mathrm{ext}})$ in Eq. (4.1) the obtained curves will not fit the measured data very well. By adding in Eq. (4.1) several oscillatory components with slightly different frequencies, we are able to increase the effective damping due to destructive interference between the different frequency components that are excited. For a specific spread in frequency we obtain

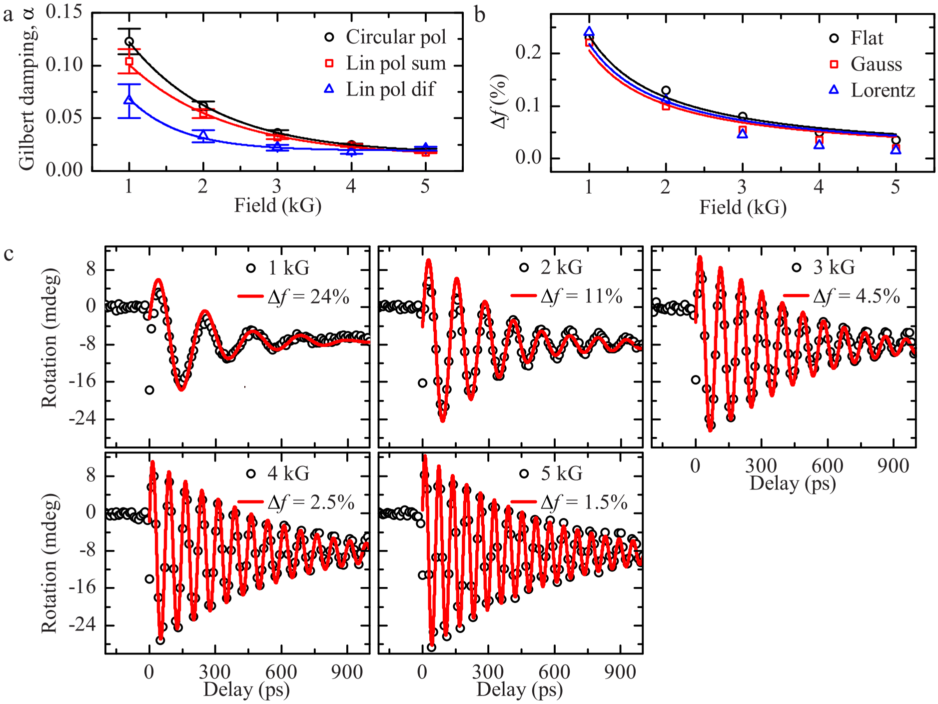

Figure 4.5: In (a) the damping factor as function of the external field is shown for a circular polarized pump pulse (black circles) and for the sum (red squares) and difference (blue triangles) signal of a linear polarized pump pulse. The solid lines are fits to the data using Eq. (4.6). In (b) it is shown how broad the frequency span has to be as a percentage of the center frequency to reproduce the experimentally observed oscillations with Eq. (4.1) taking for the damping term the intrinsic damping as obtained by fitting Eq. 4.6 to the data in (a). This is done for three different distributions for the amplitude weighting. The solid lines are fits using Eq. (4.7). How well the used model traces the experimental data is shown in (c) for a Lorentzian amplitude weighting. The full width at half maximum of the Lorentzian is shown in the legends as a percentage of the center frequency.

Table 4.1: Obtained fitting parameters from fitting Eq. (4.6) to the data shown in Fig. 4.5(a).

Data set	α_{int}	$\alpha_{\mathrm{non-int}}$	h (kG)
Circular pol	0.0161 ± 0.0002	0.243 ± 0.004	1.20 ± 0.02
Lin pol sum	0.013 ± 0.002	0.18 ± 0.03	1.3 ± 0.2
Lin pol dif	0.019 ± 0.002	0.2 ± 0.1	0.7 ± 0.2

Table 4.2: Obtained spread in anisotropy, ΔH_{ani}, from fitting Eq. (4.7) to the data shown in Fig. 4.5(b).

Amplitude weighting	ΔH_{ani} (Oe)
Flat	233 ± 8
Gaussian	206 ± 14
Lorentzian	218 ± 22

curves that closely resemble the experimental data. We performed this procedure with a flat, Gaussian and Lorentzian amplitude weighting for the different frequency components. The result is shown in Fig. 4.5(b). The best match with the experimental data we get with a Lorentzian amplitude weighting. The result of using this weighting for fitting is shown in Fig. 4.5(c). Notice that for the Lorentzian the frequency spread is the Full Width at Half Maximum (FWHM) while for the Gaussian it is twice the variance and for the flat distribution it is the total frequency span.

As already mentioned we think the spread in frequencies might be due to a spread in the anisotropy, ΔH_{ani}. We propose a simple model to link the spread in the frequency, Δf and the applied field to this ΔH_{ani} to be

$$\Delta f = \frac{\Delta H_{\mathrm{ani}}}{H_{\mathrm{ext}}}. \tag{4.7}$$

Fits using this formula are shown by the solid lines in Fig. 4.5(b). The resulting fit parameters are reported in Table 4.2. Notice that the values for the spread in anisotropy are relatively large if we compare them to the values that we found for the uniaxial and cubic anisotropies.

4.4.3 Precession amplitude versus magnetic field: a fingerprint of the excitation character.

The inverse Faraday effect and the photoinduced anisotropy differ significantly by their impulsive and displacive character respectively, that can be illustrated by the field dependence of the precession amplitude. To explain this, using the Landau-Lifshitz equation [23],

$$\frac{\mathrm{d}\mathbf{m}}{\mathrm{d}t} = \gamma(\mathbf{m} \times \mathbf{H}_{\mathrm{eff}}), \tag{4.8}$$

we simulate the expected amplitude dependence on the external field for the observed oscillations.

The effective field, $\mathbf{H}_{\mathrm{eff}}$ is given by

$$\mathbf{H}_{\mathrm{eff}} = \mathbf{H}_{\mathrm{ext}} + \mathbf{H}_{\mathrm{u}} + \mathbf{H}_{\mathrm{c}} + \mathbf{H}_{\mathrm{dem}} + \mathbf{H}_{\mathrm{IFE}}. \tag{4.9}$$

Here, $\mathbf{H}_{\mathrm{dem}}$ the demagnetizing field and $\mathbf{H}_{\mathrm{IFE}}$ the effective field caused by the IFE. These fields are defined as

$$\mathbf{H}_{\mathrm{dem}} = -4\pi m_{\mathrm{z}}, \tag{4.10}$$

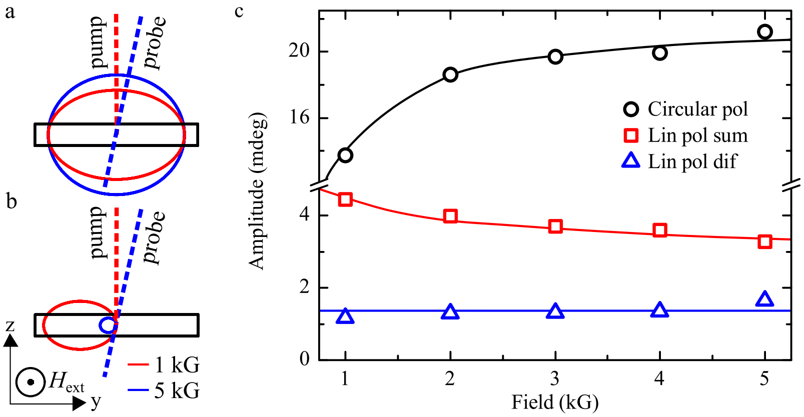

Figure 4.6: Graphical presentation of the differences in oscillation trajectory for oscillations initiated by the inverse Faraday effect and by a photoinduced change in anisotropy are shown in respectively (a) and (b). The experimental amplitude dependence on the external field is shown in (c) for a circular polarized pump pulse (black circles) and for the sum (red squares) and difference (blue triangles) signal of a linear polarized pump pulse. The solid lines are guides to the eye.

and

$$\mathbf{H}_{\text{IFE}} \propto \mathbf{E} \times \mathbf{E}^*. \tag{4.11}$$

Here E is the field amplitude of the light pulse. Hence, $\mathbf{H}_{\text{IFE}}$ only exists during the presence of a light pulse. The two anisotropy fields, $\mathbf{H}_{\text{u}}$ and $\mathbf{H}_{\text{c}}$ can be found by differentiating the last two terms of Eq. 4.2 with respect to $\mathbf{m}$.

From Eqs. (4.8) to (4.11) it is clear that in the presence of a circularly polarized pump pulse the magnetization will start to precess in the sample plane and its final position is determined by the duration and intensity of the laser pulse. The frequency of the initial precession is given by

$$f = \frac{\gamma}{2\pi}|\mathbf{H}_{\text{IFE}}|, \tag{4.12}$$

as $\mathbf{H}_{\text{IFE}}$ determines the precession because $\mathbf{H}_{\text{IFE}}$ is perpendicular to $\mathbf{m}$, while the other components of $\mathbf{H}_{\text{eff}}$ are initially parallel to $\mathbf{m}$. After the laser pulse is gone a new precession will start around $\mathbf{H}_{\text{eff}}$ at that moment, thus with $|\mathbf{H}_{\text{IFE}}| = 0$.

The trajectory of this precession as shown in Fig. 4.6(a) will be elliptical, rather than circular, due to the demagnetizing field. The long axis of the ellipse is oriented in plane. With increasing the external field the relative contribution of the demagnetizing field will decrease and thus the trajectory will more and more look like a circle, hence the out of plane component will increase.

In case of a photo or heat induced change in anisotropy, it is the anisotropy field in Eq. (4.9) that is changed. This change will not only be there during the presence of the pump pulse but also after the light is gone [3]. So in this case the magnetization starts to precess from its equilibrium position around a new effective field instead of a precession of the out of equilibrium magnetization around the unchanged effective field, as in the case of the IFE.

Such a change in anisotropy will result in a decrease of the oscillation amplitude with increasing field [4]. Indeed, the contribution from the change in anisotropy to the effective field will become less relevant for stronger external fields. The path for two different external fields for this situation is illustrated in Fig. 4.6(b).

The experimentally observed oscillation amplitude versus external field is shown in Fig. 4.6(c). Remember that in the experiment we are mainly measuring the out of plane component of the magnetization. When excited with circular polarization the amplitude is increasing with field, as expected from the inverse Faraday effect.

In contrast, the amplitude of the oscillations in the sum signal of the linearly polarized data is decreasing. As we assigned the origin of these oscillations to a photoinduced change in anisotropy earlier (see Section 4.3), this is also what we expect. This field dependence excludes the possibility that the oscillations are initiated by the inverse Cotton-Mouton effect [5, 8].

By calibrating the precession amplitudes and using Eq. (4.8) to take into account the elliptical oscillation trajectory, we are able to derive a value for the involved effective fields. For H_{IFE} this gives 3 kOe and for the change in anisotropy we obtain $\Delta H_{\mathrm{ani}} = 1.3$ Oe. The fields for the inverse Faraday effect and photoinduced anisotropy are of the same order of magnitude as the values found in Ref. [4] of respectively 6 kOe and 0.5 Oe for a higher fluence of 64 mJ/cm^2.

4.5 A new excitation mechanism

Interestingly, the oscillation amplitude for the difference signal of the linear polarized data seems to be constant with changing external field. As a long living displacive effect will always result in a decrease of the oscillation amplitude with increasing external field, the observed oscillations can only be excited with a mechanism that has an impulsive character. From all studies in this chapter we now know the following about the oscillations that we observe in the difference signal of the data that was collected with a linear polarized pump pulse:

1. The oscillations reverse their sign for opposite directions of the external field and thus opposite directions of the magnetization.

2. The oscillations are cosine like.

3. The oscillations are independent on the light polarization.

4. The excitation mechanism of the oscillations has an impulsive character.

This list of characteristics rules out all of the known photo- and opto-magnetic effects as well as a heat induced effect as is made clear in Table 4.3. So what can be the origin of these non-thermal polarization independent oscillations?

Table 4.3: Characteristics of the oscillations observed in the difference signal of the data obtained with a linear polarized pump compared with known excitation mechanisms of magnetization dynamics.

Excitation mechanism	Reversal of sign?	Cosine-like?	Polarization independent?	Impulsive?
Inverse Faraday effect	✗	✗	✗	✓
Inverse Cotton Mouton effect	✗	✓	✗	✓
Photo/heat-induced anisotropy (in plane)	✗	✗	✗/✓	✗
Photo/heat-induced anisotropy (out of plane)	✓	✓	✗/✓	✗

The initial phase and the impulsive charracter suggest that oscillations are induced by an opto-magnetic effect with an effective field in the sample plane, which direction is independend on the direction of $\mathbf{m}$. On a purely phenomenological basis, this effective field could be written as $H_{\text{eff},i} = \chi_{ijk} E_j E_k^*$, where χ is a third rank axial c-tensor. Such field however should still change sign together with $\mathbf{m}$ via the time-reversal property of this tensor, and can thus be ruled out.

The next best guess will be either an out-of-plane PIA or an out-of-plane component of the ICME. Both of them could be schematically written as $H_{\text{eff},i} = \chi_{ijkl} E_j E_k^* m_l$ [3, 5], which however is not a strict definition for the PIA as discussed in [1]. For both these effects the change in sign of $\mathbf{H}_{\text{eff}}$ will lead to $\mathbf{m}$-dependent oscillations. The ICME results in a correct impulsive character, but predicts the initial phase to be different by about 75°. On the other hand, the PIA would result in an almost correct phase, but with a field dependence typical for a displacive effect. A compromise can be reached by a PIA with a life-time comparable to the precessional period: it will result in a semi-impulsive character of the amplitude, as is observed, but simultaneously will still posses an almost correct phase.

An effective field out of the sample plane induced by the in-plane components of the electric field suggests a rather low symmetry of the sample, where the properties are dominated by the out-of-plane direction. It has been shown by second harmonic generation (SHG) experiments [24] that the epitaxial growth indeed leads to a symmetry breaking. Such breaking is expected to be much stronger in BIG that is not stable in the bulk phase. As a confirmation, we measured the non-linear optical response from our samples and found strong and isotropic SHG, indicating the dominating influence of the out-of-plane direction.

We can estimate the field strength for the polarization independent photo-magnetic effect. We find a value of about $H_{\text{imp}} = 1$ Oe when we assume a lifetime of about 10 ps. This value is realistic when compared to the field for the displacive photo-magnetic effect ΔH_{ani}.

4.6 Conclusions

In conclusion, we have found polarization independent oscillations that are excited by a yet unknown excitation mechanism. An impulsive character of these oscillations has been identified by a thorough analysis of the dependence of the oscillation amplitude on the magnetic field. For dynamics excited by a change in anisotropy, the amplitude is decreasing with increasing external field, while when excited by an impulsive action the oscillations will increase or remain constant with increasing external field.

The most likely mechanism responsible for the oscillations is suggested to be a polarization independent short living photo-induced change in the out of plane anisotropy although it does not predict the exact same phase. To obtain the observed oscillation amplitude the effective field pulse has to be 1 Oe strong if its lifetime is 10 ps. This value is realistic when compared to the value found for the long living change in anisotropy ($\Delta H_{\mathrm{ani}} = 1.3$ Oe).

The inverse Faraday and photoinduced change in anisotropy has been observed in the studied bismuth iron garnet as well. Furthermore we have determined the cubic anisotropy to be 200 Oe and $(4\pi M_{\mathrm{s}} - H_{\mathrm{u}})$ to be 1200 Oe. The damping factor is decreasing with increasing field. This dependence on field is explained with a simple model that assumes a spread in the anisotropy, possibly due to sample imperfections.

References

[1] A. Kirilyuk, A. V. Kimel, and Th. Rasing, “Ultrafast optical manipulation of magnetic order,” Rev. Mod. Phys. **82**, 2731 (2010).

[2] A. V. Kimel, A. Kirilyuk, P. A. Usachev, R. V. Pisarev, A. M. Balbashov, and Th. Rasing, “Ultrafast non-thermal control of magnetization by instantaneous photomagnetic pulses,” Nature **435**, 655 (2005).

[3] F. Hansteen, A. Kimel, A. Kirilyuk, and Th. Rasing, “Femtosecond photomagnetic switching of spins in ferrimagnetic garnet films,” Phys. Rev. Lett. **95**, 047402 (2005).

[4] F. Hansteen, A. Kimel, A. Kirilyuk, and Th. Rasing, “Nonthermal ultrafast optical control of the magnetization in garnet films,” Phys. Rev. B **73**, 014421 (2006).

[5] A. M. Kalashnikova, A. V. Kimel, R. V. Pisarev, V. N. Gridnev, A. Kirilyuk, and Th. Rasing, “Impulsive generation of coherent magnons by linearly polarized light in the easy-plane antiferromagnet $FeBO_3$,” Phys. Rev. Lett. **99**, 167205 (2007).

[6] T. Satoh, Y. Terui, R. Moriya, B. A. Ivanov, K. Ando, E. Saitoh, T. Shimura, and K. Kuroda, “Directional control of spin-wave emission by spatially shaped light,” Nat Photon **6**, 662 (2012).

[7] Y. Au, M. Dvornik, T. Davison, E. Ahmad, P. S. Keatley, A. Vansteenkiste, B. Van Waeyenberge, and V. V. Kruglyak, “Direct excitation of propagating

spin waves by focused ultrashort optical pulses," Phys. Rev. Lett. **110**, 097201 (2013).

[8] A. M. Kalashnikova, A. V. Kimel, R. V. Pisarev, V. N. Gridnev, P. A. Usachev, A. Kirilyuk, and Th. Rasing, "Impulsive excitation of coherent magnons and phonons by subpicosecond laser pulses in the weak ferromagnet $FeBO_3$," Phys. Rev. B **78**, 104301 (2008).

[9] A. Stupakiewicz, A. Maziewski, I. Davidenko, and V. Zablotskii, "Light-induced magnetic anisotropy in Co-doped garnet films," Phys. Rev. B **64**, 064405 (2001).

[10] L. Magdenko, E. Popova, M. Vanwolleghem, C. Pang, F. Fortuna, T. Maroutian, P. Beauvillain, N. Keller, and B. Dagens, "Wafer-scale fabrication of magneto-photonic structures in bismuth iron garnet thin film," Microelectronic Engineering **87**, 2437 (2010).

[11] K. Satoh, T. Okuda, H. Yamamoto, H. Onodera, and I. Nakamichi, "Effect of substrate material on growth of Bi-Fe-oxide films by reactive ion beam sputtering," Magnetics in Japan, IEEE Translation Journal on **5**, 1141 (1990).

[12] M. Deb, E. Popova, A. Fouchet, and N. Keller, "Full spin polarization of complex ferrimagnetic bismuth iron garnet probed by magneto-optical faraday spectroscopy," Phys. Rev. B **87**, 224408 (2013).

[13] E. Popova, L. Magdenko, H. Niedoba, M. Deb, B. Dagens, B. Berini, M. Vanwolleghem, C. Vilar, F. Gendron, A. Fouchet, J. Scola, Y. Dumont, M. Guyot, and N. Keller, "Magnetic properties of the magnetophotonic crystal based on bismuth iron garnet," Journal of Applied Physics **112**, 093910 (2012).

[14] M. Deb, E. Popova, A. Fouchet, and N. Keller, "Magneto-optical Faraday spectroscopy of completely bismuth-substituted $Bi_3Fe_5O_{12}$ garnet thin films," Journal of Physics D: Applied Physics **45**, 455001 (2012).

[15] E. Popova, A. F. F. Galeano, M. Deb, B. Warot-Fonrose, H. Kachkachi, F. Gendron, F. Ott, B. Berini, and N. Keller, "Magnetic anisotropies in ultrathin bismuth iron garnet films," Journal of Magnetism and Magnetic Materials **335**, 139 (2013).

[16] S. A. Manuilov and A. M. Grishin, "Pulsed laser deposited $Y_3Fe_5O_{12}$ films: Nature of magnetic anisotropy II," Journal of Applied Physics **108**, 013902 (2010).

[17] M. Djordjevic, *Magnetization dynamics in all-optical pump-probe experiments: spin-wave modes and spin-current damping*, Ph.D. thesis, Georg-August-Universität zu Göttingen (2006).

[18] G. Counil, J.-V. Kim, T. Devolder, C. Chappert, K. Shigeto, and Y. Otani, "Spin wave contributions to the high-frequency magnetic response of thin films obtained with inductive methods," Journal of Applied Physics **95**, 5646 (2004).

[19] M. Djordjevic, G. Eilers, A. Parge, M. Münzenberg, and J. S. Moodera, "Intrinsic and nonlocal Gilbert damping parameter in all optical pump-probe experiments," Journal of Applied Physics **99**, 08F308 (2006).

[20] S. Serrano-Guisan, K. Rott, G. Reiss, and H. W. Schumacher, "Inductive and magneto-resistive measurements of Gilbert damping in Ni 81 Fe 19 thin films and microstructures," Journal of Physics D: Applied Physics **41**, 164015 (2008).

[21] J. Walowski, M. D. Kaufmann, B. Lenk, C. Hamann, J. McCord, and M. Münzenberg, "Intrinsic and non-local Gilbert damping in polycrystalline nickel studied by Ti:sapphire laser fs spectroscopy," Journal of Physics D: Applied Physics **41**, 164016 (2008).

[22] H.-S. Song, K.-D. Lee, J.-W. Sohn, S.-H. Yang, S. S. P. Parkin, C.-Y. You, and S.-C. Shin, "Observation of the intrinsic Gilbert damping constant in Co/Ni multilayers independent of the stack number with perpendicular anisotropy," Applied Physics Letters **102**, 102401 (2013).

[23] L. D. Landau and E. M. Lifshitz, "On the theory of the dispersion of magnetic permeability in ferromagnetic bodies," Phys. Z. Sowjet. **8**, 153 (1935).

[24] V. N. Gridnev, V. V. Pavlov, R. V. Pisarev, A. Kirilyuk, and T. Rasing, "Second harmonic generation in anisotropic magnetic films," Phys. Rev. B **63**, 184407 (2001).

Chapter 5

Spectral study of magnetization dynamics in Bismuth Iron Garnet[1]

While in the previous chapter the magnetization dynamics in bismuth iron garnet was studied at a single probe wavelength, here we study the differences in the observed dynamics when different probe wavelengths are used. This spectral study gives access to the individual dynamics of the two ferrimagnetically coupled iron sites. After a brief introduction to the importance and possibility of measuring the dynamics of different sublattices independently, the sample and experimental setup will be discussed. The dependence of the magnetization dynamics on the probe wavelength and the pump fluence will be discussed in respectively the third and fourth section. It will be shown that the observed spectral dependence can be explained by a pump induced change in the relative contributions from the two iron sites to the total Faraday signal. In the fifth section an alternative interpretation of the data is discussed that explains the data by a shift of the energy level of one of the dipole transitions responsible for the Faraday signal. In the last section the conclusions are given.

5.1 Introduction

Studying the magnetization dynamics on the femtosecond time scale can reveal very useful information about the exchange interaction [1]. It thus becomes interesting to be able to probe the dynamics of the different sublattices of anti-ferromagnetic and ferrimagnetic materials independently.

Recently, for multisublattice metallic magnetic alloys it is shown that with time-resolved X-ray magnetic circular dichroism (XMCD) [2] the dynamics of the individual anti-ferromagnetically coupled elements can be measured. Due to the element spe-

---

[1] This work is realized in collaboration with M. Deb, E. Popova and N. Keller from the Université de Versailles Saint-Quentin-en-Yvelines

cific absorption resonances it was possible to measure an unexpected difference in the dynamics of the Fe and Gd spins of a FeGdCo alloy. Later it was also shown that for specific materials a similar element specific sensitivity can be obtained with spectrally resolved optical pump probe measurements [3]. However for a material like bismuth iron garnet (BIG), the different sublattices concern both Fe, so that it becomes hard/impossible to distinguish them by XMCD. The question is whether this could be done with optics.

Here we perform a spectral study of a ferrimagnetic BIG thin film. It is suggested [4] that the spectral dependence of the Faraday rotation makes it possible to selectively probe the two anti-ferromagnetically coupled iron sites. This site specific probing would be possible if the spectral Faraday rotation caused by two transitions located on the two different iron sites have only a minor spectral overlap. Hence despite the fact that the magnetic properties of this material are determined by only one single element (Fe), this should make it in principle still possible to be sensitive to the magnetically differently oriented iron sites. Although we do not observe any difference in dynamics between the two sites, we do observe a pump induced change in the magneto-optical Faraday spectrum. This change is different for the parts in the spectrum that can be identified to originate from either one or the other iron sublattice.

5.2 Sample and experimental setup

The same sample as in the previous chapter is investigated, a 200 nm thick single crystalline and single phase BIG film grown epitaxially on a substituted $\mathrm{Gd_3Ga_5O_{12}}(001)$ substrate by pulsed laser deposition. BIG has a crystal structure that is expected to be similar to yttrium iron garnet as is shown in Fig. 5.1(a). Like yttrium iron garnet it is then expected to have a magnetization of 5 μ_B (Bohr magneton) per formula unit, but experimentally only values up to 4.4 μ_B per formula unit are observed [5]. BIG is a ferrimagnet and the iron elements present in the crystal structure are distributed over tetrahedral sites (24× in a unit cell) and octahedral sites (16× in a unit cell) [6]. The tetrahedral and octahedral sites are anti-ferromagnetically coupled.

Among the iron garnets, BIG is known to have the largest magneto-optical response. It was shown before that the Faraday spectrum in bismuth substituted yttrium iron garnet, as well as for BIG can be explained by dipole transitions originating from the tetrahedral and octahedral iron sites [4, 8, 9]. The enhanced magneto-optical effect in BIG as compared to yttrium iron garnet is considered to be a result of an increase in the spin-orbit splitting of the energy levels involved in the dipole transitions. This increase in the spin-orbit splitting is assigned to an interaction between the bismuth and iron atoms [10].

It is interesting to consider the Faraday spectrum of the current sample in more detail. For this reason in Fig. 5.1(b) the main result from Ref. [4] is shown where a very similar sample was studied. The figure shows the measured Faraday spectrum together with fits to the data using a model based on two dipole transitions. The separate contributions from the tetrahedral and octahedral site are shown as well.

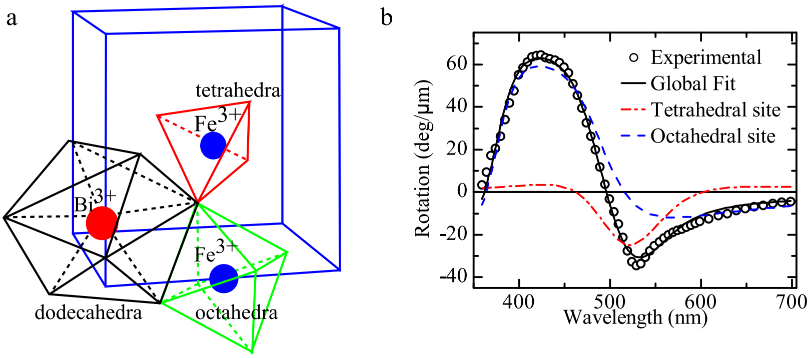

Figure 5.1: In (a) the arrangement of the different sites in bismuth iron garnet are shown. In (b) the Faraday spectrum is shown together with the theoretical contributions from the two different iron sites. This Faraday spectrum is measured on a sample that is expected to be very similar to the sample measured in this chapter. Figure (a) is adapted from [7] while figure (b) is adapted from [4]

According to the model suggested by the authors of Ref. [4] the contribution from the tetrahedral site to the Faraday rotation is zero at a wavelength of about 460 nm, while the contribution from the octahedral site is close to a maximum at the same wavelength. At a wavelength of about 520 nm the contribution from the two iron sites is reversed. Now the contribution from the octahedral site is zero while the contribution from the tetrahedral site is close to its maximum. This means that by choosing the probe wavelength to be 460 or 520 nm we will be able to measure the magnetization dynamics in the octahedral, respectively tetrahedral iron site.

The experimental setup that we use in this chapter is basically the same as in the previous chapter. The only difference is that we use here the optical parametric amplifier (OPA) to tune the wavelength of the probe between 430 and 560 nm. In short the setup is an optical pump probe setup in transmission geometry, an amplified laser system giving 40 fs, 800 nm pulses at a 1 kHz repetition rate is used for the input of the OPA and as the pump in the pump-probe scheme, a balanced detector combined with a lock-in is used for measuring the Faraday rotation, and an electromagnet supplies an in-plane magnetic field of 3 kOe.

The alignment of the pump beam was exactly perpendicular to the sample while the probe made an angle of about 10 deg with the sample normal. Depending on the measurement the spot size of the pump was 130 or 365 μm and that of the probe about 26 μm. Other than in the measurements of the fluence dependence, the pump fluence was 27 mJ/cm^2. The probe pulse energy was at least 1000× smaller than that of the pump. Here we only use circularly polarized light for the pump pulse, while the probe pulse polarization is linear.

Like in the previous chapter, the measured magnetization dynamics is fitted with

$$y = y_0 + (B\mathrm{e}^{R_0 t}) + A\mathrm{e}^{-t/\tau}\sin(2\pi f t - \phi). \tag{5.1}$$

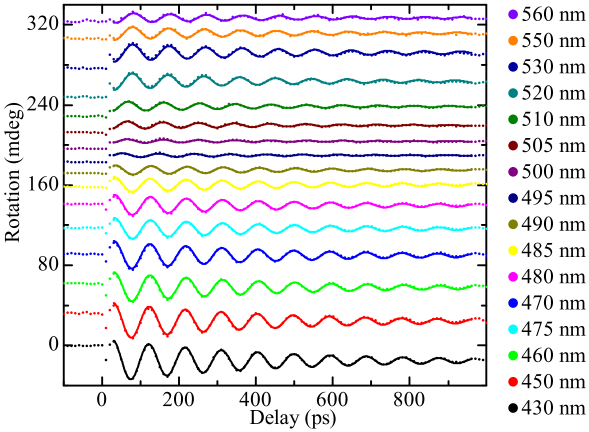

Figure 5.2: Magnetization dynamics measured at different probe wavelengths. The solid lines are fits using Eq. (5.1).

Here y_0 is the offset, A is the amplitude of the oscillations, f is the frequency, τ is the oscillation lifetime, ϕ is the initial phase and t is the time. The term $Be^{R_0 t}$ is only used when it improved the fit.

Here we would like to make the note that besides probing at 460 and 530 nm, it could also be interesting to pump at those two wavelengths to separately excite the two iron sites. Although an attempt was done with a pump at 400 nm, we could not reach similar high fluences as with an 800 nm pump in the experimental setup that was used. As the absorption at 400 nm is higher, this does not have to be a limitation. However, except in the oscillation amplitude we did not observe any other significant difference in the measured magnetization dynamics between using a 400 or 800 nm pump pulse.

5.3 Probe wavelength dependence

The measured magnetization dynamics at a range of probe wavelengths is shown in Fig. 5.2. The data is measured with left circularly polarized light. The mechanism for the excitation of the magnetization precession is identified as the inverse Faraday effect. For more details see the previous chapter or Refs. [11] and [12]. A clear disappearance of the oscillations is visible around 500 nm. Furthermore, the phase of the oscillations observed at wavelengths longer than 500 nm is shifted by π compared to the phase of the oscillations observed for a probe wavelength shorter than 500 nm. Alternatively one could state that the amplitude of the signal above 500 nm reverses sign. The latter statement is more in line with the known static Faraday rotation as shown in Fig 5.1(b).

By fitting the data with Eq. (5.1) with the amplitude defined to be positive we

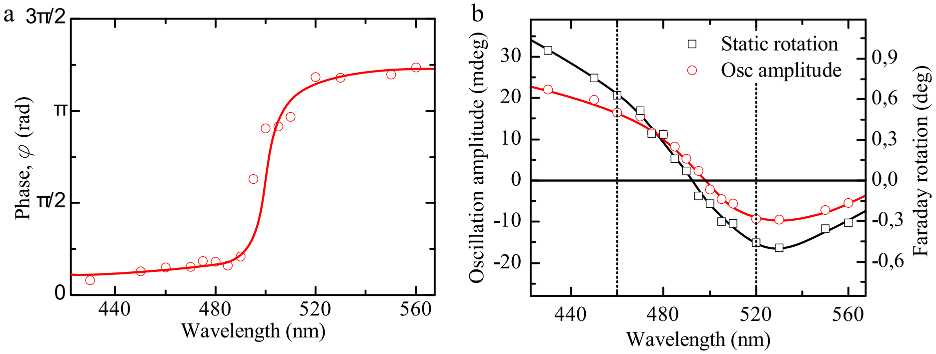

Figure 5.3: (a) The initial phase as obtained from a fit to the raw data with Eq. (5.1). A clear π phase change is observed at about 500 nm. The phase shift of π in (a) can also be represented as a change in the sign of the oscillation amplitude as is done in (b). For comparison the static spectral dependence of the hysteresis loop amplitude is given in (b) as well. A small shift of the zero crossing between static and dynamic spectral dependence is observed. The dashed lines indicate the wavelengths for which we expect to be sensitive to the octahedral or tetrahedral site only. The solid lines are guides to the eye.

obtain the phase versus wavelength graph as shown in Fig. 5.3(a). A clear phase shift of π is visible while going from 480 to 520 nm. In Fig. 5.3(b) the oscillation amplitude is shown, where we have used Fig. 5.3(a) to determine the spectral region with a Faraday rotation of opposite sign.

Other than the phase shift or sign change of the amplitude, the observed dynamics resulting from the tetrahedral and octahedral iron sites appear to be identical. Actually, at the time scale as shown in Fig. 5.2 we did not expect to observe a difference because effects due to the exchange interaction are only expected to occur on a shorter time scale directly after excitation with the pump, e.g. in the first few picoseconds. Although we did perform measurements at those shorter time scales, no difference in the dynamics was observed.

However, comparing the oscillation amplitude versus wavelength with the static Faraday spectrum we did observe a significant difference. For this comparison the static Faraday rotation spectrum is shown in the same graph in Fig. 5.3(b) as the oscillation amplitude. The static Faraday spectrum is also obtained in the same experimental geometry as the dynamic measurements. Hence due to the in-plane field and the small angle of the probe beam, the obtained maximum rotation from the hysteresis loop is far from the real maximum rotation which is expected to be like shown in Fig. 5.1(b). Yet, the obtained static spectrum does reliably represent the relative spectral dependence.

The uncertainty in wavelength in the data of Fig. 5.3 is related to the spectrum of the probe pulse from the OPA. This spectrum is about 5 to 10 nm broad. The static and dynamic measurements however, are performed with exactly the same settings of the OPA, thus the data points at a single wavelength are directly comparable.

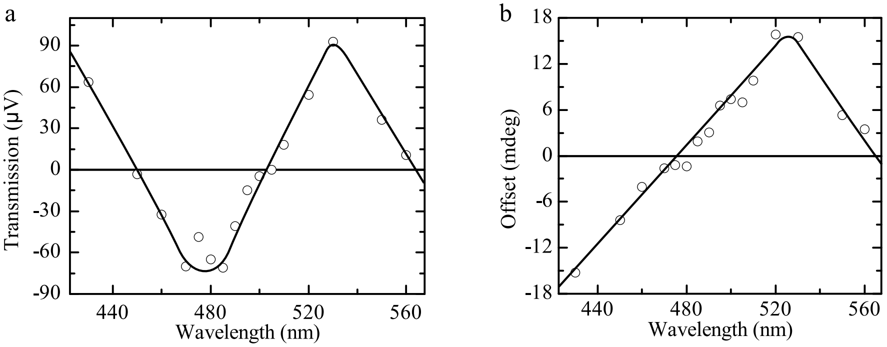

Figure 5.4: In (a) the pump induced change in transmission versus the probe wavelength is shown. In (b) the wavelength dependence of the offset is shown. This offset is obtained from fitting the data in Fig. 5.2 with Eq. 5.1. The solid lines are guides to the eye.

In Fig. 5.3(b) a difference between the two curves can be observed at the wavelength at which a zero crossing occurs. Hence the wavelength at which the two contributions from the tetrahedral and octahedral iron sites cancel each other is different and is shifted to the red by about 7 nm.

Although we do not have a definite answer about the mechanism behind this shift, we will suggest below that it can be explained by a pump induced change in the Faraday effect. This change in the Faraday effect most likely originates from a photo-induced change of the electronic structure. Such a change might influence the dipole transitions that are responsible for the optical and magneto-optical constants. As the Faraday spectrum is formed by two different dipole transitions, it is possible that the spectral contributions from the two different iron sites to the Faraday rotation are changed in a different way.

The observation of a pump induced change in the transmission as shown in Fig. 5.4(a) gives another indication that the optical constants are changed by the pump pulse. It should be noted that Fig. 5.4(a) is not calibrated to take into account a difference in probe intensity or the spectral sensitivity of the detector.

Considering the data as shown in Fig. 5.3(b) it seems that a difference in the relative change in the amplitude of the Faraday rotation originating from the two different iron sites is responsible for the observed effect. The contribution from the tetrahedral site seems to be relatively reduced as compared to the contribution from the octahedral site. From Fig. 5.1(b) it is clear that if the relative contribution from the tetrahedral site is decreasing, the point for zero Faraday rotation will shift to the red.

We would like to note here that a different relative scaling of the left and right axes in Fig. 5.3(b) could lead to a different interpretation. One such alternative is discussed in Section 5.5. However, the choice to represent the data as is done in Fig. 5.3(b) is not random. It is based on the measured wavelength dependence of the offset, y_0 which is shown in Fig. 5.4(b).

The offset is a dc change in the observed Faraday rotation after the pump pulse hits the sample. In the bottom curve in Fig 5.2 the presence of an offset is clearly visible. The oscillation is not centered around zero but around a value below zero. This value is equal to the offset, y_0. A zero crossing of this offset occurs at a wavelength of about 475 nm. Thus at 475 nm the Faraday rotation does not seem to be changed. For this reason Fig. 5.3(b) is scaled such that the static spectrum of the Faraday rotation and the dynamic spectrum cross each other at this wavelength of 475 nm.

The negative offset for wavelengths shorter than 475 nm agrees well with the decrease in Faraday rotation which seems to occur if the data is represented as is done in Fig. 5.3(b). The positive value of the offset for wavelengths longer than 475 nm agrees also with the increase in the Faraday rotation visible in this spectral region. Where it should be noted that due to the negative sign of the Faraday rotation the absolute rotation might decrease.

We would like to emphasize that the observed change in the Faraday rotation is not due to demagnetization, a process that is often observed in metallic magnetic materials [13, 14]. Here we study a dielectric material and thus the interaction between spins and phonons or electrons is expected to be too slow for demagnetization to occur on the picosecond timescale[1]. The change in Faraday rotation we measure here already reaches its maximum after the first few picosecond after the pump illumination. This is most clearly observed by looking at the offset of the oscillations in Fig. 5.2. This offset reaches its maximum after the first measurement point after the pump illumination.

5.4 Pump fluence dependence

In the previous section we ascribed the observed effects to be pump induced. It is therefore interesting to perform a pump fluence dependence. We performed a fluence dependence of the magnetization dynamics at four different probe wavelengths. Especially the behavior of the initial phase, offset and the oscillation amplitude with increasing fluence will be discussed in this section.

In Fig. 5.5(a) the fluence dependence of the initial phase is shown for four different wavelengths. While the initial phase for a probe wavelength of 450 and 530 nm is constant with fluence, a decrease in the phase is visible for the other two wavelengths. As the latter wavelengths are close to the zero Faraday rotation point, the most straightforward explanation for this decrease in phase is a further shift of the zero rotation point to longer wavelengths. From Fig. 5.3(a) we know that when the zero rotation point is crossed the phase will shift from 0 to π. Hence if this point is shifting further to the red then the phase shift will occur at longer wavelengths, and thus the initial phase at a wavelength around this zero point will show a decrease. In the investigated fluence region the initial phase continuously decreases for the wavelengths of 495 and 505 nm. This means that in the investigated fluence region the magneto-optical constants change proportionally to the pump fluence.

A second indication for this further modification of the magneto-optical constants with increasing pump power is obtained from the offset dependence on the fluence

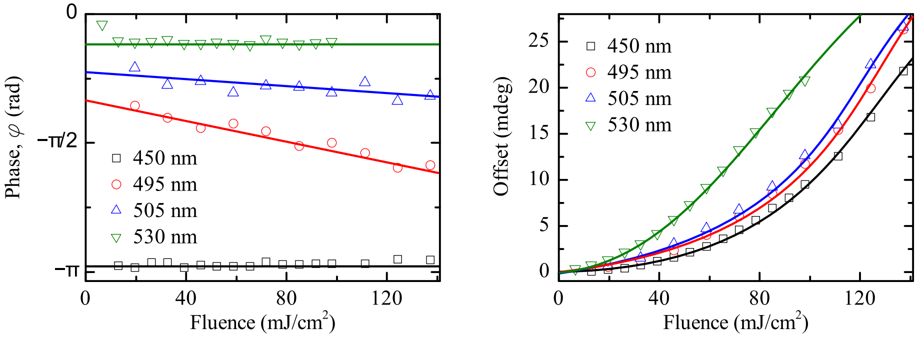

Figure 5.5: The initial phase (a) and absolute value of the offset (b) of the magnetization dynamics for four different probe wavelengths as a function of the pump fluence. The solid lines are guides to the eye.

as shown in Fig. 5.5(b). This value keeps on increasing for the fluences that are measured. Furthermore from this figure it is very clear that the rotation at 530 nm, which is mainly ascribed to the tetrahedral site, is changing much faster as compared to the rotation at 450 nm which is assigned to the octahedral site. This agrees well with the earlier statement that the relative contribution from the tetrahedral site decreases more than the contribution from the octahedral site.

Another interesting dependence to consider is the oscillation amplitude versus fluence which is shown in Fig. 5.6. We assigned the inverse Faraday effect as the starting mechanism for the magnetic precession. However, for the inverse Faraday effect a linear dependence of the oscillation amplitude on the light fluence is expected, hence

$$A = \zeta P F(\lambda, P) d. \tag{5.2}$$

Here ζ is a scaling constant, P is the fluence, F the Faraday rotation per unit distance, λ the wavelength, and d the sample thickness.

Although the amplitude depends approximately linear on the laser fluence up to 70 mJ/cm^2, above this value a clear deviation from the linear dependence is observed. This deviation can be explained by the variation in the magneto-optical constants with increasing fluence. As already indicated in Eq. (5.2), the Faraday rotation can be written as a function of the wavelength and the laser fluence. The wavelength dependence is given by the separate contributions from the two iron sites as shown in Fig. 5.1(b). We do not know the exact dependence of the Faraday rotation on the laser fluence but below we will use the following very simple model which already shows the basic characteristics that are observed in the measurements,

$$F = (1 - \eta P) F_{\mathrm{tetrahedral}}(\lambda) + (1 - \kappa P) F_{\mathrm{octahedral}}(\lambda). \tag{5.3}$$

Here η and γ are scaling constants that indicate the decrease of the Faraday rotation from the tetrahedral and octahedral iron site. The static Faraday rotation from those

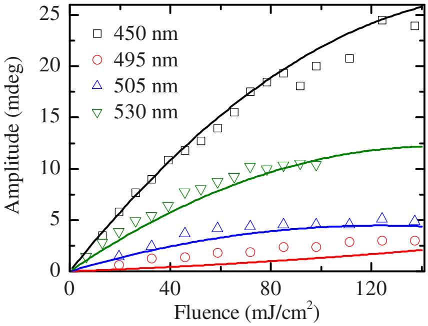

Figure 5.6: The oscillation amplitude of the magnetization dynamics for four different probe wavelengths as a function of the pump fluence. The measured data is shown with the open symbols. The solid lines are calculated according to Eq. (5.2) using for F Eq. (5.3) For ζ, η and κ the values of respectively $2.7 \cdot 10^{-5}$, $3.6 \cdot 10^{-3}$ and $2.8 \cdot 10^{-3}$ cm^2/mJ are used.

Table 5.1: Resulting values for ζ, η and κ (cm^2/mJ) from fitting the amplitude versus wavelength at fixed fluence P (mJ/cm^2) with the combination of Eqs. (5.2) and (5.3). An x in the error columns of the table means that the value is fixed. The x for η and κ represent that those variables are not taken into account.

P	ζ	ζ_{Err}	η	η_{Err}	κ	κ_{Err}
19.6	$2.7 \cdot 10^{-5}$	$0.2 \cdot 10^{-5}$	x	x	x	x
32.7	$2.5 \cdot 10^{-5}$	$0.2 \cdot 10^{-5}$	x	x	x	x
85.0	$2.7 \cdot 10^{-5}$	x	$3.6 \cdot 10^{-3}$	$0.8 \cdot 10^{-3}$	$2.8 \cdot 10^{-3}$	$0.5 \cdot 10^{-3}$
98.0	$2.7 \cdot 10^{-5}$	x	$4.0 \cdot 10^{-3}$	$0.5 \cdot 10^{-3}$	$3.2 \cdot 10^{-3}$	$0.3 \cdot 10^{-3}$

sites are given by $F_{\text{tetrahedral}}(\lambda)$ and $F_{\text{octahedral}}(\lambda)$.

As the scaling constants ζ, η and κ are assumed to be the same for all wavelengths we determined their approximate values by fitting the data points at a fixed fluence and variable wavelength. Unfortunately the three constants are not independent of each other. For this reason we first calculated an estimation for ζ at the lower fluences where the terms $(1 - \eta P)$ and $(1 - \eta P)$ are still reasonably close to one. In a next step we calculated estimations for η and κ by performing a fit at the higher fluences using the already found estimation for ζ. The resulting values from this procedure are shown in Table 5.1.

The values found for different fluences lie within the fitting error from each other and thus are reasonable values for this model. Using these values the expected fluence dependence of the amplitude of the model is shown by solid lines in Fig. 5.6. Although the model and the experimental data do not overlap perfectly they do show that the amplitude dependence on the fluence can be different from linear due to the power

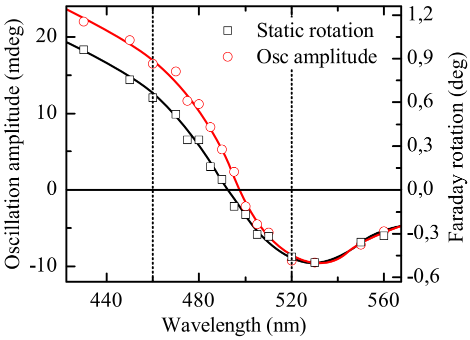

Figure 5.7: Here the same data as in Fig. 5.3(b) is shown but with other scaling of the axes. In this representation the change of the wavelength of the zero crossing is suggested to result from a shift of the Faraday spectrum related to the octahedral iron site. The dashed lines indicate the wavelengths for which we expect to be sensitive to the octahedral or tetrahedral site only. The solid lines are guides to the eye.

dependence of the Faraday rotation.

5.5 An alternative explanation

In the previous two sections we assigned the change in the zero crossing mainly to be due to a difference in the relative change of the contribution to the Faraday spectrum from the two iron sites. However the zero crossing could also change if the energy level related to the dipole transition located on the octahedral site decreases, hence the Faraday spectrum from this site will shift to longer wavelengths. If the oscillation amplitude spectrum is compared to the static rotation as in Fig. 5.7 this seems to be a reasonable explanation. The only difference between this figure and Fig. 5.3(b) is the relative scaling of the axes.

The data points of the oscillation amplitude in Fig. 5.7 for wavelengths longer than 500 nm follow the static Faraday rotation spectrum reasonably well and thus the tetrahedral contribution to the Faraday spectrum appears not to be influenced by the pump pulse. While for the data points at shorter wavelengths a clear deviation is visible and the spectrum appears to be shifted to the right.

Although with this interpretation the phase dependence on the fluence in Fig. 5.5(a) can be explained equally well as with the interpretation used in the previous sections, it is not possible to relate Figs. 5.4(b), 5.5(b) and 5.6 to this interpretation. For this reason we think the interpretation as given in the previous sections is more likely.

5.6 Conclusions

In this chapter we have shown that the relative contributions from the tetrahedral and octahedral iron sites to the Faraday spectrum change after excitation with a femtosecond laser pulse. The contribution from the tetrahedral site reduces relatively more than the contribution from the octahedral iron site.

This results in a shift of the zero Faraday rotation point by about 7 nm to the red at a fluence of 27 mJ/cm^2. By increasing the fluence the observed red shift increases as is deduced from the phase, offset and amplitude dependence on the pump fluence. The observed change in Faraday rotation can account for the non-linear dependence of the oscillation amplitude on the laser fluence.

The exact mechanism responsible for the change in the contribution from the two different iron sites remains unclear. We suggest it is related to a light induced change in the electronic structure of the material which on its turn influences the dipole transitions that are responsible for the magneto-optical properties of the sample.

References

[1] A. Kirilyuk, A. V. Kimel, and Th. Rasing, “Ultrafast optical manipulation of magnetic order,” Rev. Mod. Phys. **82**, 2731 (2010).

[2] I. Radu, K. Vahaplar, C. Stamm, T. Kachel, N. Pontius, H. A. Durr, T. A. Ostler, J. Barker, R. F. L. Evans, R. W. Chantrell, A. Tsukamoto, A. Itoh, A. Kirilyuk, Th. Rasing, and A. V. Kimel, “Transient ferromagnetic-like state mediating ultrafast reversal of antiferromagnetically coupled spins,” Nature **472**, 205 (2011).

[3] A. R. Khorsand, M. Savoini, A. Kirilyuk, A. V. Kimel, A. Tsukamoto, A. Itoh, and Th. Rasing, “Element-specific probing of ultrafast spin dynamics in multisublattice magnets with visible light,” Phys. Rev. Lett. **110**, 107205 (2013).

[4] M. Deb, E. Popova, A. Fouchet, and N. Keller, “Magneto-optical Faraday spectroscopy of completely bismuth-substituted $Bi_3Fe_5O_{12}$ garnet thin films,” Journal of Physics D: Applied Physics **45**, 455001 (2012).

[5] E. Popova, A. F. F. Galeano, M. Deb, B. Warot-Fonrose, H. Kachkachi, F. Gendron, F. Ott, B. Berini, and N. Keller, “Magnetic anisotropies in ultrathin bismuth iron garnet films,” Journal of Magnetism and Magnetic Materials **335**, 139 (2013).

[6] F. Hansteen, *Ultrafast Optical Control of Magnetization in Ferrimagnetic Garnets*, Ph.D. thesis, Radboud University Nijmegen (2006).

[7] M. A. Gilleo and S. Geller, “Magnetic and crystallographic properties of substituted yttrium-iron garnet, $3Y_2O_3 \cdot xM_2O_3 \cdot (5-x)Fe_2O_3$,” Phys. Rev. **110**, 73 (1958).

[8] G. F. Dionne and G. A. Allen, “Spectral origins of giant Faraday rotation and ellipticity in Bi-substituted magnetic garnets,” Journal of Applied Physics **73**, 6127 (1993).

[9] G. F. Dionne and G. A. Allen, “Molecular-orbital analysis of magneto-optical Bi-O-Fe hybrid excited states,” Journal of Applied Physics **75**, 6372 (1994).

[10] S. Wittekoek, T. J. A. Popma, J. M. Robertson, and P. F. Bongers, “Magneto-optic spectra and the dielectric tensor elements of bismuth-substituted iron garnets at photon energies between 2.2-5.2 eV,” Phys. Rev. B **12**, 2777 (1975).

[11] A. V. Kimel, A. Kirilyuk, P. A. Usachev, R. V. Pisarev, A. M. Balbashov, and Th. Rasing, “Ultrafast non-thermal control of magnetization by instantaneous photomagnetic pulses,” Nature **435**, 655 (2005).

[12] F. Hansteen, A. Kimel, A. Kirilyuk, and Th. Rasing, “Femtosecond photomagnetic switching of spins in ferrimagnetic garnet films,” Phys. Rev. Lett. **95**, 047402 (2005).

[13] E. Beaurepaire, J.-C. Merle, A. Daunois, and J.-Y. Bigot, “Ultrafast spin dynamics in ferromagnetic nickel,” Phys. Rev. Lett. **76**, 4250 (1996).

[14] B. Koopmans, M. van Kampen, J. T. Kohlhepp, and W. J. M. de Jonge, “Ultrafast magneto-optics in nickel: Magnetism or optics?” Phys. Rev. Lett. **85**, 844 (2000).

Chapter 6

Degree of coherence in a magnon Bose-Einstein Condensate[1]

The high quality of garnet samples has resulted in a large number of magnetic model studies carried out in them. In the past this was research on static and dynamic properties of domains and domain walls [1]. Now this has become the spin-hall effect and its derivatives [2, 3].

A very intriguing phenomenon that can also be observed in garnets, is the Bose-Einstein condensation (BEC) of magnons [4]. In contrast to ultra cold atomic gases [5, 6], in the magnetic system the BEC phenomenon can be observed at room temperature. Contrary to the ferromagnetic mode that is typically observed in an optical femtosecond pump-probe experiment, the magnon excitations that form the condensate have a k-vector unequal to zero.

The study of the coherence of such a magnon condensate allows to detect the strength of the interaction of the spin system with an external bath. In this chapter we describe the experiments to determine the coherence of the magnon condensate in yttrium iron garnet by measuring its frequency width using a continuous wave microwave pump and a femtosecond pulsed laser probe.

6.1 Introduction

Since the first observation in dilute gases [5, 6], Bose-Einstein condensation [7, 8] has been observed in other systems as well where the condensation of quasi-particles is taking place. These systems include excitons [9], polaritons [10–14], and magnetic dimers in spingap materials [15–17]. The system we study here is that of magnons in yttrium iron garnet (YIG). The BEC in this system was discovered recently [4] and

---

[1] This work is realized in collaboration with P. Nowik-Boltyk, O. Dzyapko, V. Demidov and S. Demokritov from the University of Münster

caused a lot of interest [18–21]. Compared to the other systems it is worth noting that a magnon-BEC is the only system where the lowest energy state is twice degenerate. Furthermore it is one of the few systems, together with polariton systems [22], where condensation takes place at room temperature.

From its name, Bose-Einstein condensation can occur for particles that obey Bose-Einstein statistics. In this case, the particle density n in a state with energy ε is given by

$$n(\varepsilon) = \frac{1}{\mathrm{e}^{\frac{\varepsilon-\mu}{\mathrm{k_B}T}} - 1}. \tag{6.1}$$

In this equation μ is the chemical potential of the system, $\mathrm{k_B}$ the Boltzmann constant and T the temperature. From this equation it follows that μ has to be smaller than the minimum energy level ϵ_{min}. The chemical potential depends on the particle density and with increasing density, μ will increase. Above a critical particle density for which $\mu = \epsilon_{\mathrm{min}}$, the fraction of particles that cannot be described by Eq. (6.1) will form a condensate in the lowest energy state [23, 24]. The critical particle density depends on the temperature as well. This temperature dependence is used to achieve condensation of dilute gases at low temperatures. In magnon systems the particle density is increased at a given temperature by increasing the number of magnons in the system. This makes room temperature condensation possible.

Strictly speaking Eq. 6.1 is only valid in thermal equilibrium. For a magnon system in thermal equilibrium the chemical potential μ is zero as magnons are continuously created and annihilated and thus the number of particles is not conserved. Hence no condensation in thermal equilibrium can occur. However if magnons are continuously added to the system and the magnon-magnon relaxation time, $\tau_{mag-mag}$, is shorter than the spin-lattice relaxation time, $\tau_{spin-latt}$, a quasi-equilibrium is created. Due to magnon-magnon interactions the magnons will reach a thermal equilibrium before they leave the system by spin lattice interactions. In such a quasi-equilibrium $\mu \neq 0$ and will be proportional to the number of magnons added to the system. Thus if the number of magnons reaches a critical value, the chemical potential will equal the minimum energy of the system and a condensate can be formed[4]. Yttrium Iron Garnet (YIG) is a perfect candidate for Bose-Einstein condensation as it can have long spin-lattice relaxation times of roughly $\tau_{\mathrm{spin-latt}} = 250$ ns which is longer than the characteristic magnon-magnon relaxation time of $\tau_{mag-mag} = 50$ ns [25].

In theory the condensation should take place in a single coherent state, thus at a single frequency. However, Bose-Einstein condensation of magnons takes place in quasi-equilibrium and thus not in a real equilibrium. If we make the assumption that the coherence of the condensate is limited by the magnon lifetime, $\tau_{\mathrm{spin-latt}}$, then an estimate for the width in frequency can be made by $\Delta f_{\mathrm{condensate}} = 1/2\pi\tau_{\mathrm{spin-latt}}$. With this estimation we find a width of roughly 0.6 MHz.

The degree of coherence of the magnon-BEC has been studied before with Brillouin light scattering [4] and with microwave spectroscopy [25]. With those two techniques a width of respectively 50 MHz and 6 MHz was determined. However in the former case the width was equal to the experimental resolution and in the latter case the width was determined in an indirect way where an additional loss channel was present. Both values are also significantly above the expected value.

This chapter discusses the results of measurement of the frequency width of a BEC by using parametric pumping and femtosecond stroboscopic laser spectroscopy. We will employ the modulation of the amplitude of light caused by the magnons due to the Faraday effect to extract information about the magnon frequencies and coherence in the sample.

6.2 The idea: generation and detection of the condensate

This theory section is subdivided into two parts. The first part discusses the dispersion curve for magnons and how we excite them. The second part discusses how we measure the properties of the magnon gas with light.

6.2.1 Magnons: dispersion and excitation

Most of the relevant properties of magnons for this chapter are most easily explained by the magnon dispersion relation. Unfortunately for thin films the exact solution of the dispersion relation is a rather complex implicit function. However it can be shown that a good approximation can be obtained with perturbation theory and by applying the diagonal approximation. Although the dispersion relation is different for magnons with $k \parallel H_{\text{ext}}$ and $k \perp H_{\text{ext}}$ we will here only give the equation for magnons with $k \parallel H_{\text{ext}}$ as the dispersion relation for these magnons shows the global minimum energy of the system which is of most importance here. This dispersion relation reduces with the mentioned approximations to the explicit equation[26]

$$\omega^2 = \left(\omega_{\text{H}} + \omega_{\text{M}}\alpha k^2\right)\left(\omega_{\text{H}} + \omega_{\text{M}}\alpha k^2 + \omega_{\text{M}}\left[\frac{1-\mathrm{e}^{-|k|l}}{|k|l}\right]\right). \qquad (6.2)$$

In this equation ω is the angular frequency, k the wavenumber, α the exchange constant and l the sample thickness. ω_{H} and ω_{M} are respectively given by γH_{ext} and $\gamma 4\pi M_0$, where γ is the gyromagnetic ratio, M_0 the magnetization, and H_{ext} the external field. Evaluating this equation gives dispersion curves as shown in Fig. 6.1(a) for three different values of the external field. It is worth noting that the minimum frequency shifts vertically with the magnetic field by a factor equal to γ while the k-vector remains the same.

An efficient way to excite magnons in YIG is by using the process of parametric pumping [27]. In this process the sample is pumped at high power with a microwave pump at a frequency $2\omega_{\text{p}}$. One photon at $2\omega_{\text{p}}$ then creates two magnons at a frequency ω_{p} with opposite k-vectors, that will thus travel in opposite directions.

For the BEC to form we need a quasi-equilibrium, which means that there needs to be a thermal distribution over the available states. After we have excited magnons at ω_{p} these magnons will start to interact with each other and with the lattice and by doing so they will be distributed over the available states according to Eq. 6.1. If now the microwave power is high enough such that the loss of magnons is compensated by the creation of magnons, the necessary quasi-equilibrium will be formed.

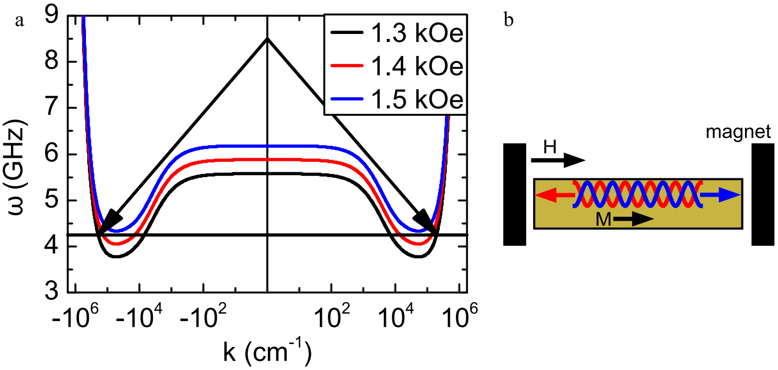

Figure 6.1: (a)The dispersion curve for magnons as given by Eq. 6.2 using $\alpha = 3 \cdot 10^{-12}$, $4\pi M_0 = 1750$ Oe, $l = 5.1$ μm and three different values for H_{ext} as indicated in the legend. With these parameters the minimum frequency can be found at $k = 5.4 \cdot 10^4$ cm^{-1}. The two black arrows show the process of parametric pumping where a photon at 8.5 GHz creates two magnons at 4.25 GHz there were the horizontal black line and the magnon dispersion cross.(b) Schematic sketch of the formation of a magnon standing wave pattern in a sample.

At the same time, with increasing microwave power, the chemical potential will increase due to the growing magnon density. At a critical particle density this chemical potential will equal the lowest energy state given by the minimum in the dispersion relation, Eq. 6.2. At that moment a Magnon Bose Einstein condensate (BEC) will be created.

6.2.2 The interaction between magnons and light

Due to the symmetry of the dispersion curve, magnons with the same frequency can travel in opposite directions. This causes a magnon standing wave pattern to be formed. This is schematically shown in Fig. 6.1(b). If enough magnons contribute to a coherent precession, it is possible to measure properties of these magnons with light using the Faraday effect.

For the light that interacts with the magnons, this standing wave pattern is effectively a grating, and thus the light will be reflected under an angle θ determined by the k-vector of the magnons k_{magnon} (periodicity of the grating), and the wavelength of the light λ_{light}

$$\sin\theta = \frac{k_{\text{magnon}}\lambda_{\text{light}}}{2\pi}. \tag{6.3}$$

The amplitude of the out of plane component of the magnetization will oscillate at the magnon frequency. This causes the intensity of the scattered light to oscillate at the same frequency as well.

To extract information about the frequency of the magnons we can in principle measure the light intensity and perform a Fourier transform of the signal. Here however we make use of a femtosecond pulsed laser at a high repetition rate. The amplitude of the individual magnetically scattered light pulses will now be modulated by the GHz magnon precession and in the Fourier transform the magnon signal will appear in side lobes of the laser pulse repetition frequency f_{rep}. For more details see Sect. 2.4.3.

To observe a clear peak in the frequency spectrum it is necessary that a large number of magnons precess coherently at the same frequency. In the quasi-thermal equilibrium this will not be the case, as multiple states with different frequencies and phases are occupied. However if condensation is achieved this condition is fulfilled. The width of the signal will now be a measure for the spectral width of the condensate. Notice that also at exactly half the pumping frequency where the parametrically generated magnons are injected, a coherent precession can be expected.

6.3 Sample and experimental setup

The sample is a 5.1 μm thick YIG film on a gadolinium gallium garnet substrate. On top of this sample a thin gold wire of 25 μm is placed which is connected to a microwave generator (Anritsu MG3692C). The gold wire will act as a microwave cavity such that a high intensity of microwaves can be applied to the sample. This high intensity of microwaves will then initiate the process of parametric pumping and be the source of magnons.

Permanent magnets on a translation stage supply a variable in-plane external magnetic field. The use of permanent magnets generates a more stable magnetic field than would be the case with an electromagnet. A stable and uniform magnetic field is necessary as the lowest energy state depends on the external magnetic field. According to Eq. (6.2) variations in the magnetic field will shift the frequency of the minimum of the dispersion curve and thus decrease the coherence of the condensate. An estimate of the field inhomogeneity can be given by measuring the change in field when the magnets are moved. We measured a change of approximately 75 mOe/μm.

To measure the coherence of the condensate we use a Spectra Physics Tsunami Ti:Sapphire laser with a repetition rate of about 80 MHz and a pulse duration of the order of 100 fs. A stable repetition rate is required as large variations in this rate will limit the frequency resolution. The highest stability for the repetition rate is achieved by using the active mode locking option of the laser. Using this option the change in the repetition rate was below 100 Hz. The wavelength is set to 990 nm. Afterwards, using a barium borate (BBO) crystal we half this to 495 nm. For YIG this wavelength is a trade-off between higher magneto-optic interaction at lower wavelengths and higher transmission at higher wavelengths.

The 495 nm light is horizontally polarized and focused to a 5 to 10 μm spot on the sample. The intensity of the light is varied between 1 and 3 mW. After the sample the light passes through a second polarizer and is coupled into an optical fiber. The optical components behind the sample are mounted on a rotation arm such that scattered light can be detected. The polarization axis of the second polarizer was set to a position between fully crossed and 45 deg uncrossed to optimize the detected signal. A Fourier transform is performed on the measured signal by an HP 8560A

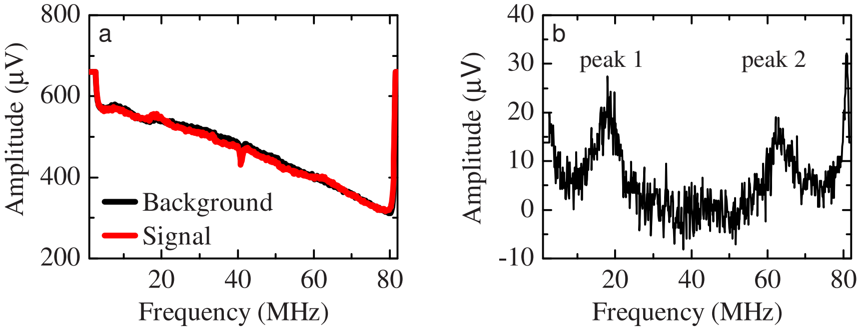

Figure 6.2: (a) Two typical curves obtained from the spectrum analyzer. One where the microwave generator is turned on and one where it was turned off. In (b) the background curve is first scaled and then subtracted from the signal curve.

Portable Spectrum Analyzer after the light was detected by an avalanche photodiode (APD). More details about the setup can be found in Sect. 2.4.3.

Two typical signals we get from the spectrum analyzer are shown in Fig. 6.2(a). The red curve is obtained with the microwave signal on, while the black curve is recorded with the microwave generator off and thus is a background curve. As it is clear from those curves the spectrum analyzer itself introduces some spectral features as well, such as for example the dip in the middle. The peak on the right side (above 80 MHz) is at f_{rep} and the peak on the left is the dc signal. To get a more clear picture of the signal that we are interested in, we recorded the background signal such that the average detected light intensity is still of the same order of magnitude. Then we perform the following operation:

$$S_{\text{norm}} = S - \text{avg}[S/S_{\text{Background}}]S_{\text{Background}}. \tag{6.4}$$

Here S and $S_{\text{Background}}$ are the measured signals, and the average (avg) is only performed on a flat area with no spectral features. The signal obtained with the above procedure is shown in Fig. 6.2(b).

The curves in Fig. 6.2(a) are obtained after a certain amount of averaging. In general we took between 16 and 64 averages for the data shown in this chapter. The maximum amplitude that can be measured with the spectrum analyzer depends on the resolution settings. This explains the cutoff of the peaks on the left and right of Fig. 6.2(a) at 650 μV.

For most measurements the observed peaks were fitted with a Lorentzian curve,

$$y = y_0 + \frac{2A}{\pi}\frac{w}{4(x-x_0)^2 + w^2}. \tag{6.5}$$

Here y_0 is the offset, A the area w the Full Width at Half Maximum (FWHM) and x_0 the center frequency. The peak height can be obtained with $2A/\pi w$. As in all the measurements two peaks are present: the left peak will be called peak 1 and the right

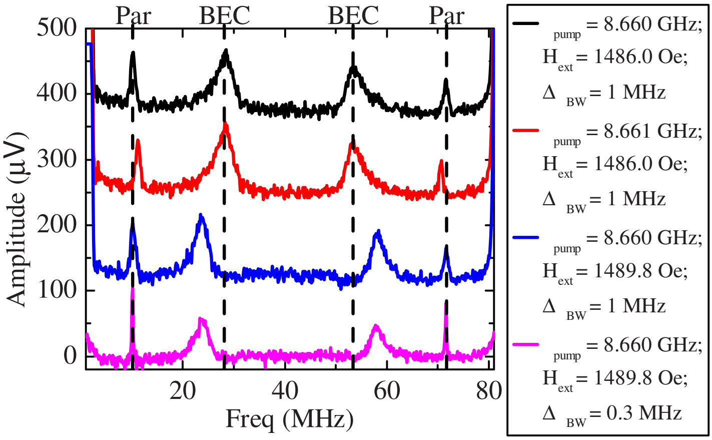

Figure 6.3: Frequency spectra of the light that is collected at an angle of 24 deg ($k = 5.2 \cdot 10^4$ cm^{-1}). By small adjustments of the parameters given in the legend, we can distinguish the Bose-Einstein peak (indicated with 'BEC') from the parametric magnon peak (indicated with 'Par').

peak will be called peak 2. Measurement points where the condensate peaks overlap each other or the peak at the laser repetition frequency are in general not included in graphs with fitting parameters as the obtained parameters are not reliable.

6.4 Results and discussion

This section will be divided into two subsections. These subsections will discuss two different data sets that used different pumping frequencies. The first subsection will discuss data obtained at $2\omega_\mathrm{p} = 8.66$ GHz and will be more extensive to demonstrate that the peak we observe is indeed from the BEC. The second subsection shows data obtained at $2\omega_\mathrm{p} = 9.94$ GHz. The focus of this section will be on the subtle differences between the two datasets because from the theory we did not expect large differences to be present.

6.4.1 Pumping with 8.66 GHz

Experimentally we obtained the largest signal from the BEC when the parametrically generated magnons are excited with a k-vector close to the minimum frequency as given by the dispersion diagram. In this condition light scattering from the standing wave at the parametric frequency and from the standing wave at the BEC frequency occurs at almost the same angle.

This made it possible to observe both peaks in a single measurement. In Fig. 6.3 a series of such measurements is shown where we can clearly observe the different behavior of the peaks. If we change the microwave pumping frequency only the narrowest of the two peaks is shifting while if we change the field only the broader peak is shifting. From this behavior it is clear that the narrow peak is from parametric magnons while we assign the broader one to the condensate. The bottom curve is measured at a lower frequency bandwidth of the spectrum analyzer, Δf_{BW}, and shows that although the parametric peak becomes narrower, the width of the BEC peaks remains almost unchanged. This measurement thus demonstrates that the frequency resolution of the experimental method is high enough to determine the width of the condensate.

The next measurement we performed was a field dependence from which the raw data are shown in Fig. 6.4(a) as a 2D intensity plot. From this figure it is clear that the BEC peak shifts with field as we expect it to do. To perform a more detailed analysis, every peak was fitted with Eq. (6.5) and the center frequency was projected in such a manner that all points form a single line as is shown in Fig. 6.4(b). The slope of this line is found to be 2.52±0.01 MHz/Oe for peak 1 and 2.50±0.01 MHz/Oe for peak 2. As explained in the theory for the BEC this increase in frequency should be equal to $\gamma/2\pi$=2.8 MHz/Oe. The reason for the deviation from this value is unclear. As we will see later on at a different pumping frequency we obtained a better match.

In Fig. 6.4(c) the amplitude of the peak versus field is shown. A sudden increase in the amplitude can be observed in the field range between 1480 and 1500 Oe. In this region the parametric magnons are pumped directly into the bottom of the magnon dispersion. The FWHM of the condensate reaches its minimum as well in this field range as is shown in Fig. 6.4(d). The observed width varies with field but the minimum width is almost 2 MHz. This is already three times narrower as observed before [25].

At a field close to where a maximum amplitude is observed, 1489 Oe, we performed a microwave pump power dependence as well. The resulting data is shown in Fig. 6.5(a)-(c). The small peak that is visible in some of the curves is from the parametric magnons. In this figure a clear asymmetry is visible in the BEC peak. For the peak at 20 MHz the higher frequency side is much steeper than the lower frequency side. We can explain this by looking back at the field dependence in Fig. 6.4(a) and the dispersion curve in Fig. 6.1(a). From the field dependence we know that the peak is moving to lower frequencies with increasing field. According to the dispersion curve this means that the bottom of the dispersion is at the right hand side of this peak. Hence the steeper side of the peak indicates the bottom of the dispersion curve. At this side there are no other states available. At the left side of the peak there are states available and thus magnons can exist.

Although a Lorentzian is not describing the shape of these peaks correctly, we still used Eq. 6.5 for fitting the data as we had too many data to perform a manual determination of the parameters of interest. A few manual checks and the reasonable error bar resulting from the fitting confirms that a Lorentzian fit does still give reliable values for the FWHM, center frequency position and peak height (see also Fig. 6.5(a)-(b) and Fig 6.7(a)-(b)).

In Fig. 6.5(d) to (f) we can identify roughly three ranges in which the signal has a different dependence on the pumping power. These three ranges are below 18 dBm, between 18 and 21 dBm and above 21 dBm. In the first range the number of

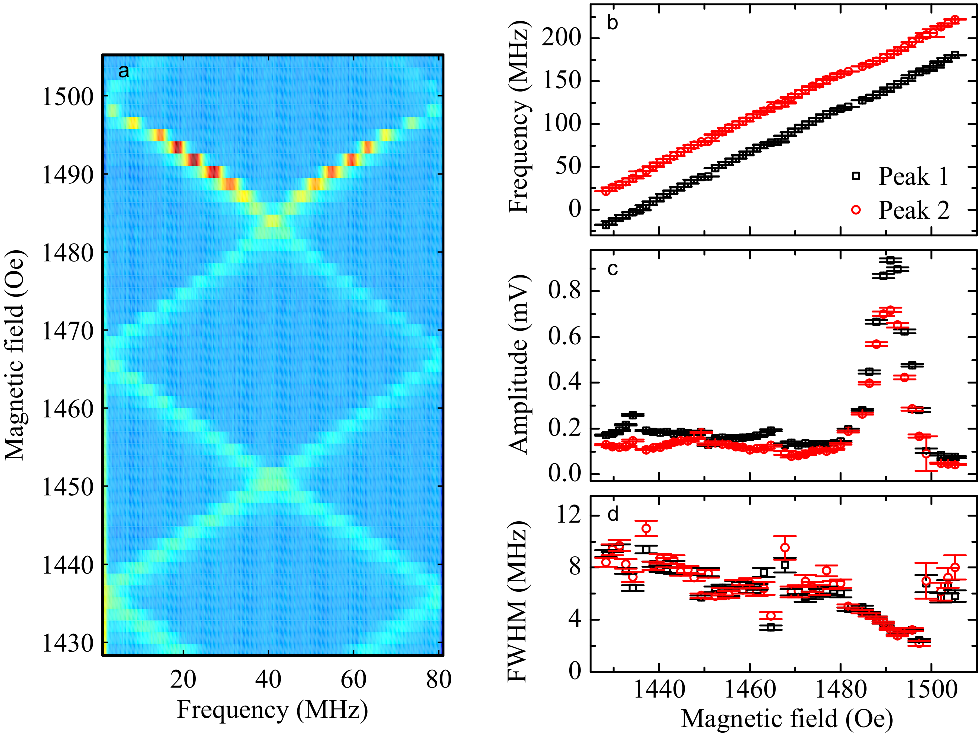

Figure 6.4: Field dependence of the BEC peak. In (a) the raw data is shown. In (b) the peak position is plotted as a function of magnetic field. The slope is found to be 2.52±0.01 MHz/Oe for peak 1 and 2.50±0.01 MHz/Oe for peak 2. (c) shows the amplitude of the peak and in (d) the FWHM versus field is plotted. The measurements are performed at $2\omega_\mathrm{p} = 8.66$ GHz, 20 dBm, a collection angle of 24 deg ($k = 5.2 \cdot 10^4$ cm^{-1}) and $\Delta f_\mathrm{BW} = 1$ MHz.

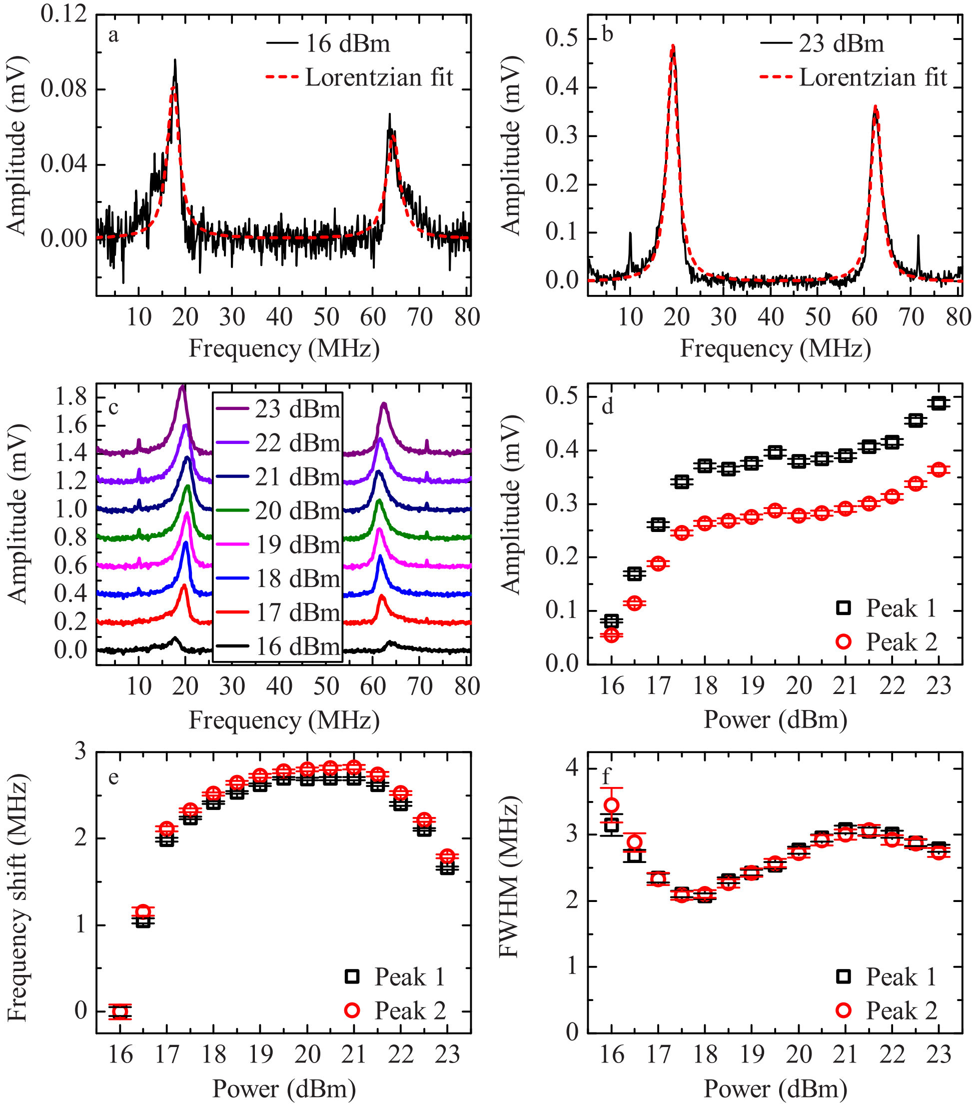

Figure 6.5: Dependence of the BEC peak on the pumping power. In (a) and (b) the raw data of a single power is shown together with a Lorentzian fit to the data. A set of raw data measured at different pumping power is shown in (c). At higher powers a small peak from the parametric pumped magnons is visible as well. In (d) the peak amplitude versus power is shown. In (e) the absolute shift of the peak position with power is shown. The FWHM versus power is shown in (f). The measurements are performed at $2\omega_{\mathrm{p}} = 8.66$ GHz, 1489 Oe, a collection angle of 24 deg ($k = 5.2 \cdot 10^4$ cm^{-1}) and $\Delta f_{\mathrm{BW}} = 300$ kHz.

magnons in the BEC state is increasing and thus the signal amplitude is increasing. In Fig. 6.5(e) we observe in this range also a clear shift of the center frequency with increasing pumping power. This shift can be explained by a decrease in the static magnetization due to an increase in the oscillation amplitude. According to Eq. (6.2) this will decrease the minimum frequency. The FWHM is decreasing in this region as the contribution from non-condensate states is decreasing. A minimum of 2 MHz is reached at 18 dBm. This measurement is performed with $\Delta f_{\mathrm{BW}} = 300$ kHz compared to the measurements shown in Fig. 6.4 which where performed with $\Delta f_{\mathrm{BW}} = 1$ MHz. Hence the observed 2 MHz is not limited by the bandwidth of the spectrum analyzer.

In the second range from 18 to 21 dBm the amplitude is constant. It is known that the parametric pumping at higher powers will become less efficient due to a reaction of the parametric spin waves on the pumping [27]. This seems to be the case here. As the amplitude of the oscillations is not increasing anymore the minimum frequency is stable as well. The FWHM is slightly increasing in this range.

Above 21 dBm the amplitude suddenly starts to increase again and the minimum frequency starts to increase as well while the FWHM is decreasing. At the moment it is still unclear what is the origin of this behaviour.

6.4.2 Pumping with 9.94 GHz

If we keep the field range similar to the previous dataset while changing the pumping frequency, we change the position in the dispersion diagram where the magnons are excited by the parametric pumping process. In this subsection we will discuss the differences that we observe between a dataset measured at 9.94 GHz and the previous dataset.

Again in Fig. 6.6 the field dependences are shown, in particular in (a) the raw data, in (b) the peak position, (c) the peak amplitude and in (d) the FWHM as a function of field. The slopes resulting from fits to the data points in Fig. 6.6(b) are both 2.77±0.01 MHz/Oe. That is, these are much closer to the expected value for $\gamma/2\pi$ as compared to the previous data set.

The amplitude of the signal, shown in Fig. 6.6(c), is much lower compared to the previous dataset. For this difference we can give two reasons. The first is that the intensity of the laser was in this case 2.5 times smaller. The second reason is that with this pumping frequency and fields we are much further away from the bottom of the dispersion curve. It should be noted however that if we increased the external field to a level where we should be pumping into the minimum directly, we did not observe an increase in the signal either. Two maxima can still be observed in Fig. 6.6(c). Again the maxima occur at positions where the FWHM reaches a minimum (Fig. 6.6(d)). The global minimum in FWHM is equal to the minimum width observed in the other data set, 2 MHz.

Fig. 6.7(a)-(c) shows the raw data of a power dependence at a field close to the maximum amplitude in Fig 6.6(c). The peak amplitude can be found in Fig. 6.7(d). Instead of showing saturation, the amplitude directly decreases after reaching a maximum. In the measured power range the frequency shift is only increasing and is smaller compared to the previous dataset. Both phenomena, the smaller frequency

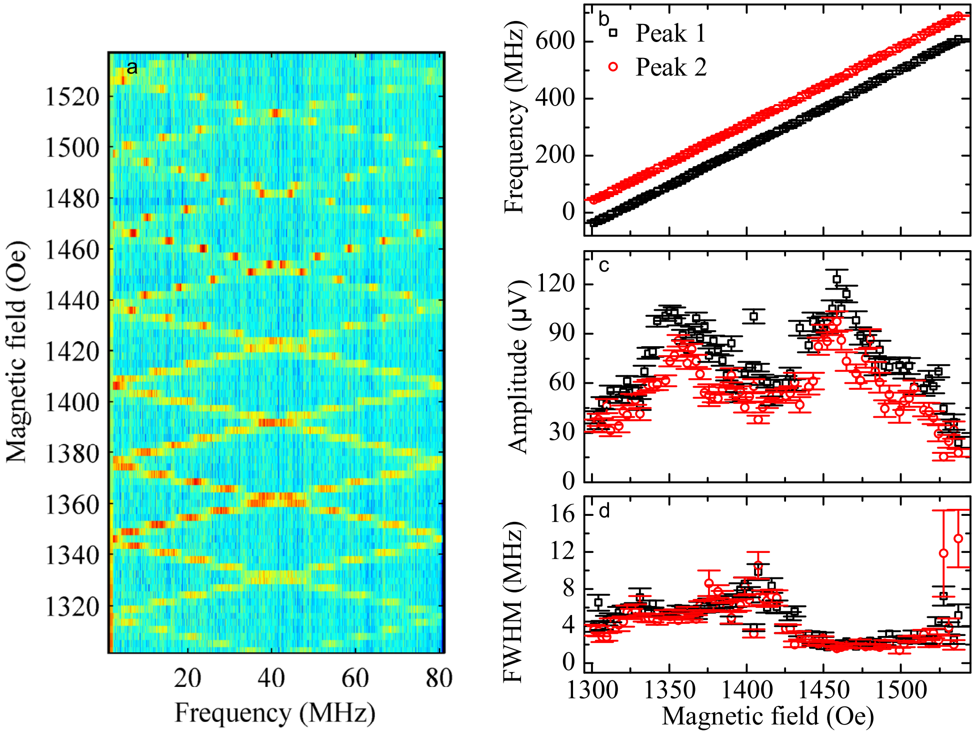

Figure 6.6: Field dependence of the BEC peak. In (a) the raw data is shown. In (b) The peak position plotted as a function of magnetic field. The slope is found to be 2.77±0.01 MHz/Oe for both peaks. (c) shows the amplitude of the peak and in (d) the FWHM versus field is plotted. The measurements are performed at $2\omega_\mathrm{p} = 9.94$ GHz, 21 dBm, a collection angle of 23 deg ($k = 5.0 \cdot 10^4$ cm^{-1}) and $\Delta f_\mathrm{BW} = 1$ MHz.

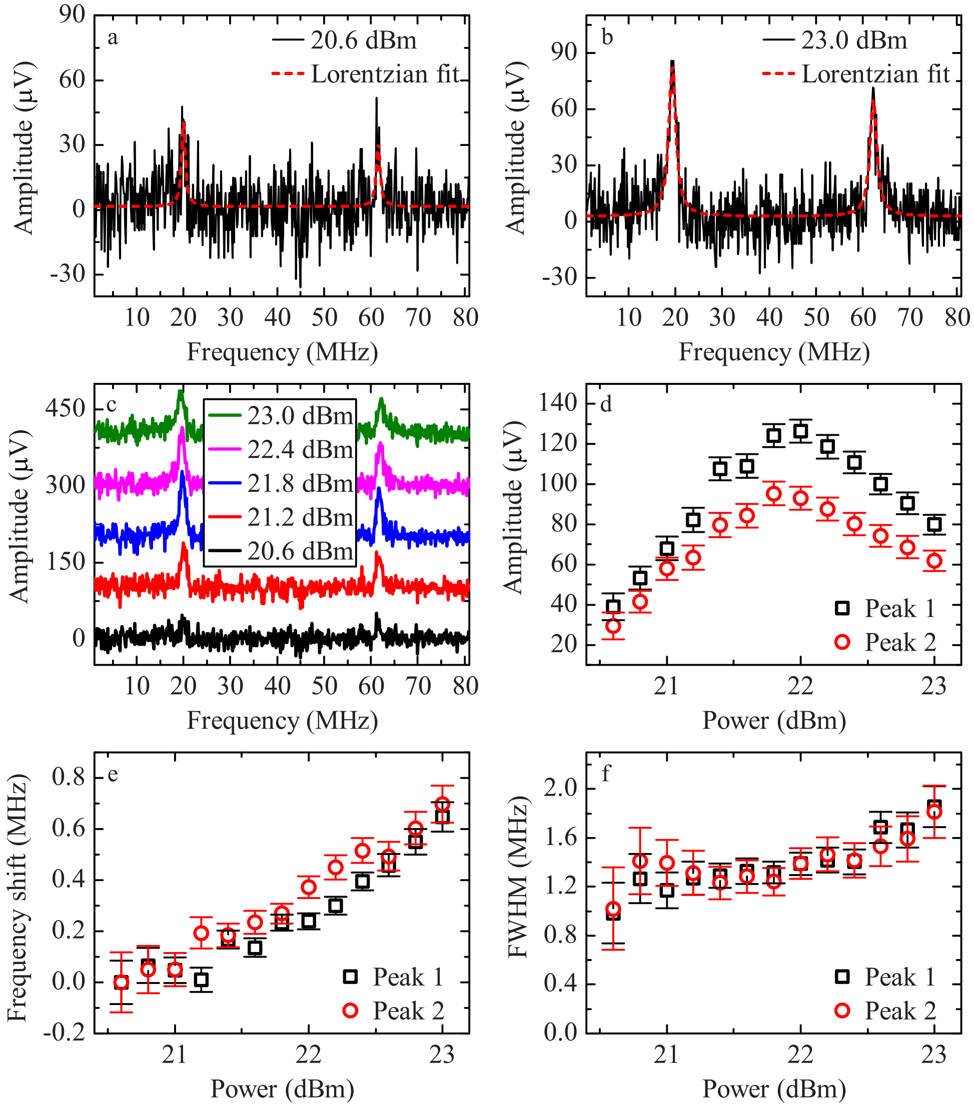

Figure 6.7: Dependence of the BEC peak on the pumping power. In (a) and (b) the raw data of a single power is shown together with a Lorentzian fit to the data. A set of raw data measured at different pumping power is shown in (c). In (d) the peak amplitude versus power is shown. (e) shows that the peak position is shifting with power. The FWHM versus power is shown in (f). The measurements are performed at $2\omega_\mathrm{p} = 9.94$ GHz, 1455 Oe, a collection angle of 23 deg $k = 5.0 \cdot 10^4\ \mathrm{cm}^{-1}$) and $\Delta f_\mathrm{BW} = 300$ kHz.

shift and the absence of saturation in the peak amplitude might be related to the lower efficiency of the parametric pumping process at this frequency.

In Fig. 6.7(f) we see that again the minimum in FWHM is obtained when the amplitude is at a maximum. Most interestingly this data set shows an even more narrow line width of the condensate of 1.2 MHz. This is only twice as big as the minimum theoretically expected width. Again $\Delta f_{\mathrm{BW}} = 300$ kHz, thus the measurement is not limited by the resolution of the spectrum analyzer.

Although we measure a frequency width that is much closer to the theoretically expected width, a difference of a factor two is still present. Furthermore significant differences are observed between the two presented datasets while theoretically we did not expect those differences. This might mean that we do not have yet a full control over the experimental parameters or that we do not understand the theory enough. Experimentally the homogeneity of the magnetic field in combination with a too large spot size might not have been enough. If we multiply the field homogeneity of 75 mOe/μm with the maximum expected spot size of 10 μm and multiply this with $\gamma/2\pi$ we obtain a value that gives an estimation of the frequency resolution. The obtained value is 2.1 MHz, hence this is broader than the minimum width that we observed. This value could be improved by the use of a better objective to decrease the spot size or the use of larger and stronger magnets. With a more tight focusing the signal might become smaller if it is necessary to decrease the laser power to prevent sample damage.

6.5 Conclusion

In conclusion, we have studied the degree of coherence of the magnon Bose-Einstein condensation in an yttrium iron garnet film. For this study a microwave continuous wave pump - optical femtosecond pulsed probe scheme was used. For the study of magnon Bose-Einstein condensation the use of this method is a novelty.

For the excitation of magnons the known process of parametric pumping is used. However we combined this with a stroboscopic probing of the Faraday effect from the magnon precession. As the magnon related to the Bose-Einstein condensate has a non zero k-vector, the signal had to be collected at an angle of roughly 24 degree from the sample normal. By performing a frequency analysis of the detected optical signal, the width in frequency of the condensate precession is measured with a high frequency resolution. This width in frequency is a direct measure for the coherence of the condensate.

With this new method the minimum observed width of the condensate is 1.2 MHz. This is only by a factor of two different from the theoretically expected value. The field inhomogeneity in combination with the optical spot size might limit the frequency resolution.

The minimum width and thus the coherence of the condensate is found to depend on both the external applied field and the pumping power. When the amplitude of the signal from the condensate is largest the width of the condensate is observed to be minimal.

References

[1] A. P. Malozemoff, J. C. Slonczewski, and R. Wolfe, *Magnetic Domain Walls in Bubble Materials* (Elsevier Inc., 1979).

[2] Y. Kajiwara, K. Harii, S. Takahashi, J. Ohe, K. Uchida, M. Mizuguchi, H. Umezawa, H. Kawai, K. Ando, K. Takanashi, S. Maekawa, and E. Saitoh, "Transmission of electrical signals by spin-wave interconversion in a magnetic insulator," Nature **464**, 262 (2010).

[3] K. Uchida, J. Xiao, H. Adachi, J. Ohe, S. Takahashi, J. Ieda, T. Ota, Y. Kajiwara, H. Umezawa, H. Kawai, G. E. W. Bauer, S. Maekawa, and E. Saitoh, "Spin seebeck insulator," Nat Mater **9**, 894 (2010).

[4] S. O. Demokritov, V. E. Demidov, O. Dzyapko, G. A. Melkov, A. A. Serga, B. Hillebrands, and A. N. Slavin, "Bose-Einstein condensation of quasi-equilibrium magnons at room temperature under pumping," Nature **443**, 430 (2006).

[5] M. H. Anderson, J. R. Ensher, M. R. Matthews, C. E. Wieman, and E. A. Cornell, "Observation of Bose-Einstein condensation in a dilute atomic vapor," Science **269**, 198 (1995).

[6] K. B. Davis, M. O. Mewes, M. R. Andrews, N. J. van Druten, D. S. Durfee, D. M. Kurn, and W. Ketterle, "Bose-Einstein condensation in a gas of sodium atoms," Phys. Rev. Lett. **75**, 3969 (1995).

[7] S. N. Bose, "Plancks gesetz und lichtquantenhypothese," Z. Phys. **26**, 178 (1924).

[8] A. Einstein, "Quantentheorie des einatomigen idealen gases. part I," Sber. Preuss. Akad. Wiss. **22**, 261 (1924).

[9] L. V. Butov, "Condensation and pattern formation in cold exciton gases in coupled quantum wells," Journal of Physics: Condensed Matter **16**, R1577 (2004).

[10] Y. Yamamoto, "Semiconductor physics: Half-matter, half-light amplifier," Nature **405**, 629 (2000).

[11] M. Saba, C. Ciuti, J. Bloch, V. Thierry-Mieg, R. Andre, L. S. Dang, S. Kundermann, A. Mura, G. Bongiovanni, J. L. Staehli, and B. Deveaud, "High-temperature ultrafast polariton parametric amplification in semiconductor microcavities," Nature **414**, 731 (2001).

[12] D. Snoke, "Spontaneous Bose coherence of excitons and polaritons," Science **298**, 1368 (2002).

[13] I. Carusotto and C. Ciuti, "Probing microcavity polariton superfluidity through resonant rayleigh scattering," Phys. Rev. Lett. **93**, 166401 (2004).

[14] J. Kasprzak, M. Richard, S. Kundermann, A. Baas, P. Jeambrun, J. M. J. Keeling, F. M. Marchetti, M. H. Szymanska, R. Andre, J. L. Staehli, V. Savona, P. B. Littlewood, B. Deveaud, and L. S. Dang, "Bose-Einstein condensation of exciton polaritons," Nature **443**, 409 (2006).

[15] M. Matsumoto, B. Normand, T. M. Rice, and M. Sigrist, "Magnon dispersion in the field-induced magnetically ordered phase of $TlCuCl_3$," Phys. Rev. Lett. **89**, 077203 (2002).

[16] C. Ruegg, N. Cavadini, A. Furrer, H.-U. Gudel, K. Kramer, H. Mutka, A. Wildes, K. Habicht, and P. Vorderwisch, "Bose-Einstein condensation of the triplet states in the magnetic insulator $TlCuCl_3$," Nature **423**, 62 (2003).

[17] T. Giamarchi, C. Ruegg, and O. Tchernyshyov, "Bose-Einstein condensation in magnetic insulators," Nat. Phys. **4**, 198 (2008).

[18] V. E. Demidov, O. Dzyapko, S. O. Demokritov, G. A. Melkov, and A. N. Slavin, "Thermalization of a parametrically driven magnon gas leading to Bose-Einstein condensation," Phys. Rev. Lett. **99**, 037205 (2007).

[19] V. E. Demidov, O. Dzyapko, S. O. Demokritov, G. A. Melkov, and A. N. Slavin, "Observation of spontaneous coherence in Bose-Einstein condensate of magnons," Phys. Rev. Lett. **100**, 047205 (2008).

[20] V. E. Demidov, O. Dzyapko, M. Buchmeier, T. Stockhoff, G. Schmitz, G. A. Melkov, and S. O. Demokritov, "Magnon kinetics and Bose-Einstein condensation studied in phase space," Phys. Rev. Lett. **101**, 257201 (2008).

[21] A. V. Chumak, G. A. Melkov, V. E. Demidov, O. Dzyapko, V. L. Safonov, and S. O. Demokritov, "Bose-Einstein condensation of magnons under incoherent pumping," Phys. Rev. Lett. **102**, 187205 (2009).

[22] J. D. Plumhof, T. Stöferle, L. Mai, U. Scherf, and R. F. Mahrt, "Room-temperature Bose-Einstein condensation of cavity exciton-polaritons in a polymer," Nat. Mater. **13**, 247 (2014).

[23] Nobelprize.org, "The 2001 nobel prize in physics - advanced information," (2001), http://www.nobelprize.org/nobel_prizes/physics/laureates/2001 /advanced.html.

[24] O. Dzyapko, V. E. Demidov, S. O. Demokritov, G. A. Melkov, and A. N. Slavin, "Direct observation of Bose-Einstein condensation in a parametrically driven gas of magnons," New Journal of Physics **9**, 64 (2007).

[25] O. Dzyapko, V. E. Demidov, S. O. Demokritov, G. A. Melkov, and V. L. Safonov, "Monochromatic microwave radiation from the system of strongly excited magnons," Appl. Phys. Lett. **92**, 162510 (2008).

[26] B. Kalinikos, "Excitation of propagating spin waves in ferromagnetic films," Microwaves, Optics and Antennas, IEE Proceedings H **127**, 4 (1980).

[27] A. G. Gurevich and G. A. Melkov, *Magnetization Oscillations and Waves* (CRC Press, 1996).

Summary

In the current society information technology plays an important role. To store data we rely mostly on magnetic data storage especially inside data centers. With the increasing number of those data centers they are responsible for an increasing fraction of the yearly energy consumption. To increase the energy efficiency as well as the write/read speed and data density of existing magnetic storage techniques or to find alternative magnetic storage techniques it is important to increase the understanding of the fundamental physics involved in the storage process, which is magnetization dynamics.

In this thesis we are mainly interested in how the magnetization dynamics can be excited and controlled with light. Therefore, in Chapter 1, after an overview of different magnetic data storage techniques, the current knowledge of the different mechanisms of the optical excitation of magnetization dynamics is discussed. More specifically we distinguish between photo-magnetic and opto-magnetic effects as well as we discuss demagnetization in metals and all optical switching.

In Chapter 2 an overview is given of the computational and experimental techniques that are used throughout this thesis. All experimental techniques are based on a pump-probe scheme, but the information they can extract from the sample of interest differs. While one of them, an X-ray holography setup, gives static spatial information of the magnetic domain structure, the other two, an optical pump-probe and a femtosecond stroboscopic laser spectroscopy setup, measure magnetization dynamics in respectively the time or frequency domain.

In Chapter 3 it is shown that to use plasmonic nano antennas for all optical switching, interference effects have to be taken into account if a spacing layer is present between the antenna and the region of interest where we want to profit from the field enhancement and confinement from the plasmonic structure. Those interference effects make an off-resonant antenna to perform better than a resonant one. A FWHM light spot of 41 nm is obtained in a magnetic thin film separated by a 10 nm capping layer from an antenna structure with light with a wavelength of 800 nm.

Furthermore we have shown antenna induced switching experimentally with X-ray holographic imaging. The smallest observed domains have a diameter below 50 nm. However, no full control over the switching location has been obtained. While switching was expected to occur in the antenna gap, we did observe switching under the antenna arm more often. More research is necessary to explain the location of the observed switching. A more detailed fluence dependence or a mapping of the inhomogeneity in the distribution of Fe and Gd in the investigated magnetic material could reveal more information.

In Chapter 4 and 5 we have investigated the magnetization dynamics in bismuth iron garnet. More specific, in Chapter 4 the field and polarization dependence is studied in detail resulting in the observation of a new excitation mechanism which most likely is an impulsive photo-magnetic effect that is non-thermal and polarization independent. We were able to distinguish the observed non-thermal effect from a thermal effect by its oscillation amplitude dependence on the external field. The anisotropy and the Gilbert damping was studied as well. A simple model assuming a spread in the anisotropy is shown to describe the decrease of the apparent Gilbert damping with increasing field very well.

In Chapter 5 the spectral dependence of the magnetization dynamics in bismuth iron garnet is studied with the aim to have an independent sensitivity to the magnetization originating from the two different iron sites. We find a light induced modification of the magneto-optical constants. It is shown that the relative contributions from the two different iron sites change after the pump pulse has hit the sample. With the change in the magneto-optical constants we can explain the non-linear dependence of the amplitude of the oscillations on the fluence. These oscillations are excited by the inverse Faraday effect and thus in principle expected to depend linearly on the light intensity.

In the last chapter we investigate how the excited magnetic system evolves. In particular, the formation of a coherent Bose-Einstein condensate of magnons is studied. The degree of coherence was measured as the spectral width of the condensate. An additional complication was that the light scattered from the magnons propagated from the sample at an angle determined by the magnon k-vector. The minimal spectral width found was 1.2 MHz while 0.6 MHz was theoretically predicted. It might be that the homogeneity of the magnetic field limits the observed width. A more uniform magnetic field over the spot size of the probing laser spot might increase the observed coherence of the condensate even further.

This summary started with the statement that understanding magnetization dynamics could lead to an improvement in magnetic data storage. While the subjects treated in Chapter 4 to 6 have a more fundamental character, the relevance of the work in Chapter 3 towards realizing an energy efficient, fast and high density data recording device is more direct. Until now it was not yet demonstrated that all optical switching, which has the potential to become a more energy efficient and faster data storage technique as compared to switching with a magnetic field, could be realized with a writing density that can be compared to the commercial hard drives of today. The use of the antenna structure makes the all optical switching even more energy efficient by local field enhancement and the reduction of the area where switching takes place.

However this does not mean that all optical switching is now ready to be commercialized. First of all as also shown in this thesis more control over the switching process is necessary. Furthermore an antenna structure placed directly on the magnetic material is not the most convenient and still does not offer the possibility of high density recording. For the high density recording it would be necessary that the antenna structure is mounted on a tip that can move over the recording disk. As this is basically already what happens in the prototypes of heat or thermally assisted magnetic recording, this is not expected to be the biggest challenge.

From the more fundamental side it is still interesting to do more research on the possibility to independently pump or probe the two different iron sites in bismuth iron garnet by selecting the right optical probe wavelength as suggested in Chapter 5. In this thesis we did not observe any difference in the dynamics, this is clearly due to the fact that a single ferromagnetic mode was excited. Alternatively, one could attempt pumping the energy into a single sublattice, by using the inverse Faraday effect at the proper wavelength, and thus observe the interaction between the sublattices. Moreover, if it could indeed be shown that sensitivity could be obtained to the individual iron sites by the choice of the probe wavelength then this would give an advantage of optical pump-probe compared to X-ray techniques. While with X-rays it is only possible to distinguish between different elements, the measurement suggested here would be able to distinguish between the same element in a different crystal lattice environment.

Samenvatting

In de hedendaagse maatschappij speelt informatie technologie een belangrijke rol. Om gegevens op te slaan gebruiken we met name magnetische data opslag en dit gebeurt dan vooral in datacenters. Met de groei aan datacenters nemen deze een steeds groter deel van de jaarlijkse energie consumptie voor hun rekening. Het is van belang om onze kennis van de fundamentele natuurkunde gerelateerd aan de opslag processen uit te breiden om de energie efficiëntie als ook de schrijf/lees snelheid en de gegevensdichtheid van bestaande magnetische data opslag technieken te vergroten. Met meer fundamentele kennis zouden ook eventuele alternatieve magnetische data opslag technieken gevonden kunnen worden. Het belangrijkste natuurkundige proces in het opslag proces is de magnetizatie dynamica.

In dit proefschrift zijn we met name geïnteresseerd in hoe de magnetizatie dynamica kan worden aangeslagen en gecontroleerd met licht. In Hoofdstuk 1 wordt daarvoor een overzicht gegeven van de verschillende bestaande magnetische data opslag technieken als ook een overzicht van de al beschikbare kennis over de verschillende manieren waarop met licht magnetizatie dynamica aangeslagen kan worden. Meer specifiek maken we een onderscheid tussen foto-magnetische en opto-magnetische effecten. Daarnaast behandelen we ook demagnetizatie in metalen en volledig optisch schakelen.

In Hoofdstuk 2 wordt een overzicht gegeven van de computationele en experimentele technieken die in dit proefschrift zijn gebruikt. Alle experimentele technieken zijn gebaseerd op een pomp-sonde schema maar de informatie die met de technieken verkregen kan worden verschilt. Terwijl een van de technieken, een Röntgen stralen holografie opstelling, statische informatie over de magnetische domeinen geeft, kan er met de andere twee, een optische pomp-sonde en een femtoseconde stroboscopische laser spectroscopie opstelling, magnetizatie dynamica gemeten worden in respectievelijk het tijds- en frequentie domein.

In Hoofdstuk 3 laten we zien dat het belangrijk is om interferentie effecten in beschouwing te nemen als plasmonische nano antennes gebruikt worden voor volledig optisch schakelen en er een separatie laag aanwezig is tussen de antenne en de regio waar we willen profiteren van de veld versterking en localizatie veroorzaakt door de plasmonische structuur. De interferentie effecten zorgen ervoor dat een niet resonante antenna beter werkt dan een resonante. Een halfwaardebreedte van 41 nm is verkregen voor de optische spot in de magnetische dunne film welke met een 10 nm protectie laag verwijderd is van de antenne. De golflengte van het gebruikte licht was 800 nm.

Daarnaast hebben we antenne geïnduceerd schakelen experimenteel laten zien met behulp van Röntgen holografie. De kleinst geobserveerde domeinen hebben een diameter kleiner dan 50 nm. Echter hebben we nog geen volledige controle over de locatie waar het schakelen optreed. Terwijl we schakelen in de antenna opening verwachtten, hebben we vaker schakelen geobserveerd onder de antenna arm. Meer onderzoek is nodig om de locatie van het schakelen te verklaren. Een meer gedetailleerde energie afhankelijkheid of het maken van een afbeelding van de inhomogeniteit in de distributie van de Fe en Gd elementen in het onderzochtte magnetische materiaal zouden meer informatie kunnen geven.

In Hoofdstuk 4 en 5 hebben we de magnetizatie dynamica in bismut ijzer granaat onderzocht. Meer specifiek hebben we in Hoofdstuk 4 de veld en polarizatie afhankelijkheid bestudeerd. Dit heeft geresulteerd in de observatie van een nieuw excitatie mechanisme. Dit excitatie mechanisme is hoogstwaarschijnlijk een impulsief fotomagnetisch effect dat niet-thermisch en polarizatie onafhankelijk is. We waren in staat om dit niet-thermische effect te onderscheiden van een thermisch effect door de relatie tussen de oscillatie amplitude en het extern aangelegde magnetische veld. De anisotropie en de Gilbert demping is ook bestudeerd. Een simpel model dat een spreiding in de anisotropie aanneemt, is in staat om de geobserveerde afname in de Gilbert demping met toenemend veld goed te beschrijven.

In Hoofdstuk 5 is de spectroscopische afhankelijkheid van de magnetizatie dynamica in bismut ijzer granaat bestudeerd met het doel om een onafhankelijke gevoeligheid te hebben voor de magnetizatie veroorzaakt door de twee verschillende ijzer locaties. Een licht geïnduceerde verandering in de magnetisch-optische constanten is gevonden. We laten zien dat de relatieve bijdrage van de twee verschillende ijzer locaties veranderd na het arriveren van de pomp puls. Met de verandering in de magnetisch-optische constanten kunnen we de niet lineare afhankelijkheid tussen de oscillatie amplitude en de puls energie dichtheid verklaren. De oscillaties zijn geëxciteerd door het omgekeerde Faraday effect en dus wordt er in principe een linear verband verwacht met de licht intensiteit.

In het laatste Hoofdstuk onderzoeken we hoe een geëxciteerd magnetisch systeem zich ontwikkeld. In het bijzonder kijken we naar de formatie van een coherent Bose-Einstein condensaat van magnonen. We hebben de mate van coherentie gemeten aan de hand van de spectrale breedte van het condensaat. Een extra complicatie hierbij was dat het licht door de interactie met de magnonen onder een hoek verstrooid werd. De hoek waaronder dit licht verstrooid werd, werd bepaald door de magnon k-vector. De kleinste spectrale breedte die gevonden is, is 1.2 MHz, terwijl theoretisch 0.6 MHz verwacht word. Het zou kunnen dat de homogeniteit van het magnetische veld de observeerbare breedte limiteerd. Een meer homogeen magnetisch veld in de licht spot zou de geobserveerde coherentie kunnen vergroten.

Deze samenvatting startte met de stelling dat het begrijpen van magnetizatie dynamica zou kunnen leiden tot een verbetering in magnetische data opslag. Alhoewel de onderwerpen behandeld in Hoofdstuk 4 tot en met 6 een meer fundamenteel karakter hebben, is het werk uit Hoofdstuk 3 meer direct relevant voor het realiseren van een energie efficiënt en snel data opslag apparaat met een hoge datadichtheid. Volledig optisch schakelen heeft de potentie om een meer energie efficiënt en snellere data opslag techniek te worden vergeleken met technieken gebaseerd op schakelen met een magnetisch veld. Tot nog toe was echter nog niet aangetoond dat volledig optisch schakelen kan worden gerealiseerd met een schrijfdichtheid vergelijkbaar met die van de op het moment verkrijgbare commerciële harde schijven. Het gebruik van de antenna structuur maakt het volledig optisch schakelen zelfs nog meer energie efficiënt door de veld versterking en een reductie van de te schakelen oppervlakte.

Dit betekend echter niet dat volledig optisch schakelen nu klaar is om te commercialiseren. Ten eerste, zoals ook getoont in dit proefschrift is er meer controle nodig over de locatie waar er geschakeld wordt. Daarnaast is het plaatsen van een antenne direct op het magnetische materiaal niet het handigst en bied nog steeds niet de mogelijkheid van een hoge datadichtheid. Voor het schrijven met hoge dichtheid is het noodzakelijk om de antenne op een tip te bevestigen die over de opnameschijf beweegt. Omdat dit in feite hetzelfde is als wat er al gebeurd in prototypes van warmte geassisteerde magnetische opslag, is dit waarschijnlijk niet de grootste uitdaging.

Van de meer fundamentele kant is het nog steeds interessant om meer onderzoek te doen naar de mogelijkheid om de twee ijzer locaties in bismut ijzer granaat onafhankelijk te exciteren of te detecteren door de juiste golflengte van het licht te selecteren zoals gesuggereerd in Hoofdstuk 5. In dit proefschrift hebben wij geen verschillen in de dynamica waargenomen, dit komt duidelijk door het feit dat we enkel een ferromagnetische toestand hebben geëxciteerd. Als alternatief zou kunnen worden geprobeerd om energie in een enkel subrooster te pompen, gebruikmakend van het omgekeerde Faraday effect op de juiste golflengte. Nu kan geprobeerd worden om de interactie tussen de twee subroosters waar te nemen. Daarnaast, als het inderdaad aangetoond kan worden dat er gevoeligheid voor de individuele ijzer locaties verkregen kan worden door de juiste keuze van de golflengte van de sonde, dan zou dit een voordeel opleveren voor de optische pomp-sonde techniek vergeleken met Röntgen technieken. Terwijl het met Röntgen straling alleen mogelijk is om verschillende elementen van elkaar te onderscheiden, zou de hier gesuggereerde meting in staat zijn dezelfde elementen in een verschillende kristalstructuur omgeving te kunnen onderscheiden.

List of Publications

[1] B. Koene, M. Deb, E. Popova, N. Keller, Th. Rasing, and A. Kirilyuk, "Excitation of magnetic precession in bismuth iron garnet via a polarization-independent impulsive photo-magnetic effect," (in preparation).

[2] B. Koene, M. Deb, E. Popova, N. Keller, Th. Rasing, and A. Kirilyuk, "Spectrally resolved optical probing of laser induced magnetization dynamics in bismuth iron garnet," (in preparation).

[3] O. Dzyapko, B. Koene, P. Nowik-Boltyk, V. Demidov, A. Kirilyuk, Th. Rasing, and S. Demokritov, "Degree of coherence in a magnon Bose-Einstein condensate," (in preparation).

[4] O. Dzyapko, B. Koene, P. Nowik-Boltyk, V. Demidov, A. Kirilyuk, Th. Rasing, and S. Demokritov, "A stroboscopic Faraday setup for the measurement of the coherence of a magnon gas," (in preparation).

[5] T. Liu, T. Wang, A. H. Reid, M. Savoini, X. Wu, B. Koene, P. Granitzka, C. Graves, D. Higley, Z. Chen, G. Razinskas, M. Hantschmann, A. Scherz, J. Stöhr, A. Tsukamoto, B. Hecht, A. V. Kimel, A. Kirilyuk, Th. Rasing, and H. A. Dürr, "Nanoscale confinement of all-optical switching in TbFeCo using plasmonic antennas," (submitted).

[6] Y. Hashimoto, A. R. Khorsand, M. Savoini, B. Koene, D. Bossini, A. Tsukamoto, A. Itoh, Y. Ohtsuka, K. Aoshima, A. V. Kimel, A. Kirilyuk, and Th. Rasing, "Ultrafast time-resolved magneto-optical imaging of all-optical switching in GdFeCo with femtosecond time-resolution and a μm spatial-resolution," Review of Scientific Instruments **85**, 063702 (2014).

[7] M. Savoini, R. Medapalli, B. Koene, A. R. Khorsand, L. Le Guyader, L. Duò, M. Finazzi, A. Tsukamoto, A. Itoh, F. Nolting, A. Kirilyuk, A. V. Kimel, and Th. Rasing, "Highly efficient all-optical switching of magnetization in GdFeCo microstructures by interference-enhanced absorption of light," Physical Review B **86**, 140404 (2012).

[8] B. Koene, M. Savoini, A. V. Kimel, A. Kirilyuk, and Th. Rasing, “Optical energy optimization at the nanoscale by near-field interference,” Applied Physics Letters **101**, 013115 (2012).

[9] R. W. Heeres, S. N. Dorenbos, B. Koene, G. S. Solomon, L. P. Kouwenhoven, and V. Zwiller, “On-chip single plasmon detection,” Nano Letters **10**, 661 (2010).

Curriculum Vitae

Name: Benny Koene
Date of birth: October 16, 1985
Nationality: Dutch
E-mail: benkoene@gmail.com

2010 – 2014	PhD in Physics, *FOM/Radboud University Nijmegen*
2007 – 2010	MSc in Applied Physics *Delft, University of Technology*
2004 – 2008	BSc in Applied Physics *Delft, University of Technology*
1998 – 2004	Secondary education, VWO *Goudse Scholen Gemeenschap Leo Vroman*